

RICE UNIVERSITY

**A Comparative Study Based on Patient-Specific  
Fluid–Structure Interaction Modeling of Cerebral  
Aneurysms**

by

**Tyler M. Brummer, 2nd Lt, USAF**

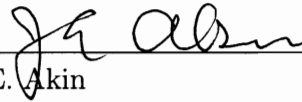
A THESIS SUBMITTED  
IN PARTIAL FULFILLMENT OF THE  
REQUIREMENTS FOR THE DEGREE

**Master of Science**

APPROVED, THESIS COMMITTEE:



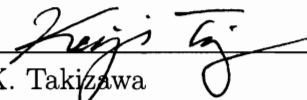
\_\_\_\_\_  
T. E. Tezduyar, Chair  
Professor of Mechanical Engineering and  
Materials Science



\_\_\_\_\_  
J. E. Akin  
Professor of Mechanical Engineering and  
Materials Science and Professor of  
Computational and Applied Mathematics



\_\_\_\_\_  
A. J. Meade  
Professor of Mechanical Engineering and  
Materials Science



\_\_\_\_\_  
K. Takizawa  
Associate Professor in Department of  
Modern Mechanical Engineering and  
Waseda Institute for Advanced Study  
Waseda University, Tokyo, Japan

HOUSTON, TEXAS

APRIL 2011

The views expressed in this thesis are those of the author and do not reflect the official policy or position of the United States Air Force, Department of Defense, or the U. S. Government.

# Abstract

## **A Comparative Study Based on Patient-Specific Fluid–Structure Interaction Modeling of Cerebral Aneurysms**

by

**Tyler M. Brummer**

The Team for Advanced Flow Simulation and Modeling (T★AFSM) at Rice University has been developing techniques to address the computational challenges involved in fluid–structure interaction (FSI) modeling. The Stabilized Space–Time FSI (SSTFSI) core technologies, in conjunction with an array of special techniques, is used in a comparative study of patient-specific cerebral aneurysms. Ten cases, from three different locations, are studied, half of which were ruptured. The study compares the wall shear stress, oscillatory shear index, and the arterial-wall stress and stretch, with the original motivation of finding significant differences between ruptured and unruptured aneurysms. Simpler approaches to computer modeling of cerebral aneurysms are also compared to FSI modeling.

# Acknowledgments

First I would like to thank Dr. Tayfun Tezduyar for the opportunity to study with the T★AFSM at Rice University. The experience of participating in a group that is at the forefront of FSI modeling is an opportunity for which I am truly grateful.

To Dr. Kenji Takizawa, I am quite sure there are not enough ways to say “thank you” in the Japanese language to correctly encompass my gratitude. He is one of the most intellectually gifted people I have ever met and his work ethic is inspiring. I look forward to seeing the product of his research in years to come.

A great deal of thanks is owed to the members of my thesis committee. Dr. Tezduyar, Dr. Akin, Dr. Meade, and Dr. Takizawa. Thank you for your time and thoughtful input.

I would like to extend my thanks to Dr. Peng R. Chen. His experience as a neurosurgeon was immensely beneficial. I am continually amazed at his example of devotion and passion as he offers aid to his patients.

I would like to thank the members of the T★AFSM with whom I had the pleasure of knowing and working with: Lt. Creighton Moorman, Lt. Eddie Wright, Lt. Brad Henicke, Lt. Tim Spielman, Lt. Tracee Curlett, Matthew Fritze, Nikolay Kostov, Lt. Matthew Guertin, Lt. Darren Montes, Lt. Anthony Puntel, and Lt. Kathleen Schjodt. I’d also like to thank the Air Force family that I had the pleasure of spending time with while at Rice University: Lt. Danielle Burke, Lt. Joel Martin, Lt. Eric Mees, Lt. Adam Sievers, Lt. Jon Wilder, Lt. Wyatt Harris, Lt. Tim Phillips, Lt. Brad Ward,

Lt. Matt Wichmann, Lt. Eric Herbort, Lt. Millie Mays, and Lt. Woody Sukut. To the greeks, thanks for the lunches and insightful perspectives.

Much thanks to my parents, Mike and Mel, and my brother, Austin, who have always supported me in my education and career. You always prove that family is there no matter what.

Finally and most importantly to my beautiful bride, Danielle. Thank you so much for supporting me throughout my career. The sacrifices you make are greater than mine, and I thank you for all the warm meals and patience as I worked late. You truly are my best friend and greatest fan. I am confident with you by my side as we embark on our career in the Air Force. I could not have done so well without your unwavering support.

This work was supported partly by John & Ann Doerr Fund for Computational Biomedicine. It was also supported partly by NSF Grant CNS-0821727. The 3DRA research at the Memorial Hermann was supported by the Weatherhead Foundation. We thank Dr. Ryo Torii for the velocity wave form.

# Contents

<b>Abstract</b>	<b>iii</b>
<b>Acknowledgments</b>	<b>iv</b>
<b>List of Figures</b>	<b>ix</b>
<b>List of Tables</b>	<b>xiv</b>
<b>1 Introduction</b>	<b>1</b>
1.1 Overview . . . . .	3
<b>2 Governing Equations</b>	<b>5</b>
2.1 Fluid Mechanics (blood flow) . . . . .	5
2.2 Structural Mechanics (arterial-wall deformation) . . . . .	6
2.2.1 Continuum Element Made of Fung Material . . . . .	7
<b>3 Finite Element Formulations</b>	<b>8</b>
3.1 DSD/SST Formulation of Fluid Mechanics . . . . .	8
3.2 Semi-discrete Formulation of Structural Mechanics . . . . .	12
3.3 Stabilized Space–Time Fluid–Structure Interaction (SSTFSI) Technique	14
<b>4 Special Modeling Techniques</b>	<b>17</b>
4.1 Separated Stress Projection . . . . .	17

4.2	Mapping Technique for Inflow Boundaries . . . . .	19
4.3	Preconditioning Technique . . . . .	20
4.4	Boundary Condition Techniques for Inclined Inflow and Outflow Planes	21
4.4.1	Structural Mechanics Equations . . . . .	22
4.4.2	Mesh-Moving Equations . . . . .	22
4.5	Wall Shear Stress Calculation . . . . .	23
4.6	Oscillatory Shear Index . . . . .	24
<b>5</b>	<b>Mesh Generation and Simulation Conditions</b>	<b>26</b>
5.1	Arterial-Surface Extraction from Medical Images . . . . .	26
5.2	Mesh Generation and Estimated Zero Pressure Geometry . . . . .	27
5.3	Fluid and Structure Properties . . . . .	31
5.4	Boundary Conditions . . . . .	32
5.5	Computational Conditions . . . . .	36
5.6	Simulation Sequence . . . . .	36
5.6.1	Fluid–Structure Interaction (FSI) . . . . .	37
5.6.2	Rigid Artery (RA) . . . . .	38
5.6.3	Structure (S) . . . . .	38
5.6.4	Prescribed Shape (PS) . . . . .	39
<b>6</b>	<b>Computational Results</b>	<b>40</b>
6.1	Computational Models . . . . .	40
6.2	Comparative Study . . . . .	55
6.2.1	Blood Flow Characteristics . . . . .	55
6.2.2	Arterial-Wall Characteristics . . . . .	69
6.3	Evaluation of Simpler Modeling Approaches . . . . .	81
6.4	Mesh Refinement . . . . .	89

<b>7 Findings and Conclusions</b>	<b>98</b>
7.1 Findings . . . . .	98
7.2 Conclusions . . . . .	99
<b>Bibliography</b>	<b>100</b>



# List of Figures

4.1	Special mapping technique. . . . .	20
5.1	Structural mechanics mesh generation process for a sample model. The color range represents red (large) to blue (small). . . . .	29
5.2	Structural mechanics mesh of hexahedral elements at zero-pressure. . . . .	30
5.3	Fluid mechanics mesh generation process for a sample model. The color range represents red (large) to blue (small). . . . .	31
5.4	Fluid mechanics mesh of tetrahedral elements at starting pressure. . . . .	32
5.5	Sample volumetric flow rate. . . . .	34
5.6	Sample outflow pressure profile corresponding to the sample flow rate shown in Figure 5.5. . . . .	35
6.1	Arterial lumen geometry obtained from voxel data for the ten models studied. . . . .	41
6.2	Structural mechanics meshes at zero pressure for the MCA models. . . . .	43
6.3	Structural mechanics meshes at zero pressure for the Acom models. . . . .	44
6.4	Structural mechanics meshes at zero pressure for the Basilar models. . . . .	45
6.5	Fluid mechanics meshes at starting pressure at the fluid–structure interface and inflow plane for the MCA models. . . . .	46
6.6	Fluid mechanics meshes at starting pressure at the fluid–structure interface and inflow plane for the Acom models. . . . .	47

6.7	Fluid mechanics meshes at starting pressure at the fluid–structure interface and inflow plane for the Basilar models. . . . .	48
6.8	Mass balance for M1MCA. . . . .	50
6.9	Mass balance for M2MCA. . . . .	50
6.10	Mass balance for M3MCA. . . . .	51
6.11	Mass balance for M4MCA. . . . .	51
6.12	Mass balance for M5Acom. . . . .	52
6.13	Mass balance for M6Acom. . . . .	52
6.14	Mass balance for M7Acom. . . . .	53
6.15	Mass balance for M8Acom. . . . .	53
6.16	Mass balance for M9Basilar. . . . .	54
6.17	Mass balance for M10Basilar. . . . .	54
6.18	Maximum WSS (dyn/cm <sup>2</sup> ) in space and time. . . . .	56
6.19	Average WSS (dyn/cm <sup>2</sup> ) in space and time. . . . .	56
6.20	WSS at peak flow for M1MCA. . . . .	57
6.21	WSS at peak flow for M2MCA. . . . .	57
6.22	WSS at peak flow for M3MCA. . . . .	58
6.23	WSS at peak flow for M4MCA. . . . .	58
6.24	WSS at peak flow for M5Acom. . . . .	59
6.25	WSS at peak flow for M6Acom. . . . .	59
6.26	WSS at peak flow for M7Acom. . . . .	60
6.27	WSS at peak flow for M8Acom. . . . .	60
6.28	WSS at peak flow for M9Basilar. . . . .	61
6.29	WSS at peak flow for M10Basilar. . . . .	61
6.30	Streamlines showing WSS on the dome of the aneurysm for M1MCA at 0.06 s after the peak flow. The maximum WSS on the dome is 19.0 dyn/cm <sup>2</sup> . . . . .	62

6.31 Streamlines showing WSS on the dome of the aneurysm for M3MCA at 0.03 s after the peak flow. The maximum WSS on the dome is 107.3 dyn/cm <sup>2</sup> . . . . .	62
6.32 Streamlines showing WSS on the dome of the aneurysm for M5Acom at 0.06 s after the peak flow. The maximum WSS on the dome is 65.5 dyn/cm <sup>2</sup> . . . . .	63
6.33 Streamlines showing WSS on the dome of the aneurysm for M6Acom at 0.03 s after the peak flow. The maximum WSS on the dome is 136.3 dyn/cm <sup>2</sup> . . . . .	63
6.34 OSI for M1MCA. . . . .	64
6.35 OSI for M2MCA. . . . .	64
6.36 OSI for M3MCA. . . . .	65
6.37 OSI for M4MCA. . . . .	65
6.38 OSI for M5Acom. . . . .	66
6.39 OSI for M6Acom. . . . .	66
6.40 OSI for M7Acom. . . . .	67
6.41 OSI for M8Acom. . . . .	67
6.42 OSI for M9Basilar. . . . .	68
6.43 OSI for M10Basilar. . . . .	68
6.44 Maximum stress (kPa) in space and time. . . . .	69
6.45 Maximum variation in stress (kPa) in space and time. . . . .	70
6.46 Stress at peak pressure for M1MCA. . . . .	70
6.47 Stress at peak pressure for M2MCA. . . . .	71
6.48 Stress at peak pressure for M3MCA. . . . .	71
6.49 Stress at peak pressure for M4MCA. . . . .	72
6.50 Stress at peak pressure for M5Acom. . . . .	72
6.51 Stress at peak pressure for M6Acom. . . . .	73

6.52 Stress at peak pressure for M7Acom. . . . .	73
6.53 Stress at peak pressure for M8Acom. . . . .	74
6.54 Stress at peak pressure for M9Basilar. . . . .	74
6.55 Stress at peak pressure for M10Basilar. . . . .	75
6.56 Maximum stretch in space and time. . . . .	75
6.57 Stretch at peak pressure for M1MCA. . . . .	76
6.58 Stretch at peak pressure for M2MCA. . . . .	76
6.59 Stretch at peak pressure for M3MCA. . . . .	77
6.60 Stretch at peak pressure for M4MCA. . . . .	77
6.61 Stretch at peak pressure for M5Acom. . . . .	78
6.62 Stretch at peak pressure for M6Acom. . . . .	78
6.63 Stretch at peak pressure for M7Acom. . . . .	79
6.64 Stretch at peak pressure for M8Acom. . . . .	79
6.65 Stretch at peak pressure for M9Basilar. . . . .	80
6.66 Stretch at peak pressure for M10Basilar. . . . .	80
6.67 Maximum WSS (dyn/cm <sup>2</sup> ) in space and time. . . . .	82
6.68 Average WSS (dyn/cm <sup>2</sup> ) in space and time. . . . .	83
6.69 PS WSS at peak flow for M5Acom. . . . .	83
6.70 RA WSS at peak flow for M5Acom. . . . .	84
6.71 PS OSI for M5Acom. . . . .	84
6.72 RA OSI for M5Acom. . . . .	85
6.73 Maximum stress (kPa) in space and time. . . . .	86
6.74 Structure only stress at peak pressure for M3MCA. . . . .	87
6.75 Average stretch in space and time. . . . .	87
6.76 Structure only stretch at peak pressure for M3MCA. . . . .	88
6.77 Structural mechanics meshes at zero pressure: M1MCA (left) and M1MCA-FS (right). . . . .	89

6.78 Structural mechanics meshes at zero pressure: M3MCA (left) and M3MCA-FS (right). . . . .	90
6.79 Fluid mechanics meshes at starting pressure at the fluid–structure interface and inflow plane for M1MCA (left) and M1MCA-FF (right). .	91
6.80 Fluid mechanics meshes at starting pressure at the fluid–structure interface and inflow plane for M3MCA (left) and M3MCA-FF (right). .	91
6.81 WSS at peak flow for M1MCA-FF. . . . .	93
6.82 WSS at peak flow for M3MCA-FF. . . . .	93
6.83 OSI for M1MCA-FF. . . . .	94
6.84 OSI for M3MCA-FF. . . . .	94
6.85 Stress at peak pressure for M1MCA-FS. . . . .	96
6.86 Stress at peak pressure for M3MCA-FS. . . . .	96
6.87 Stretch at peak pressure for M1MCA-FS. . . . .	97
6.88 Stretch at peak pressure for M3MCA-FS. . . . .	97

# List of Tables

6.1	Physical parameters for the ten arterial models. Diameters are in mm and peak volumetric flow rate is in ml/s. . . . .	42
6.2	Number of nodes and elements for the structural mechanics mesh of each of the ten arterial models. Here $nn$ and $ne$ are number of nodes and elements, respectively. . . . .	45
6.3	Number of nodes and elements for the fluid mechanics mesh of each of the ten arterial models. Here $nn$ and $ne$ are number of nodes and elements, respectively. . . . .	48
6.4	Computational parameters for the ten arterial models. Structure scales and fluid scales for the momentum conservation are 100 and 1.0 respectively for all models. . . . .	49
6.5	Computational parameters for the ten arterial models. Structure scales and fluid scales are 100 and 1.0 respectively for all models. . . . .	81
6.6	Number of nodes ( $nn$ ) and elements ( $ne$ ) for the standard and refined structural mechanics meshes for the two models. . . . .	90
6.7	Number of nodes ( $nn$ ) and elements ( $ne$ ) for the standard and refined fluid mechanics meshes for the two models. . . . .	90
6.8	Maximum and average WSS (dyn/cm <sup>2</sup> ) in space and time. . . . .	92
6.9	Maximum stress (kPa) at peak pressure and average stretch in space and time. . . . .	95

# Chapter 1

## Introduction

In 1808, the first theory of blood flow was introduced [85]. In 1881, the elastic properties of the arterial-wall were first investigated [34]. These two theories, though hypothesized independently, have inspired research in biomechanics and development of computational methods needed for that. While considering problems of blood flow in arterial networks, the blood flow causes fluid tractions on the surface of the elastic wall which cause structural displacements, making the structure dependent on the fluid forces. As the structure deforms, the fluid flow changes, making the fluid dependent on the structural shape. Thus, there is a need to correctly model this interaction. An approach to successfully model these coupling forces is known as fluid–structure interaction (FSI) modeling. The Team for Advanced Flow Simulation and Modeling (T★AFSM) at Rice University has developed techniques for FSI modeling (see, for example, [50, 10, 3, 23, 11, 24, 51, 38, 32, 80, 65, 72, 73, 5, 25, 55, 60, 36, 59, 47, 44, 84, 75, 28, 63, 62, 64, 35, 76, 4, 22, 16, 66, 77, 6, 7, 39, 40, 69, 78, 29, 79, 9, 70, 8, 42, 41, 46, 30, 67, 45, 43])

Cardiovascular diseases are the leading cause of death and disability today. Aneurysms are one such disease and are estimated to plague six percent of the general population. The two most common types of aneurysms are abdominal and intracranial,

of which the later is the focus of this work. Intracranial aneurysms primarily occur near the circle of Willis, a major network of arteries that supply the brain with blood. Aneurysms arise from the degeneration of the arterial-wall, often the constituents medial elastin and smooth muscle. The degeneration can occur from an array of risk factors such as genetics, age, smoking and drug use, direct head trauma, infection, brain tumors, hypertension, and other factors which are currently being studied. When the biomechanical factors of the arterial-wall have sufficiently degenerated, hemodynamic forces cause the artery wall to balloon outwards forming the aneurysm. Rupture occurs when the wall stress exceeds the material strength of the arterial-wall and blood begins to leak into the intracranial cavity. Once an aneurysm ruptures, a patient has a 40 percent chance of death even if they receive immediate medical treatment. Of those that survive treatment, 35 percent experience moderate to severe brain damage and only 15–30 percent experience mild or no difficulties [48, 81, 18].

Cerebral aneurysms are detected by various means such as Computed Tomographic Angiography (CTA), Magnetic Resonance Angiography (MRA), and in this effort 3D Rotational Angiography (3DRA). Once a cerebral aneurysm is detected, there are three methods of treatment. Medical therapy is for small, unruptured aneurysms where regular medical imaging to monitor growth and risk factors is used in combination with therapy to reduce medical conditions that cause rupture. Neurosurgery is open surgery where the aneurysm is exposed and a neurosurgeon clips the aneurysm to occlude it from the arterial network. Interventional neuroradiology/endovascular neurosurgery is a minimally invasive procedure where an endovascular surgeon places soft platinum micro-coils into the aneurysm to reduce blood circulation. All treatment methods carry significant risk and there is a pressing need to distinguish whether or not an aneurysm needs treatment and what aneurysms are more susceptible to rupture [48, 81, 18].



The focus of this thesis is to summarize the tools developed by the T★AFSM to model aneurysms using FSI and perform a comparative study of ruptured to unruptured aneurysms. Ten cases, from three different locations, are studied. Half of the cases were ruptured. We compare the physical characteristics of wall shear stress (WSS), oscillatory shear index (OSI), and the arterial-wall stress and stretch in an effort that was originally motivated by looking for significant differences between ruptured and unruptured aneurysms. In addition, we investigate how simpler approaches perform compared to FSI modeling and perform mesh refinement studies.

## 1.1 Overview

Chapter 2 provides a description of the governing equations for the blood flow and arterial-wall deformation. The Navier–Stokes equations of incompressible flows and the structural mechanics equations are explained.

Chapter 3 shows the solution technique for the fluid mechanics part as the Deforming-Spatial-Domain/Stabilized Space–Time (DSD/SST) formulation. For the structural mechanics part, a standard finite element formulation is explained. The FSI modeling, including the coupling of the fluid and structural mechanics part, is accomplished using the Stabilized Space–Time FSI (SSTFSI) technique.

Special modeling techniques are described in Chapter 4. These techniques include a method developed to separately project the pressure and viscous forces of the fluid to the structure, a special mapping technique for non-circular inflow shapes, a preconditioning technique, a boundary condition technique for inclined planes, and techniques for calculating fluid effects.

Special mesh generation techniques are explained in Chapter 5 as well as fluid and structural properties and boundary conditions for the computation. Simulation sequences for the FSI technique and the simpler approaches to modeling are also

shown.

Chapter 6 shows results for the comparative study, showing the physical characteristics of WSS, OSI, and arterial-wall stress and stretch. The simpler approaches to modeling are also shown.

Findings and conclusions are presented in Chapter 7.

# Chapter 2

## Governing Equations

The equations in this chapter define the blood flow and arterial-wall deformation. For the arterial diameters and flow rates we consider in this thesis, the average shear rate in the artery is larger than  $150 \text{ s}^{-1}$ . As it was pointed out in [75], the viscosity of the blood can be assumed to be constant if the shear rate is high enough ( $> 150 \text{ s}^{-1}$ ) [82]. Therefore, we assume the blood to be Newtonian here [75] even though the blood is known to be non-Newtonian in general. Section 2.1 shows the Navier–Stokes equations of incompressible flow which govern the fluid mechanics. The arterial-wall is modeled with hyperelastic continuum elements made of Fung material. Section 2.2 shows the equations governing this structural model.

### 2.1 Fluid Mechanics (blood flow)

Let  $\Omega_t \subset \mathbb{R}^{n_{sd}}$  be the spatial domain with boundary  $\Gamma_t$  at time  $t \in (0, T)$ . The subscript  $t$  indicates the time-dependence of the domain. The Navier–Stokes equations of incompressible flows are written on  $\Omega_t$  and  $\forall t \in (0, T)$  as

$$\rho \left( \frac{\partial \mathbf{u}}{\partial t} + \mathbf{u} \cdot \nabla \mathbf{u} - \mathbf{f} \right) - \nabla \cdot \boldsymbol{\sigma} = \mathbf{0}, \quad (2.1)$$

$$\nabla \cdot \mathbf{u} = 0, \quad (2.2)$$

where  $\rho$ ,  $\mathbf{u}$  and  $\mathbf{f}$  are the density, velocity and the external force, respectively. The stress tensor  $\boldsymbol{\sigma}$  is defined as  $\boldsymbol{\sigma}(p, \mathbf{u}) = -p\mathbf{I} + 2\mu\boldsymbol{\epsilon}(\mathbf{u})$ , with  $\boldsymbol{\epsilon}(\mathbf{u}) = ((\nabla\mathbf{u}) + (\nabla\mathbf{u})^T)/2$ . Here  $p$  is the pressure,  $\mathbf{I}$  is the identity tensor,  $\mu = \rho\nu$  is the viscosity,  $\nu$  is the kinematic viscosity, and  $\boldsymbol{\epsilon}(\mathbf{u})$  is the strain-rate tensor. The essential and natural boundary conditions for Eq. (2.1) are represented as  $\mathbf{u} = \mathbf{g}$  on  $(\Gamma_t)_g$  and  $\mathbf{n} \cdot \boldsymbol{\sigma} = \mathbf{h}$  on  $(\Gamma_t)_h$ , where  $(\Gamma_t)_g$  and  $(\Gamma_t)_h$  are complementary subsets of the boundary  $\Gamma_t$ ,  $\mathbf{n}$  is the unit normal vector, and  $\mathbf{g}$  and  $\mathbf{h}$  are given functions. A divergence-free velocity field  $\mathbf{u}_0(\mathbf{x})$  is specified as the initial condition.

## 2.2 Structural Mechanics (arterial-wall deformation)

Let  $\Omega_t^s \subset \mathbb{R}^{n_{xd}}$  be the spatial domain with boundary  $\Gamma_t^s$ , where  $n_{xd} = 3$  for the continuum element and  $n_{xd} = 2$  for the membrane element. The superscript “s” indicates the structure. The parts of  $\Gamma_t^s$  corresponding to the essential and natural boundary conditions are represented by  $(\Gamma_t^s)_g$  and  $(\Gamma_t^s)_h$ . The equations of motion are written as

$$\rho^s \left( \frac{d^2\mathbf{y}}{dt^2} + \eta \frac{d\mathbf{y}}{dt} - \mathbf{f}^s \right) - \nabla \cdot \boldsymbol{\sigma}^s = \mathbf{0}, \quad (2.3)$$

where  $\rho^s$ ,  $\mathbf{y}$ ,  $\eta$ ,  $\mathbf{f}^s$  and  $\boldsymbol{\sigma}^s$  are the material density, structural displacement, damping coefficient, external force and the Cauchy stress tensor, respectively. The stresses are expressed in terms of the second Piola–Kirchhoff stress tensor  $\mathbf{S}$ , which is related to the Cauchy stress tensor through a kinematic transformation. For the arterial structural models we describe here, what makes one structural element model different from the other is the manner in which  $\mathbf{S}$  is defined.

### 2.2.1 Continuum Element Made of Fung Material

For the continuum element made of Fung material, the expression for  $\mathbf{S}$  is given as

$$S^{ij} = 2D_1D_2 e^{D_2(I_1-3)} G^{ij} + \left( K_{\text{PEN}} \ln \left( \sqrt{I_3} \right) - 2D_1D_2 \right) g^{ij}, \quad (2.4)$$

where  $I_1$  is the first invariant of the right Cauchy–Green deformation tensor,  $D_1$  and  $D_2$  are the Fung material constants, and  $K_{\text{PEN}}$  is defined as

$$K_{\text{PEN}} = \frac{2D_1D_2}{(1 - 2\nu_{\text{PEN}})}. \quad (2.5)$$

# Chapter 3

## Finite Element Formulations

The equations described in this chapter are the basis for the fully coupled FSI computations reported in this thesis. Section 3.1 describes the DSD/SST formulation that is used for the fluid mechanics part of the computation. Section 3.2 describes the semi-discrete formulation used for the structural mechanics parts. These two formulations are coupled in the SSTFSI method described in Section 3.3.

### 3.1 DSD/SST Formulation of Fluid Mechanics

In the DSD/SST method [52, 56, 57, 53], the finite element formulation is written over a sequence of  $N$  space–time slabs  $Q_n$ , where  $Q_n$  is the slice of the space–time domain between the time levels  $t_n$  and  $t_{n+1}$ . At each time step, the integrations are performed over  $Q_n$ . The space–time finite element interpolation functions are continuous within a space–time slab, but discontinuous from one space–time slab to another. The notation  $(\cdot)_n^-$  and  $(\cdot)_n^+$  will denote the function values at  $t_n$  as approached from below and above. Each  $Q_n$  is decomposed into elements  $Q_n^e$ , where  $e = 1, 2, \dots, (n_{el})_n$ . The subscript  $n$  used with  $n_{el}$  is for the general case where the number of space–time elements may change from one space–time slab to another. The essential and natural boundary conditions are enforced over  $(P_n)_g$  and  $(P_n)_h$ , the complementary subsets of

the lateral boundary of the space–time slab. The finite element trial function spaces  $(\mathcal{S}_{\mathbf{u}}^h)_n$  for velocity and  $(\mathcal{S}_p^h)_n$  for pressure, and the test function spaces  $(\mathcal{V}_{\mathbf{u}}^h)_n$  and  $(\mathcal{V}_p^h)_n = (\mathcal{S}_p^h)_n$  are defined by using, over  $Q_n$ , first-order polynomials in space and time.

The DSD/SST formulation (from [53]) is written as follows: given  $(\mathbf{u}^h)_n^-$ , find  $\mathbf{u}^h \in (\mathcal{S}_{\mathbf{u}}^h)_n$  and  $p^h \in (\mathcal{S}_p^h)_n$  such that  $\forall \mathbf{w}^h \in (\mathcal{V}_{\mathbf{u}}^h)_n$  and  $\forall q^h \in (\mathcal{V}_p^h)_n$ :

$$\begin{aligned}
& \int_{Q_n} \mathbf{w}^h \cdot \rho \left( \frac{\partial \mathbf{u}^h}{\partial t} + \mathbf{u}^h \cdot \nabla \mathbf{u}^h - \mathbf{f}^h \right) dQ + \int_{Q_n} \boldsymbol{\varepsilon}(\mathbf{w}^h) : \boldsymbol{\sigma}(p^h, \mathbf{u}^h) dQ \\
& - \int_{(P_n)_h} \mathbf{w}^h \cdot \mathbf{h}^h dP + \int_{Q_n} q^h \nabla \cdot \mathbf{u}^h dQ + \int_{\Omega_n} (\mathbf{w}^h)_n^+ \cdot \rho ((\mathbf{u}^h)_n^+ - (\mathbf{u}^h)_n^-) d\Omega \\
& + \sum_{e=1}^{(n_{el})_n} \int_{Q_n^e} \frac{1}{\rho} \left[ \tau_{\text{SUPG}} \rho \left( \frac{\partial \mathbf{w}^h}{\partial t} + \mathbf{u}^h \cdot \nabla \mathbf{w}^h \right) + \tau_{\text{PSPG}} \nabla q^h \right] \cdot [\mathbb{L}(p^h, \mathbf{u}^h) - \rho \mathbf{f}^h] dQ \\
& + \sum_{e=1}^{(n_{el})_n} \int_{Q_n^e} \nu_{\text{LSIC}} \nabla \cdot \mathbf{w}^h \rho \nabla \cdot \mathbf{u}^h dQ = 0, \tag{3.1}
\end{aligned}$$

where

$$\mathbb{L}(q^h, \mathbf{w}^h) = \rho \left( \frac{\partial \mathbf{w}^h}{\partial t} + \mathbf{u}^h \cdot \nabla \mathbf{w}^h \right) - \nabla \cdot \boldsymbol{\sigma}(q^h, \mathbf{w}^h). \tag{3.2}$$

This formulation is applied to all space–time slabs  $Q_0, Q_1, Q_2, \dots, Q_{N-1}$ , starting with  $(\mathbf{u}^h)_0^- = \mathbf{u}_0$ . Here  $\tau_{\text{SUPG}}$ ,  $\tau_{\text{PSPG}}$  and  $\nu_{\text{LSIC}}$  are the SUPG, PSPG and LSIC (least-squares on incompressibility constraint) stabilization parameters. There are various ways of

defining these stabilization parameters. Here we provide the definitions given in [53]:

$$\tau_{\text{SUPG}} = \left( \frac{1}{\tau_{\text{SUGN12}}^2} + \frac{1}{\tau_{\text{SUGN3}}^2} \right)^{-\frac{1}{2}}, \quad (3.3)$$

$$\tau_{\text{SUGN12}} = \left( \sum_{a=1}^{n_{en}} \left| \frac{\partial N_a}{\partial t} + \mathbf{u}^h \cdot \nabla N_a \right| \right)^{-1}, \quad (3.4)$$

$$\tau_{\text{SUGN3}} = \frac{h_{\text{RGN}}^2}{4\nu}, \quad (3.5)$$

$$h_{\text{RGN}} = 2 \left( \sum_{a=1}^{n_{en}} |\mathbf{r} \cdot \nabla N_a| \right)^{-1}, \quad (3.6)$$

$$\mathbf{r} = \frac{\nabla \|\mathbf{u}^h\|}{\|\nabla \|\mathbf{u}^h\|\|}, \quad (3.7)$$

$$\tau_{\text{PSPG}} = \tau_{\text{SUPG}}, \quad (3.8)$$

and in [59]:

$$\nu_{\text{LSIC}} = \tau_{\text{SUPG}} \|\mathbf{u}^h - \mathbf{v}^h\|^2, \quad (3.9)$$

where  $n_{en}$  is the number of (space–time) element nodes and  $N_a$  is the space–time shape function associated with the space–time node  $a$ . As an alternative to the construction of  $\tau_{\text{SUPG}}$  as given by Eqs. (3.3)–(3.4), another option was introduced in [59]. In that option,  $\tau_{\text{SUPG}}$  is constructed based on separate definitions for the advection-dominated and transient-dominated limits:

$$\tau_{\text{SUPG}} = \left( \frac{1}{\tau_{\text{SUGN1}}^2} + \frac{1}{\tau_{\text{SUGN2}}^2} + \frac{1}{\tau_{\text{SUGN3}}^2} \right)^{-\frac{1}{2}}, \quad (3.10)$$

$$\tau_{\text{SUGN1}} = \left( \sum_{a=1}^{n_{en}} |(\mathbf{u}^h - \mathbf{v}^h) \cdot \nabla N_a| \right)^{-1}, \quad (3.11)$$

$$\tau_{\text{SUGN2}} = \frac{\Delta t}{2}, \quad (3.12)$$

where  $\mathbf{v}^h$  is the mesh velocity and  $\Delta t$  is the time-step size. It was noted in [59] that separating  $\tau_{\text{SUGN12}}$  into its advection- and transient-dominated components as



given by Eqs. (3.11)–(3.12) is equivalent to excluding the  $\left(\frac{\partial N_a}{\partial t} \Big|_{\boldsymbol{\xi}}\right)$  part of  $\left(\frac{\partial N_a}{\partial t}\right)$  in Eq. (3.4), making that the definition for  $\tau_{\text{SUGN1}}$ , and accounting for  $\left(\frac{\partial N_a}{\partial t} \Big|_{\boldsymbol{\xi}}\right)$  in the definition for  $\tau_{\text{SUGN2}}$  given by Eq. (3.12). Here  $\boldsymbol{\xi}$  is the vector of element coordinates. For more ways of calculating  $\tau_{\text{SUPG}}$ ,  $\tau_{\text{PSPG}}$  and  $\nu_{\text{LSIC}}$ , see [58, 1, 53, 54, 2, 55, 33, 13, 14, 20, 15]. References [53, 54, 55] also include the Discontinuity-Capturing Directional Dissipation (DCDD) stabilization, which was introduced as an alternative to the LSIC stabilization.

Several remarks from [67] are summarized in the following.

**Remark 1** *As an alternative to how the SUPG test function is defined in Eq. (3.1), another option was proposed in [59]. In this option, the SUPG test function  $\left(\frac{\partial \mathbf{w}^h}{\partial t} + \mathbf{u}^h \cdot \nabla \mathbf{w}^h\right)$  is replaced with  $\left((\mathbf{u}^h - \mathbf{v}^h) \cdot \nabla \mathbf{w}^h\right)$ . This replacement is equivalent to excluding the  $\left(\frac{\partial \mathbf{w}^h}{\partial t} \Big|_{\boldsymbol{\xi}}\right)$  part of  $\left(\frac{\partial \mathbf{w}^h}{\partial t}\right)$ . In [59], this option was called “WTSE”, and the option where the  $\left(\frac{\partial \mathbf{w}^h}{\partial t} \Big|_{\boldsymbol{\xi}}\right)$  term is active, “WTSA”.*

**Remark 2** *The stability and accuracy analysis reported in [46] for the DSD/SST formulation of the time-dependent advection equation shows for linear functions in space and time that the WTSA option yields higher-order accuracy than the WTSE option.*

**Remark 3** *With the function spaces defined in the paragraph preceding Eq. (3.1), for each space–time slab velocity and pressure assume double unknown values at each spatial node. One value corresponds to the lower end of the slab, and the other one the upper end. In [59], the option of using double unknown values at a spatial node is called “DV” for velocity and “DP” for pressure. In this case, as pointed out in [59], we use two integration points over the time interval of the space–time slab, and this time-integration option is called “TIP2”. This version of the DSD/SST formulation, with the options set DV, DP and TIP2, is called “DSD/SST-DP”.*

**Remark 4** *In [59], the option of using, for each space–time slab, a single unknown pressure value at each spatial node was proposed with the option name “SP”. With this, another version of the DSD/SST formulation was proposed in [59], where the options set is DV, SP and TIP2. This version is called “DSD/SST-SP”. Because the number of unknown pressure values is halved, the computational cost is reduced substantially.*

**Remark 5** *To reduce the computational cost further, the option of using only one integration point over the time interval of the space–time slab was proposed in [59]. This time-itegration option is called “TIP1”. With that, a third version of the DSD/SST formulation was proposed in [59], where the options set is DV, SP and TIP1. This version is called “DSD/SST-TIP1”.*

**Remark 6** *For DSD/SST-SP and DSD/SST-TIP1, in integration of the incompressibility-constraint term over each space–time slab, as proposed in [39], we use only one integration point in time, shifted to the upper time level of the slab. All other terms in the space–time finite element formulation are integrated by using Gaussian quadrature points in time, with the number of points set to whatever we intended to have for the overall formulation. With this technique, as pointed in [39], the incompressibility constraint equation focuses on the velocity field  $(\mathbf{u}^h)_{n+1}^-$ .*

## 3.2 Semi-discrete Formulation of Structural Mechanics

With  $\mathbf{y}^h$  and  $\mathbf{w}^h$  coming from appropriately defined trial and test function spaces, respectively, the semi-discrete finite element formulation of the structural mechanics

equations (see [26, 12, 37]) is written as

$$\int_{\Omega_0^s} \mathbf{w}^h \cdot \rho^s \frac{d^2 \mathbf{y}^h}{dt^2} d\Omega^s + \int_{\Omega_0^s} \mathbf{w}^h \cdot \eta \rho^s \frac{d\mathbf{y}^h}{dt} d\Omega^s + \int_{\Omega_0^s} \delta \mathbf{E}^h : \mathbf{S}^h d\Omega^s = \int_{\Omega_t^s} \mathbf{w}^h \cdot (\mathbf{t}^h + \rho^s \mathbf{f}^s) d\Omega^s. \quad (3.13)$$

The fluid mechanics forces acting on the structure are represented by vector  $\mathbf{t}^h$ . The above formulation is for structures represented by a membrane model (extending the formulation to structures represented by a 3D continuum model is described in Section 3.3). The left-hand-side terms of Eq. (3.13) are referred to in the original configuration and the right-hand-side terms in the deformed configuration at time  $t$ . From this formulation at each time step we obtain a nonlinear system of equations. In solving that nonlinear system with an iterative method, we use an incremental form (see [26, 12, 37, 24]), which is expressed as

$$\left[ \frac{\mathbf{M}}{\beta \Delta t^2} + \frac{(1-\alpha)\gamma \mathbf{C}}{\beta \Delta t} + (1-\alpha) \mathbf{K} \right] \Delta \mathbf{d}^i = \mathbf{R}^i. \quad (3.14)$$

Here  $\mathbf{M}$  is the mass matrix,  $\mathbf{C}$  is the damping matrix,  $\mathbf{K}$  is the consistent tangent matrix associated with the internal elastic forces,  $\mathbf{R}^i$  is the residual vector at the  $i^{th}$  iteration, and  $\Delta \mathbf{d}^i$  is the  $i^{th}$  increment in the nodal displacements vector  $\mathbf{d}$ . For spatially-constant  $\eta$ , the damping matrix can be written as  $\mathbf{C} = \eta \mathbf{M}$ . All of the terms known from the previous iteration are lumped into the residual vector  $\mathbf{R}^i$ . The parameters  $\alpha, \beta, \gamma$  are part of the Hilber–Hughes–Taylor [19] scheme, which is the time-integration technique used here. In the computations reported here and those reported earlier by the T★AFSM, the mass matrix is lumped in the structural mechanics part.

### 3.3 Stabilized Space–Time Fluid–Structure Interaction (SSTFSI) Technique

The SSTFSI technique was introduced in [59], where it was described based on the finite element formulations given by Eqs. (3.1) and (3.13), with a slight change of notation and with a clarification of how the fluid–structure interface conditions are handled. In that notation subscripts 1 and 2 refer to fluid and structure, respectively. Furthermore, while subscript  $I$  refers to the fluid–structure interface, subscript  $E$  refers to “elsewhere” in the fluid and structure domains or boundaries. Here we write from [59] the equations representing the SSTFSI technique:

$$\begin{aligned}
& \int_{Q_n} \mathbf{w}_{1E}^h \cdot \rho \left( \frac{\partial \mathbf{u}^h}{\partial t} + \mathbf{u}^h \cdot \nabla \mathbf{u}^h - \mathbf{f}^h \right) dQ + \int_{Q_n} \boldsymbol{\varepsilon}(\mathbf{w}_{1E}^h) : \boldsymbol{\sigma}(p^h, \mathbf{u}^h) dQ \\
& - \int_{(P_n)_h} \mathbf{w}_{1E}^h \cdot \mathbf{h}_{1E}^h dP + \int_{Q_n} q_{1E}^h \nabla \cdot \mathbf{u}^h dQ + \int_{\Omega_n} (\mathbf{w}_{1E}^h)_n^+ \cdot \rho ((\mathbf{u}^h)_n^+ - (\mathbf{u}^h)_n^-) d\Omega \\
& + \sum_{e=1}^{(n_{el})_n} \int_{Q_n^e} \frac{1}{\rho} \left[ \tau_{\text{SUPG}} \rho \left( \frac{\partial \mathbf{w}_{1E}^h}{\partial t} + \mathbf{u}^h \cdot \nabla \mathbf{w}_{1E}^h \right) + \tau_{\text{PSPG}} \nabla q_{1E}^h \right] \cdot [\mathbf{L}(p^h, \mathbf{u}^h) - \rho \mathbf{f}^h] dQ \\
& + \sum_{e=1}^{(n_{el})_n} \int_{Q_n^e} \nu_{\text{LSIC}} \nabla \cdot \mathbf{w}_{1E}^h \rho \nabla \cdot \mathbf{u}^h dQ = 0, \tag{3.15}
\end{aligned}$$

$$\int_{Q_n} q_{1I}^h \nabla \cdot \mathbf{u}^h dQ + \sum_{e=1}^{(n_{el})_n} \int_{Q_n^e} \frac{1}{\rho} [\tau_{\text{PSPG}} \nabla q_{1I}^h] \cdot [\mathbf{L}(p^h, \mathbf{u}^h) - \rho \mathbf{f}^h] dQ = 0, \tag{3.16}$$

$$\int_{(\Gamma_{II})_{\text{REF}}} (\mathbf{w}_{1I}^h)_{n+1} \cdot ((\mathbf{x}_{1I}^h)_{n+1} - (\mathbf{x}_{2I}^h)_{n+1}) d\Gamma = 0, \tag{3.17}$$

$$\int_{(\Gamma_{II})_{\text{REF}}} (\mathbf{w}_{1I}^h)_{n+1}^- \cdot ((\mathbf{u}_{1I}^h)_{n+1}^- - \mathbf{u}_{2I}^h) d\Gamma = 0, \tag{3.18}$$

$$\begin{aligned}
\int_{(P_n)_h} (\mathbf{w}_{11}^h)_{n+1}^- \cdot \mathbf{h}_{11}^h dP &= - \int_{(P_n)_h} (\mathbf{w}_{11}^h)_{n+1}^- \cdot p \mathbf{n} dP + \int_{Q_n} 2\mu \boldsymbol{\varepsilon}((\mathbf{w}_{11}^h)_{n+1}^-) : \boldsymbol{\varepsilon}(\mathbf{u}) dQ \\
&+ \sum_{e=1}^{(nel)_n} \int_{Q_n^e} (\mathbf{w}_{11}^h)_{n+1}^- \cdot \nabla \cdot (2\mu \boldsymbol{\varepsilon}(\mathbf{u})) dQ, \tag{3.19}
\end{aligned}$$

$$\int_{(\Omega_{2I})_{\text{REF}}} \mathbf{w}_{2I}^h \cdot (\mathbf{h}_{2I}^h + (\mathbf{h}_{11}^h)_A + (\mathbf{h}_{11}^h)_B) d\Omega = 0, \tag{3.20}$$

$$\begin{aligned}
&\int_{(\Omega_2)_0} \mathbf{w}_2^h \cdot \rho_2 \frac{d^2 \mathbf{y}^h}{dt^2} d\Omega + \int_{(\Omega_2)_0} \mathbf{w}_2^h \cdot \eta \rho_2 \frac{d\mathbf{y}^h}{dt} d\Omega + \int_{(\Omega_2)_0} \delta \mathbf{E}^h : \mathbf{S}^h d\Omega \\
&= \int_{\Omega_2} \mathbf{w}_2^h \cdot \rho_2 \mathbf{f}_2^h d\Omega + \int_{\Omega_{2E}} \mathbf{w}_{2E}^h \cdot \mathbf{h}_{2E}^h d\Omega + \int_{\Omega_{2I}} \mathbf{w}_{2I}^h \cdot \mathbf{h}_{2I}^h d\Omega. \tag{3.21}
\end{aligned}$$

Here  $(\Gamma_{1I})_{\text{REF}}$  and  $(\Omega_{2I})_{\text{REF}}$  represent some reference configurations of  $\Gamma_{1I}$  and  $\Omega_{2I}$ , respectively, and  $\mathbf{x}_{1I}^h$  and  $\mathbf{x}_{2I}^h$  are the fluid mechanics and structural mechanics nodal positions at the fluid–structure interface. In reconciling the slightly modified notation used here with the notation used in Eqs. (3.1) and (3.13), we note that  $\rho_2 = \rho^s$ ,  $\mathbf{f}_2^h = \mathbf{f}^s$ ,  $(\Omega_2)_0 = \Omega_0^s$ ,  $\Omega_2 = \Omega_t^s$ , and  $\Omega_{2I}$  and  $\Omega_{2E}$  denote the partitions of  $\Omega_2$  corresponding to the interface and elsewhere. We also note that  $\mathbf{h}_{2I}^h = \mathbf{t}^h$ , and  $(\mathbf{h}_{11}^h)_A$  and  $(\mathbf{h}_{11}^h)_B$  represent the values of  $\mathbf{h}_{11}^h$  associated with the fluid surfaces above and below the membrane structure. The symbol  $\mathbf{h}_{2E}^h$  denotes the prescribed external forces acting on the structure in  $\Omega_{2E}$ , which is separate from  $\mathbf{f}_2^h$ . In this formulation,  $(\mathbf{u}_{11}^h)_{n+1}^-$ ,  $\mathbf{h}_{11}^h$  and  $\mathbf{h}_{2I}^h$  (the fluid velocity, fluid stress and structural stress at the fluid–structure interface) are treated as separate unknowns, and Eqs. (3.18), (3.19) and (3.20) can be seen as corresponding to these three unknowns, respectively. The structural displacement rate at the interface,  $\mathbf{u}_{2I}^h$ , is derived from  $\mathbf{y}^h$ .

We note that Eq. (3.19) has been derived by assuming that the viscous-flux jump

terms across inter-element borders are negligible. We also note that the last term of that equation, in its original form in [59], was written as a global integral  $\int_{Q_n}$  rather than a series of element-level integrals. Alternatively, as pointed out in [67], one can leave that projection equation in its form prior to the integration-by-parts:

$$\int_{(P_n)_h} (\mathbf{w}_{11}^h)_{n+1}^- \cdot \mathbf{h}_{11}^h dP = - \int_{(P_n)_h} (\mathbf{w}_{11}^h)_{n+1}^- \cdot p \mathbf{n} dP + \int_{(P_n)_h} (\mathbf{w}_{11}^h)_{n+1}^- \cdot (\mathbf{n} \cdot (2\mu \boldsymbol{\varepsilon}(\mathbf{u}))) dP, \quad (3.22)$$

and this would require also the projection of  $\boldsymbol{\varepsilon}(\mathbf{u})$  from the element interiors to the nodes.

The formulation given by Eqs. (3.15)–(3.21) is based on allowing for cases when the fluid and structure meshes at the interface are not identical. If they are identical, as pointed out in [59], the same formulation can still be used. Also as pointed out in [59], if the structure is represented by a 3D continuum model instead of a membrane model, the formulation above would still be applicable if the the domain integrations over  $\Omega_{2E}$  and  $\Omega_{2I}$  in the last two terms of Eq. (3.21) are converted to boundary integrations over  $\Gamma_{2E}$  and  $\Gamma_{2I}$ . In such cases,  $\mathbf{h}_{2E}^h$  would represent the prescribed forces acting “elsewhere” on the surface of the structure.

It was noted in [59] that, for constant viscosity, the term  $\nabla \cdot (2\mu \boldsymbol{\varepsilon}(\mathbf{u}))$  in Eq. (3.19) vanishes for tetrahedral elements and in most cases can be neglected for hexahedral elements. It was further noted in [59] that the same statement can be made also in the context of that term being a part of the expression  $\mathbf{L}(p^h, \mathbf{u}^h)$  appearing in Eqs. (3.15) and (3.16). In [59], the versions of the SSTFSI technique corresponding to the DSD/SST-DP, DSD/SST-SP and DSD/SST-TIP1 formulations (see Remarks 3–5) were called “SSTFSI-DP”, “SSTFSI-SP” and “SSTFSI-TIP1”, respectively.

# Chapter 4

## Special Modeling Techniques

The following chapter explains some of the special modeling techniques that have been developed by the T★AFSM to overcome the challenges of modeling arterial blood flow problems. Section 4.1 explains the method developed to separately project the pressure and viscous forces of the fluid to the structure and Section 4.2 shows a special mapping technique developed to handle non-circular inflow shapes. A preconditioning technique is shown in Section 4.3. A special boundary condition technique is explained in Section 4.4 that is used for inflow and outflow planes that are inclined to the cartesian planes. Sections 4.5 and 4.6 explain how the fluid mechanics results are evaluated to show fluid effects.

### 4.1 Separated Stress Projection

In the “Separated Stress Projection” (SSP) option proposed in [63], the pressure and viscous parts of the stress at the fluid interface are projected to the structure interface separately, pressure as a scalar and viscous stress as a vector. The projected parts are then combined while integrating the interface stresses in the structural mechanics equations. In the SSP option, the projections given by Eq. (3.19) and (3.20) are

replaced with the following projections:

$$\begin{aligned} \int_{(P_n)_h} (\mathbf{w}_{11}^h)_{n+1}^- \cdot (\mathbf{h}_v^h)_{11} dP &= \int_{Q_n} 2\mu\boldsymbol{\varepsilon}((\mathbf{w}_{11}^h)_{n+1}^-) : \boldsymbol{\varepsilon}(\mathbf{u}) dQ \\ &+ \sum_{e=1}^{(n_{el})_n} \int_{Q_n^e} (\mathbf{w}_{11}^h)_{n+1}^- \cdot \nabla \cdot (2\mu\boldsymbol{\varepsilon}(\mathbf{u})) dQ, \end{aligned} \quad (4.1)$$

$$\int_{(\Omega_{2I})_{\text{REF}}} q_{2I}^h (p_{2I}^h + (p_{1I}^h)_A - (p_{1I}^h)_B) d\Omega = 0, \quad (4.2)$$

$$\int_{(\Omega_{2I})_{\text{REF}}} \mathbf{w}_{2I}^h \cdot \left( (\mathbf{h}_v^h)_{2I} + ((\mathbf{h}_v^h)_{1I})_A + ((\mathbf{h}_v^h)_{1I})_B \right) d\Omega = 0, \quad (4.3)$$

$$\mathbf{h}_{2I}^h = -p_{2I}^h \mathbf{n}_{2I} + (\mathbf{h}_v^h)_{2I}, \quad (4.4)$$

where  $\mathbf{h}_v^h$  is the viscous part of the stress vector,  $p_{1I}^h$  is the pressure at the fluid interface,  $p_{2I}^h$  is the projection of that to the structure interface, and  $\mathbf{n}_{2I}$  is the unit normal vector at the structure interface. The stress vector at the structure interface, given by Eq. (4.4), is evaluated while integrating the interface stresses in the structural mechanics equations. Therefore, in the way Eq. (4.4) is used,  $\mathbf{n}_{2I}$  is evaluated at the integration point, and  $p_{2I}^h$  and  $(\mathbf{h}_v^h)_{2I}$  are the interpolated values at the integration point.

As an alternative to the projection given by Eq. (4.1), as pointed out in [67], one can leave that projection equation in its form prior to the integration-by-parts:

$$\int_{(P_n)_h} (\mathbf{w}_{11}^h)_{n+1}^- \cdot (\mathbf{h}_v^h)_{11} dP = \int_{(P_n)_h} (\mathbf{w}_{11}^h)_{n+1}^- \cdot (\mathbf{n} \cdot (2\mu\boldsymbol{\varepsilon}(\mathbf{u}))) dP, \quad (4.5)$$

which would correspond to Eq. (3.22) and would again require the projection of  $\boldsymbol{\varepsilon}(\mathbf{u})$  from the element interiors to the nodes.

Several remarks from [67] are summarized in the following.

**Remark 7** *The pressure projection given by Eq. (4.2) is solved by numerical substitution. It simplifies to direct substitution if the fluid and structure meshes at the*



*fluid–structure interface are identical.*

**Remark 8** *It was proposed in [40] that the “mass” matrix associated with the first term in Eq. (4.1) be lumped, pointing out that with this lumping the projection would become equivalent to a direct substitution, which would make the computations more efficient. This mass lumping would also be applicable to the first term in Eq. (4.5).*

**Remark 9** *As pointed out in [40], a smoother stress distribution is observed with a lumped mass matrix than with a consistent mass matrix.*

## 4.2 Mapping Technique for Inflow Boundaries

The special mapping technique for inflow boundaries was introduced in [39]. We repeat here from [39] the need for such a mapping technique and how the technique works.

Some inflow profiles require the inlet to be circular, however the inlets in many of the geometries we encounter are not circular. Furthermore, as the artery deforms, the inlet shape changes. Thus, even if the inlet is initially circular, it will not remain so. The technique introduced in [39] to meet this requirement maps the inflow boundaries from non-circular shapes to circular shapes. The actual inflow profile  $U(\mathbf{z}, t)$ , where  $\mathbf{z}$  is the coordinate vector in the inflow plane, is obtained by mapping from a preferred inflow profile  $U^P(r, t)$ . Here  $r$  is the circular coordinate and  $0 \leq r \leq r_B$ , where  $r_B$  is the average radius of the inflow cross-sectional area, which comes from the image-based data. It is calculated by dividing that area by  $\pi$  and taking the square-root of that.

The technique involves two steps:

1. Map  $\mathbf{z}$  to  $r$  and calculate a “trial” velocity:

$$r(\mathbf{z}) = \frac{\|\mathbf{z} - \mathbf{z}_C\|}{\|\mathbf{z} - \mathbf{z}_B\| + \|\mathbf{z} - \mathbf{z}_C\|} r_B, \quad (4.6)$$

$$U^T(\mathbf{z}, t) = U^P(r, t), \quad (4.7)$$

where subscripts “C” and “B” denote the centroid and the closest boundary, respectively, as shown in Figure 4.1, and the superscript “T” stands for “trial”.

2. Adjust the velocity:

$$U(\mathbf{z}, t) = \frac{Q(t)}{\int_{\Gamma_{\text{INFL}}} U^T(\mathbf{z}, t) d\Gamma} U^T(\mathbf{z}, t), \quad (4.8)$$

where  $Q$  is the flow rate and  $\Gamma_{\text{INFL}}$  is the discretized inflow area; i.e. the integration area in the finite element space.

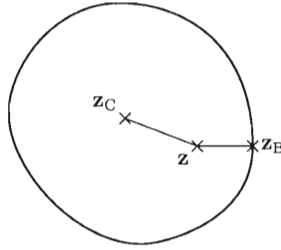


Figure 4.1: Special mapping technique.

### 4.3 Preconditioning Technique

In computations with hyperelastic materials, we do not compute the diagonal of the tangent stiffness matrix. Therefore, as proposed in [66], we use a diagonal preconditioner based on the assembly of only the element-level lumped mass matrices  $\mathbf{m}_{\text{LUMP}}^e$ , but after being multiplied by a factor that, to some extent, takes into account the material stiffness. In computations with the Fung material, for the multiplication factor, as proposed in [66], we use  $(C_{\text{HYFU}}^e)^2$ , where

$$C_{\text{HYFU}}^e = \max \left( \frac{\sqrt{\lambda^{\text{FP}}/\rho^s} \Delta t}{h^e}, \frac{\sqrt{\mu^{\text{FP}}/\rho^s} \Delta t}{h^e} \right). \quad (4.9)$$

Here  $h^e$  is the cube-root of the element volume, and  $\lambda^{\text{FP}}$  and  $\mu^{\text{FP}}$  are given as

$$\lambda^{\text{FP}} = \frac{6D_1D_2\nu_{\text{PEN}}}{(1 + \nu_{\text{PEN}})(1 - 2\nu_{\text{PEN}})}, \quad \mu^{\text{FP}} = \frac{3D_1D_2}{(1 + \nu_{\text{PEN}})}. \quad (4.10)$$

In [66],  $[1 + (1 - \alpha)\beta (2 C_{\text{HYFU}}^e)^2]$  was proposed as an alternative multiplication factor, where  $\alpha$  and  $\beta$  are the time-integration parameters mentioned in Section 3.2.

Several remarks from [67] are summarized in the following.

**Remark 10** *We use the “Selective Scaling” technique (see Remark 14 in [59]) to shift the emphasis between the fluid and structure parts. As pointed out in [39], the preconditioner described in this section improves, within the fluid+structure block, the relative scaling between the fluid and structure parts and provides a better beginning point for selective scaling, if we still find a need to use such a scaling.*

**Remark 11** *In its originally-proposed form in [59], the Selective Scaling technique was intended to shift the emphasis between the fluid and structure parts when used with the quasi-direct coupling technique, and between the fluid, structure and mesh-moving parts when used with a direct coupling technique (see [61, 59] for the terminology). In [41] it was extended to also shifting the emphasis between the parts of the fluid mechanics equations corresponding to the momentum conservation and incompressibility constraint.*

## 4.4 Boundary Condition Techniques for Inclined Inflow and Outflow Planes

In earlier arterial FSI computations [64, 66, 39, 69, 40] with the SSTFSI technique, the inflow and outflow planes were parallel to the Cartesian coordinate planes, and slip boundary conditions were imposed on those planes for the structural mechanics and

mesh-moving equations. With the techniques introduced in [41], such slip boundary conditions were extended to inclined inflow and outflow planes. Here we describe those techniques from [41].

#### 4.4.1 Structural Mechanics Equations

The unknown space for the structural mechanics nodes at the inflow and outflow planes is rotated in such a way that one of the directions is perpendicular to the plane. The normal vector of the plane,  $\mathbf{n}_{S2}$ , is calculated for each arterial end by the area-weighted average of the normal vectors of the element surfaces at that end, where the subscripts ‘‘S’’ and ‘‘2’’ refer to the slip plane and the structural mechanics equations. With that, the normal component of the structural displacement is set to zero.

#### 4.4.2 Mesh-Moving Equations

The fluid mechanics nodal positions calculated with Eq. (3.17) include the positions of the rim nodes at the lumen ends. However, as pointed out in [41], there is no guarantee that those nodes would all be on the same plane. As proposed in [41], we bring them all to the same plane by adjusting their positions as follows:

$$(\mathbf{x}_{1I}^h)_{n+1} \leftarrow (\mathbf{x}_{1I}^h)_{n+1} + \left( ((\mathbf{x}_{S1}^h)_{n+1} - (\mathbf{x}_{1I}^h)_{n+1}) \cdot \frac{\mathbf{n}_{S1}}{\|\mathbf{n}_{S1}\|} \right) \frac{\mathbf{n}_{S1}}{\|\mathbf{n}_{S1}\|}, \quad (4.11)$$

where  $\mathbf{x}_{S1}^h$  is the centroid of the set of fluid element edges coinciding with the rim, and the normal vector of the plane,  $\mathbf{n}_{S1}$ , is calculated by using the following expression:

$$\mathbf{n}_{S1} = \sum_{k=1}^{N_{S1}} ((\mathbf{x}_L^k)_{n+1} - (\mathbf{x}_{S1}^h)_{n+1}) \times ((\mathbf{x}_R^k)_{n+1} - (\mathbf{x}_{S1}^h)_{n+1}). \quad (4.12)$$

Here  $N_{s1}$  is the number of element edges coinciding with the rim, and  $(\mathbf{x}_L^k)_{n+1}$  and  $(\mathbf{x}_R^k)_{n+1}$  are the positions of the left and right nodes of the  $k^{th}$  edge. We apply the adjustment of Eq. (4.11) also to the other nodes of the inflow and outflow boundaries. With  $\mathbf{n}_{s1}$  given for each inflow and outflow boundary, the fluid mechanics mesh-moving equations are solved with slip condition at the inflow and outflow planes, in the same way the structural mechanics equations are solved.

## 4.5 Wall Shear Stress Calculation

A new technique for calculating the wall shear stress (WSS) was proposed in [40]. We provide the description of the technique from [40].

We first decompose the spatial version of  $(\mathbf{w}_{11}^h)_{n+1}^-$  into its two components:

$$\mathbf{w}_{11}^h = (\mathbf{w}_{11}^h)^W + (\mathbf{w}_{11}^h)^R, \quad (4.13)$$

where  $(\mathbf{w}_{11}^h)^R$  is the part associated with the rim nodes at the lumen ends, and  $(\mathbf{w}_{11}^h)^W$  is the part associated with the rest of the fluid mechanics nodes at the arterial wall.

We then calculate  $(\mathbf{h}_v^h)_{11}$  as follows:

$$\int_{\Gamma_h} (\mathbf{w}_{11}^h)^W \cdot (\mathbf{h}_v^h)_{11} \, d\Gamma = \int_{\Omega} 2\mu \boldsymbol{\varepsilon}((\mathbf{w}_{11}^h)^W) : \boldsymbol{\varepsilon}(\mathbf{u}) \, d\Omega + \sum_{e=1}^{(n_{el})n} \int_{\Omega^e} (\mathbf{w}_{11}^h)^W \cdot \nabla \cdot (2\mu \boldsymbol{\varepsilon}(\mathbf{u})) \, d\Omega, \quad (4.14)$$

$$\int_{\Gamma_h} (\mathbf{w}_{11}^h)^R \cdot ((\mathbf{n} \times \mathbf{e}^R) \cdot \nabla) (\mathbf{h}_v^h)_{11} \, d\Gamma = 0, \quad (4.15)$$

where  $\mathbf{e}^R$  is the unit vector along the rim.

## 4.6 Oscillatory Shear Index

The oscillatory shear index (OSI) is a measure of the degree to which WSS oscillates during a heart beat cycle. It is defined (see [49]) as follows:

$$\text{OSI} = \frac{1}{2} \left( 1 - \frac{(\mathbf{h}_v^h)_{\text{II}}^{\text{NM}}}{(\mathbf{h}_v^h)_{\text{II}}^{\text{MN}}} \right), \quad (4.16)$$

where, following the notation from [40], “NM” and “MN” stand for “norm of the mean” and “mean of the norm”, and

$$(\mathbf{h}_v^h)_{\text{II}}^{\text{NM}} = \frac{1}{T} \left\| \int_0^T (\mathbf{h}_v^h)_{\text{II}} dt \right\|, \quad (4.17)$$

$$(\mathbf{h}_v^h)_{\text{II}}^{\text{MN}} = \frac{1}{T} \int_0^T \| (\mathbf{h}_v^h)_{\text{II}} \| dt. \quad (4.18)$$

Here  $T$  is the period of the cardiac cycle. Higher OSI indicates larger flow direction variation in a cardiac cycle. As pointed out in [40], calculating the OSI based on a fixed reference frame is not the best way, because, for example, if an artery segment undergoes rigid-body rotation, that should not influence the OSI. Two methods that exclude rigid-body rotation from the OSI calculation were proposed in [40].

*Method 1*

$$(\mathbf{h}_v^h)_{\text{II}}^{\Delta} = J\mathbf{F}^{-1}(\mathbf{h}_v^h)_{\text{II}}, \quad (4.19)$$

where  $\mathbf{F}$  is the deformation gradient tensor associated with the deformation of the fluid-structure interface (not the volumetric deformation gradient of the fluid-domain motion), and  $J = \det \mathbf{F}$ .

*Method 2*

$$(\mathbf{h}_v^h)_{\text{II}}^{\Delta} = \mathbf{R}^T(\mathbf{h}_v^h)_{\text{II}}, \quad (4.20)$$

where  $\mathbf{R}$  is the rotation tensor coming from the decomposition of  $\mathbf{F}$  as

$$\mathbf{F} = \mathbf{R}\mathbf{U}, \quad (4.21)$$

and  $\mathbf{U}$  is the right stretch tensor.

For both methods,  $(\mathbf{h}_v^h)_{\text{II}}^\Delta$  is calculated as follows:

$$\int_{(\Gamma_{\text{II}})_{\text{ROSI}}} \mathbf{w}_{\text{II}}^h \cdot (\mathbf{h}_v^h)_{\text{II}}^\Delta d\Gamma = \int_{(\Gamma_{\text{II}})_{\text{ROSI}}} \mathbf{w}_{\text{II}}^h \cdot \mathcal{R} (\mathbf{h}_v^h)_{\text{II}} d\Gamma, \quad (4.22)$$

where  $\mathcal{R} = J\mathbf{F}^{-1}$  or  $\mathcal{R} = \mathbf{R}^T$ , and  $(\Gamma_{\text{II}})_{\text{ROSI}}$  is a reference configuration of the fluid–structure interface used in the OSI calculations. In Eqs. (4.17) and (4.18), we replace  $(\mathbf{h}_v^h)_{\text{II}}$  with  $(\mathbf{h}_v^h)_{\text{II}}^\Delta$ .

Several remarks from [67] are summarized in the following.

**Remark 12** *The OSI calculations reported in this paper are based on Eq. (4.19).*

**Remark 13** *As pointed out in [40], the reference configuration used in Eq. (4.22) is not necessarily the unstressed configuration of the fluid–structure interface. For the calculations reported in this paper, it is the configuration corresponding to the instant when the pressure is at its time-averaged value (on the way up, i.e. at the ascending part of the pressure curve).*

# Chapter 5

## Mesh Generation and Simulation Conditions

In any computational problem, the spatial discretization can be among the most difficult tasks. In Sections 5.1 and 5.2, we explain the process used in mesh generation for the patient-specific models. Sections 5.3 and 5.4 show the fluid and structure properties as well as boundary conditions for the computations. Section 5.6 explains the simulation sequences for all techniques used including the simpler approaches to FSI modeling.

### 5.1 Arterial-Surface Extraction from Medical Images

In our current arterial FSI research the arterial geometries come as voxel data from 3D rotational angiography (3DRA) performed at one of the neuroangiography suites at the Memorial Hermann Hospital at the Texas Medical Center. This is done on a biplane neuroangiographic unit (Allura FD20/10; Philips Medical System, Best, the Netherlands). Adjusting the contrast ratio for this voxel data allows us to visualize



and create a triangular surface mesh using a marching cubes algorithm. The vertices of the surface mesh are then passed through a Gaussian smoothing filter to eliminate any high frequency noise and obtain a smooth surface. At the artery inlets and outlets, we select cutting planes that are approximately perpendicular to the flow direction. As pointed out in [41], this provides better inflow and outflow planes for specifying the fluid mechanics boundary conditions and is also important for imposing proper slip boundary conditions at the inlets and outlets for the structural mechanics and fluid mesh motion (see Section 4.4). This entire process is carried out using software originally designed by Warren and McPhail for the purpose of interactively imaging the pulmonary structure of the human lung [31].

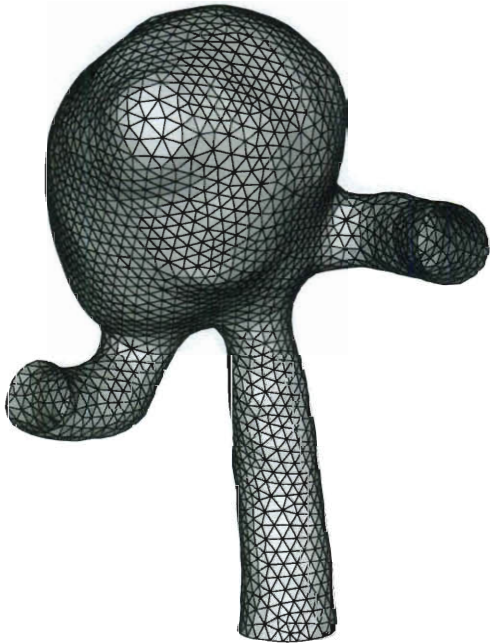
## 5.2 Mesh Generation and Estimated Zero Pressure Geometry

We begin by giving an overview of the mesh generation process. In the process outlined above, we see the artery model as composed of “patches”. The patches are identified as the regions associated with the inflow trunk, each of the outflow branches, and the aneurysm/bifurcation area. The process of mesh generation begins by generating a structural mechanics mesh from the arterial lumen geometry that corresponds to an estimated zero-pressure (EZP) arterial geometry [64, 39, 68, 40]. The structural mechanics mesh consists of two layers of hexahedral elements with varying thickness. The mesh is then inflated from zero-pressure to the average pressure of the cardiac cycle (92 mm Hg). After inflation, we seek to maintain a 10% wall-thickness ratio (relative to the diameter of the arterial lumen) at inflow and outflow boundaries. Then, once re-inflated to the starting pressure of the cardiac cycle (near 80 mm Hg), we generate a fluid mechanics mesh of tetrahedral elements that has a desired number of layers of refined fluid mechanics volume mesh near the arte-

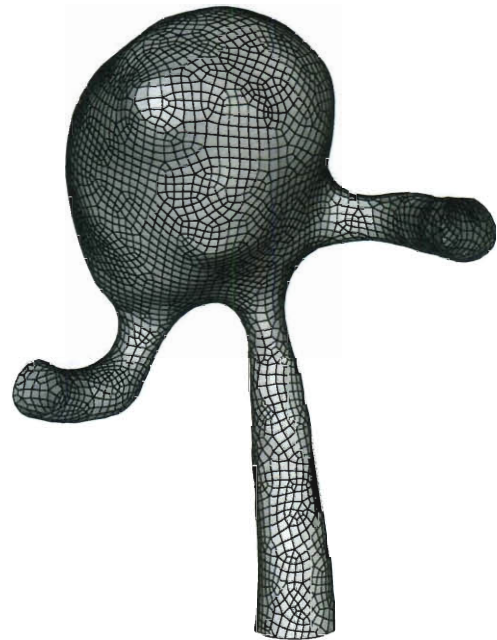
rial walls. As mentioned in [41], at locations where the arteries have large curvature we use more mesh refinement.

The concept of EZP geometry was introduced in [64]. As pointed out in [64], we assume that the extracted arterial lumen geometry corresponds to the shape at the time-averaged value of the blood pressure. Given that arterial geometry at the time-averaged pressure value, an estimated arterial geometry corresponding to zero blood pressure needs to be constructed. In estimating that geometry, the time-averaged value of the blood pressure, obtained by averaging over a cardiac cycle, is 92 mm Hg.

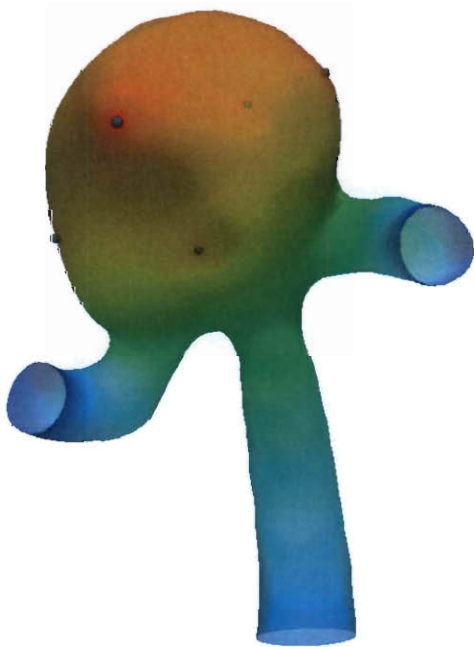
The progression of the structural mechanics mesh generation process is shown in Figure 5.3. We begin by generating the structural mechanics mesh using the arterial lumen geometry from surface-extraction (see Section 5.1) as input to ANSYS Meshing Tools and generate a triangular surface mesh as shown in Figure 5.1a. This mesh is then shrunk an appropriate distance, re-meshed as a quadrilateral surface mesh (Figure 5.1b), and given a thickness to diameter ratio of about 12–13% so that it corresponds to EZP geometry. The shrinking amount and wall-thickness are determined based on the objective to have an EZP geometry that, after inflation to average pressure, gives us a shape that closely resembles the lumen geometry from the 3DRA with new thickness to diameter ratios of 10% at the inflow and outflow boundaries. The inflation to average pressure is dependent on both the shrinking amount and the wall-thickness as related by the incompressibility constraint. We iterate on the values of shrinking amount and wall-thickness until we achieve our stated objective. The shrinking amount and wall-thickness are specified at the inflow and outflow boundaries. The Laplace’s equation is then solved over the surface mesh covering the lumen. In some cases where the outflow diameters significantly differ, the solution obtained from the Laplace’s equation for shrinking amount and wall-thickness could have undesirable distribution for the aneurysm/bifurcation patch. In these cases, the shrinking amount and wall-thickness are prescribed at a set of inter-



(a) Surface mesh of triangular elements of the arterial lumen geometry extracted from 3DRA.



(b) Surface mesh of quadrilateral elements after the shrinking process.



(c) Shrinking amount over the arterial lumen geometry extracted from 3DRA. Dots represent inter-patch points where shrinking amount is prescribed.



(d) Wall-thickness over the surface mesh after shrinking.

Figure 5.1: Structural mechanics mesh generation process for a sample model. The color range represents red (large) to blue (small).

patch points (i.e. points that are considered to be at the boundaries between the patches). Figure 5.1c is an example of the shrinking amount and the necessity to define the shrinking amount at a set of inter-patch points. Figure 5.1d shows an example of the wall-thickness amount on the shrunk surface geometry. Figure 5.2 shows the resultant hexahedral structural mechanics mesh for a sample artery. The shrinking method is applied, as needed, in multiple steps (typically 2), with surface remeshing between the steps in order to maintain the geometry at points of high curvature. Because the parameter space is wider and the targets are multiple, the mesh generation process involves more user experience, intuition and judgment.

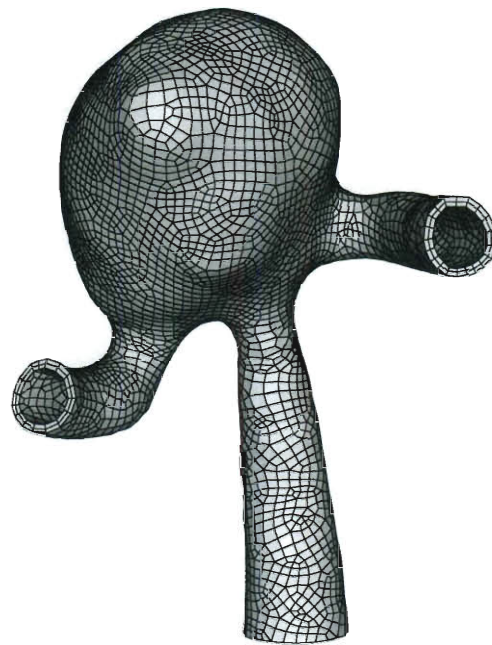


Figure 5.2: Structural mechanics mesh of hexahedral elements at zero-pressure.

The fluid mesh generation process begins by extracting the inner surface of the structural mechanics mesh after it has been inflated to the starting pressure of our cardiac cycle (near 80 mm Hg). After that, we generate, with ANSYS Meshing Tools, a fluid mechanics surface mesh of triangular elements. Then, using that surface mesh, we generate a desired number of layers of refined fluid mechanics volume mesh near the arterial walls. The thickness of these layers is determined much the same as the

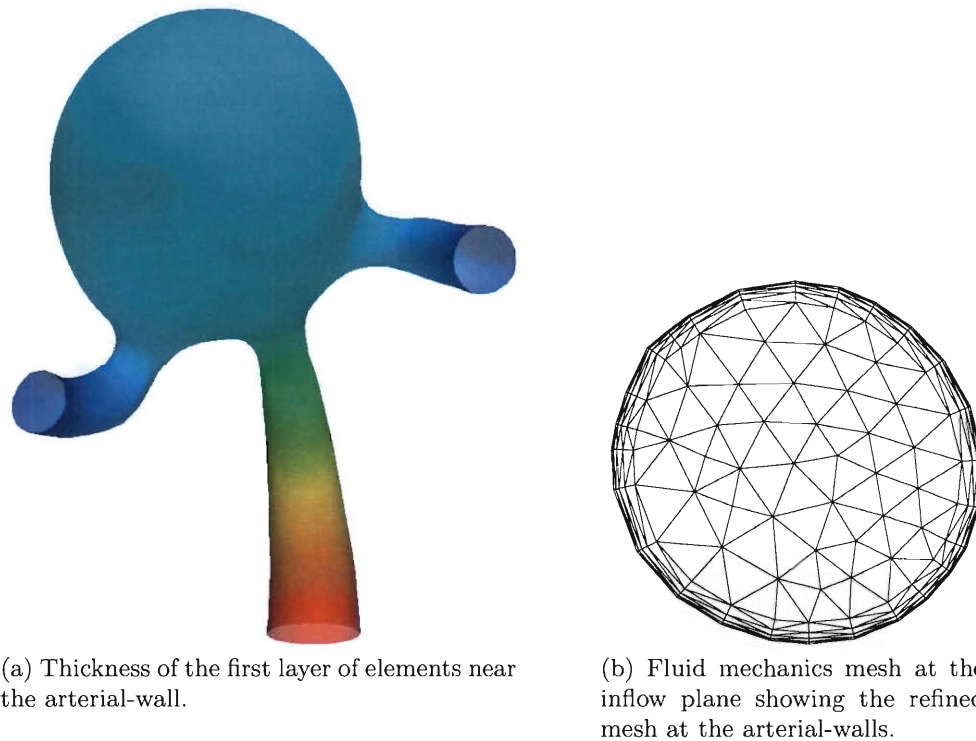


Figure 5.3: Fluid mechanics mesh generation process for a sample model. The color range represents red (large) to blue (small).

wall-thickness amount is determined in [41]. The thickness of the layers are prescribed for the inflow and outflow boundaries. The thickness of the first layer of elements at the inflow and outflow boundaries is  $0.007 \times (\text{lumen diameter at those ends})$ . The Laplace's equation is then solved over the surface mesh as shown in Figure 5.3a. In generating the refined fluid mechanics volume mesh near the arterial walls, the number of layers is 4 and the progression ratio is 1.75 as shown in Figure 5.3b. The rest of the fluid mechanics volume mesh is generated with the T★AFSM automatic mesh generator. Figure 5.4 shows the fluid volume mesh for a sample artery.

### 5.3 Fluid and Structure Properties

As it was done for the computations reported in [71, 72, 73, 74, 75], the blood is assumed to behave like a Newtonian fluid (see Section 2.1 in [64]). The density



Figure 5.4: Fluid mechanics mesh of tetrahedral elements at starting pressure.

and kinematic viscosity are set to  $1,000 \text{ kg/m}^3$  and  $4.0 \times 10^{-6} \text{ m}^2/\text{s}$ . The material density of the arterial wall is known to be close to that of the blood and therefore set to  $1,000 \text{ kg/m}^3$ . The arterial wall is modeled with the continuum element made of hyperelastic (Fung) material. The Fung material constants  $D_1$  and  $D_2$  (from [21]) are  $2.6447 \times 10^3 \text{ N/m}^2$  and  $8.365$ , and the penalty Poisson's ratio is  $0.45$ . Cerebral arteries are surrounded by cerebrospinal fluid, and we expect that to have a damping effect on the structural dynamics of the arteries. Therefore we add a mass-proportional damping, which also helps in removing the high-frequency modes of the structural deformation. The damping coefficient  $\eta$  is chosen in such a way that the structural mechanics computations remain stable at the time-step size used. It is  $1.5 \times 10^4 \text{ s}^{-1}$ .

## 5.4 Boundary Conditions

At the inflow boundary we specify the velocity profile as a function of time, by using the technique introduced in [39]. Here we describe the technique from [39]. We

use a velocity waveform which represents the cross-sectional maximum velocity as a function of time. Assuming that the maximum velocity occurs at  $r = 0$ , the artery is rigid and the cross-sectional shape is a perfect circle, we can apply the Womersley [83] solution as follows:

$$U^P(r, t) = A_0 \left( 1 - \left( \frac{r}{r_B} \right)^2 \right) + \sum_{k=1}^N A_k \frac{J_0(\Upsilon \sqrt{k} i^{\frac{3}{2}}) - J_0(\Upsilon \sqrt{k} \left( \frac{r}{r_B} \right) i^{\frac{3}{2}})}{J_0(\Upsilon \sqrt{k} i^{\frac{3}{2}}) - 1} \exp \left( i 2\pi k \frac{t}{T} \right), \quad (5.1)$$

where  $N$  is the number of Fourier coefficients (we use  $N = 20$ ),  $A_k \in \mathbb{C}$  are the Fourier coefficients of the waveform,  $T$  is the period of the cardiac cycle,  $J_0$  is the Bessel functions of the first kind of order 0,  $i$  is the imaginary number, and  $\Upsilon$  is the Womersley parameter:

$$\Upsilon = r_B \sqrt{\frac{2\pi}{\nu T}}. \quad (5.2)$$

We use the special mapping technique described in Section 4.2 for non-circular shapes. The volumetric flow rate (which was calculated based on a velocity waveform that represents the cross-sectional maximum velocity) is scaled by a factor. The scaling factor is determined in such a way that the scaled flow rate, when averaged over the cardiac cycle, yields a target WSS for Poiseuille flow over an equivalent cross-sectional area. The target WSS is 10 dyn/cm<sup>2</sup> in the current T★AFSM computations. Figure 5.5 shows a sample volumetric flow rate as a function of time.

At all outflow boundaries of an artery segment, we specify the same traction boundary condition. The traction boundary condition is based on a pressure profile computed as described in [39]. In that computation, the pressure profile, as a function of time, is determined based on the flow rate and by using the Windkessel model [17].

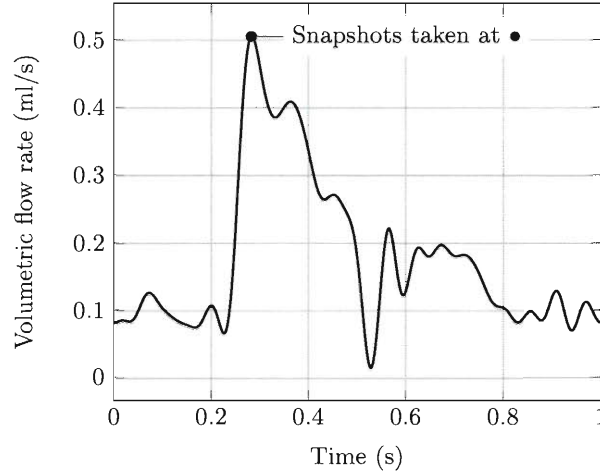


Figure 5.5: Sample volumetric flow rate.

From Eq. (5.1), we obtain the flow rate as follows:

$$Q(t) = \int_0^{r_B} 2\pi r U^P(r, t) dr \quad (5.3)$$

$$= \pi r_B^2 \frac{A_0}{2} + \pi r_B^2 \sum_{n=1}^N A_k \frac{J_0(\Upsilon \sqrt{k} i^{\frac{3}{2}}) - 2 \left( \Upsilon \sqrt{k} i^{\frac{3}{2}} \right)^{-1} J_1(\Upsilon \sqrt{k} i^{\frac{3}{2}})}{J_0(\Upsilon \sqrt{k} i^{\frac{3}{2}}) - 1} \exp \left( i 2\pi k \frac{t}{T} \right) \quad (5.4)$$

$$= \sum_{k=0}^N B_k \exp \left( i 2\pi k \frac{t}{T} \right), \quad (5.5)$$

where  $J_1$  is the Bessel functions of the first kind of order 1, and for notational convenience we introduce another set of coefficients,  $B_k \in \mathbb{C}$ . The pressure, based on the Windkessel model, can be written as follows:

$$p(t) = \exp \left( -\frac{t}{RC} \right) \int_0^t \frac{1}{C} Q(\tau) \exp \left( \frac{\tau}{RC} \right) d\tau + p_0, \quad (5.6)$$

where  $C$  and  $R$  are the compliance and resistance of the distal arterial networks, and  $p_0$  is a constant of integration. Substituting Eq. (5.5) into Eq. (5.6), we obtain the



following:

$$p(t) = \sum_{k=0}^N \frac{B_k}{i2\pi k \frac{C}{T} + \frac{1}{R}} \left[ \exp\left(i2\pi k \frac{t}{T}\right) - \exp\left(-\frac{t}{RC}\right) \right] + p_0. \quad (5.7)$$

After a sufficient number of periods, the  $\exp\left(-\frac{t}{RC}\right)$  term in Eq. (5.7) goes to 0:

$$p(t) = \frac{T}{C} \sum_{k=0}^N \frac{B_k}{i2\pi k + \frac{T}{RC}} \exp\left(i2\pi k \frac{t}{T}\right) + p_0. \quad (5.8)$$

Here  $\frac{T}{RC}$  is only a profile factor, because it is a parameter that only acts on each Fourier coefficient. We set  $\frac{T}{RC}$  to 18.2, and the other parameters,  $\frac{T}{C}$  and  $p_0$ , are set in such a way that the range for the pressure profile is from 80 to 120 mm Hg for normal blood pressure. Figure 5.6 shows the pressure profile corresponding to the sample flow rate shown in Figure 5.5.

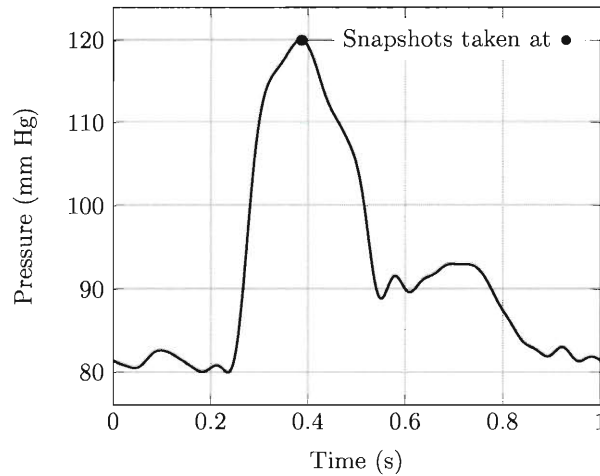


Figure 5.6: Sample outflow pressure profile corresponding to the sample flow rate shown in Figure 5.5.

On the arterial walls, we specify no-slip boundary conditions for the flow. In the structural mechanics part, as boundary condition at the ends of the arteries, we set the normal component of the displacement to zero (see Section 4.4), and for one of those nodes we also set to zero the tangential displacement component that needs to

be specified to preclude rigid-body motion.

## 5.5 Computational Conditions

The computations are carried out with the SSTFSI-TIP1 technique (see Section 3.3) and the SUPG test function option WTSA (see Remark 1). The stabilization parameters used are those given by Eqs. (3.3)–(3.8). We do not use the “LSIC” stabilization (see Eq. (3.9) for meaning). The SSP option is used fully (see Section 4.1). The time-step size is  $3.333 \times 10^{-3}$  s. The number of nonlinear iterations per time step is 6. The number of GMRES iterations per nonlinear iteration for the fluid+structure block was chosen such that mass balance is satisfied to within at most 5% for each case. For all six nonlinear iterations the fluid scale is 1.0 and the structure scale is 100. In three of the cases, the fluid scales for the momentum conservation and incompressibility constraint are 1.0 and 10. For the mesh moving block the number of GMRES iterations is 30. All computations were carried out in a parallel computing environment and were completed without any remeshing.

## 5.6 Simulation Sequence

We compute all ten of the aneurysm cases with the four following techniques: Fluid–Structure Interaction (FSI), Rigid Artery (RA), Structure (S), and Prescribed Shape (PS). The FSI technique is the most thorough technique while the other three are simpler approaches aimed at saving time. The accuracy of the simpler approaches will be studied in later Chapters.

### 5.6.1 Fluid–Structure Interaction (FSI)

Recipes for pre-FSI computations that provide a good starting point for the FSI computations and improve their convergence were introduced in [60]. Now, in all arterial simulations carried out by the T★AFSM, the FSI computations are preceded by a set of pre-FSI computations. These pre-FSI computations include fluid-only and structure-only computations. The recipes introduced in [60] were used also in [64, 66]. A slightly modified recipe was introduced in [39], resulting in a simulation sequence called “S→F→S→FSI”, and this is the one that the T★AFSM has been using in its arterial simulations since then.

#### **Structure→Fluid→Structure→FSI (S→F→S→FSI) sequence**

**Step 1:** Generate the structural mechanics mesh based on the shape of the unstressed structure.

**Step 2:** Compute the structural deformation with a uniform fluid pressure held steady at a value close to 80 mm Hg (100 mm Hg for high blood pressure).

- Structural deformation can be determined with a steady-state computation or a time-dependent computation that eventually yields a steady-state solution.
- For the steady-state computation,  $\Delta t \rightarrow \infty$  and  $\alpha = 0$  in Eq. (3.14), the number of time steps is one, and the initial displacement, velocity and acceleration are set to zero.

**Step 3:** Generate the fluid mesh based on the shape of the deformed structure.

**Step 4:** Compute a developed flow field while holding the structure from Step 2 rigid.

- The outflow traction is set to a value close to 80 mm Hg.
- The inflow velocity is set to a value corresponding to the outflow traction.

**Step 5:** Recompute the structural deformation, with the fluid stresses at the interface held steady at their values from Step 4, and simultaneously update the fluid mesh.

- Structural deformation can be determined with one of the two choices we had in Step 2.

**Step 6:** Compute the FSI with the same inflow and outflow conditions used in Step 4, with the initial condition for the flow velocity coming from Step 4.

**Step 7:** Compute the FSI with the inflow and outflow conditions pulsating.

### 5.6.2 Rigid Artery (RA)

The RA technique involves computing the blood flow with the artery shape held fixed at the average pressure (92 mm Hg).

**Step 1:** Compute the structural deformation starting at the output from Step 2 of the FSI sequence and ramping the uniform fluid pressure from 80 mm Hg (referred to as starting pressure) to 92 mm Hg (referred to as average pressure).

**Step 2:** Move the developed flow field fluid mesh from the output of Step 4 of the FSI sequence to the new structural position at average pressure.

**Step 3:** Compute the blood flow with pulsating conditions while holding the structure rigid at the average pressure (92 mm Hg).

- The inflow velocity is set to the profile in Figure 5.5.
- The outflow traction is set to the profile in Figure 5.6.

### 5.6.3 Structure (S)

The Structure technique involves computing the arterial-wall deformation with a prescribed, time-dependent pressure.

**Step 1:** Compute the structural deformation starting at the output from Step 2 of the FSI sequence using a uniform fluid pressure profile as seen in Figure 5.6.

#### 5.6.4 Prescribed Shape (PS)

The PS technique involves computing the pulsating blood flow with the prescribed arterial shape coming from the Structure computation.

**Step 1:** Compute the blood flow with pulsating conditions while prescribing the structural shape as the output of Step 1 of the Structure technique.

- The inflow velocity is set to the profile in Figure 5.5.

# Chapter 6

## Computational Results

This chapter introduces the computational models and shows results of the comparative study as well as the simpler approaches to modeling. Section 6.1 gives the problem description for each of the ten cases studied. Section 6.2 compares the WSS, OSI, and arterial-wall stress and stretch between the ruptured and unruptured aneurysms. In Section 6.3 we compare the results of the simpler modeling approaches to the FSI modeling results. The mesh refinement results are shown in Section 6.4.

### 6.1 Computational Models

Ten arterial cases are studied from three locations: 4 Middle Cerebral Artery (MCA), 4 Anterior Communicating Artery (Acom), and 2 Basilar Artery. Half of each location were ruptured. Figure 6.1 shows the lumen geometries for the MCA, Acom, and Basilar locations. The physical parameters for each model are shown in Table 6.1.











MCA			
			
M1MCA Unruptured	M2MCA Unruptured	M3MCA Ruptured	M4MCA Ruptured
Acom			
			
M5Acom Unruptured	M6Acom Unruptured	M7Acom Ruptured	M8Acom Ruptured
Basilar			
			
M9Basilar Unruptured	M10Basilar Ruptured		

Figure 6.1: Arterial lumen geometry obtained from voxel data for the ten models studied.

Model	$D_I$	$D_{O1}$	$D_{O2}$	$D_{O3}$	$D_{O4}$	$\Upsilon$	$Q_{\max}$
M1MCA	2.43	2.42	1.87			1.52	0.51
M2MCA	1.56	1.41	1.38			0.97	0.12
M3MCA	2.50	1.49	1.43			1.57	0.56
M4MCA	1.70	1.21	0.81			1.06	0.16
M5Acom	3.05	1.78	1.75			1.91	1.08
M6Acom	3.13	2.12	2.12			1.96	1.20
M7Acom	1.02	0.90	0.80			0.64	0.04
M8Acom	1.94	2.31	2.17	1.38		1.21	0.25
M9Basilar	2.60	1.31	1.01	0.88		1.63	0.64
M10Basilar	3.03	1.34	1.04	1.01	0.93	1.90	1.06

Table 6.1: Physical parameters for the ten arterial models. Diameters are in mm and peak volumetric flow rate is in ml/s.

The structural mechanics meshes for the MCA, Acom, and Basilar locations are shown in Figures 6.2, 6.3 and 6.4, respectively. The node and element numbers for all the models' structural mechanics meshes are given in Table 6.2. The fluid mechanics meshes for the MCA, Acom, and Basilar locations are shown in Figures 6.5, 6.6 and 6.7, respectively. The node and element numbers for all the models' fluid mechanics meshes are given in Table 6.3. The computational parameters for each model are shown in Table 6.4. As explained in Section 5.5, to determine if the computation was successful, we observe the mass balance for the arterial model. Good mass balance is achieved when the difference between the inflow and outflow rates equals the change in volume of the artery over the cardiac cycle. Figures 6.8–6.17 show the mass balance for all the models.



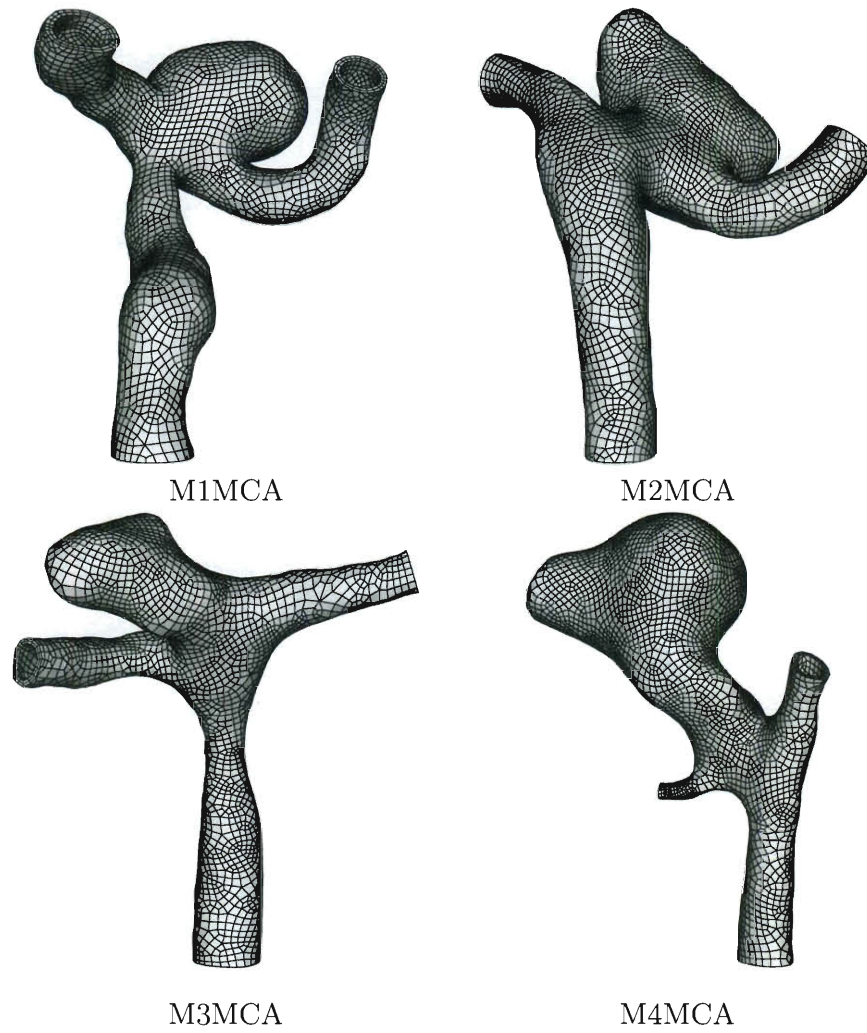


Figure 6.2: Structural mechanics meshes at zero pressure for the MCA models.

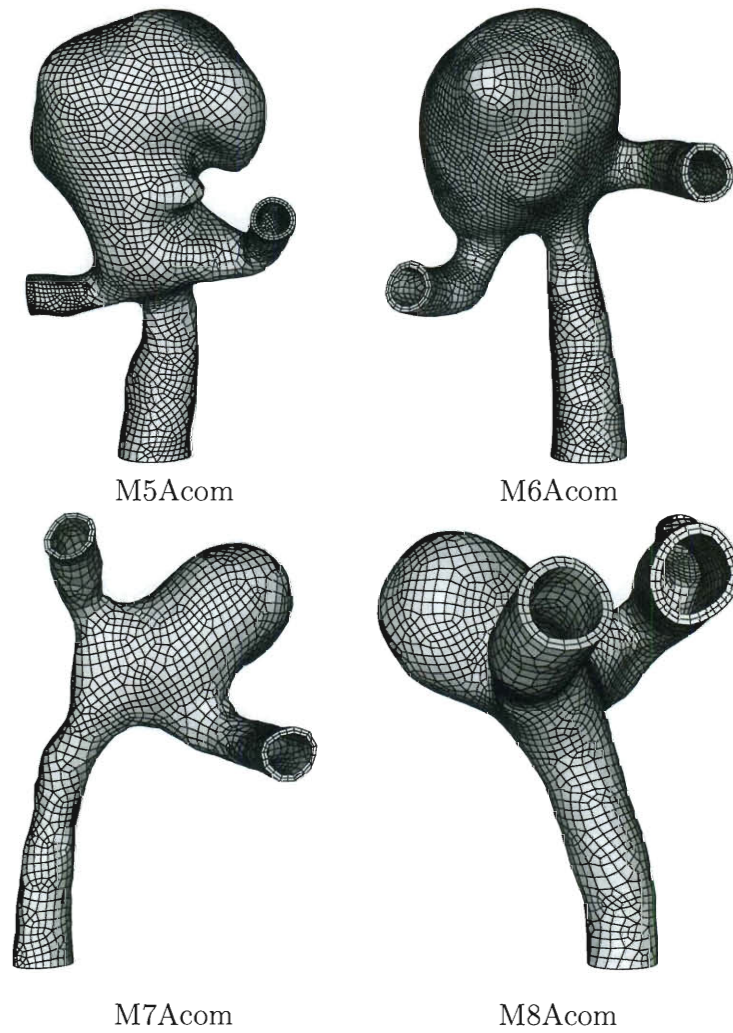


Figure 6.3: Structural mechanics meshes at zero pressure for the Acom models.

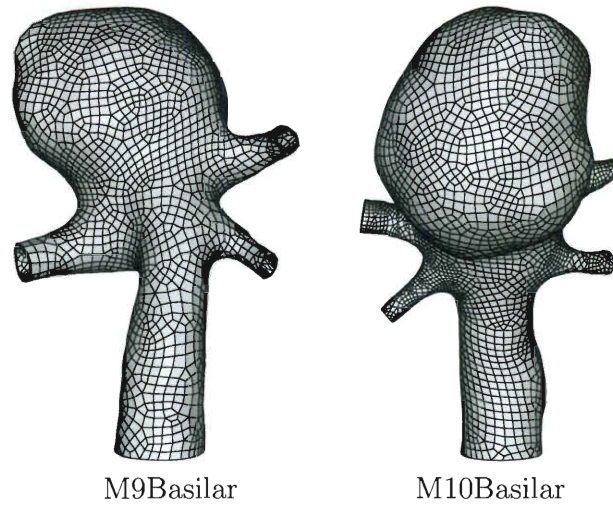


Figure 6.4: Structural mechanics meshes at zero pressure for the Basilar models.

	Structure			
	Volume		Interface	
	$nn$	$ne$	$nn$	$ne$
M1MCA	14,670	9,700	4,890	4,850
M2MCA	17,568	11,640	5,856	5,820
M3MCA	12,927	8,550	4,309	4,275
M4MCA	17,244	11,432	5,748	5,716
M5Acom	14,757	9,752	4,919	4,876
M6Acom	17,574	11,650	5,858	5,825
M7Acom	8,046	5,304	2,682	2,652
M8Acom	11,436	7,538	3,812	3,769
M9Basilar	11,886	7,862	3,962	3,931
M10Basilar	16,128	10,652	5,376	5,326

Table 6.2: Number of nodes and elements for the structural mechanics mesh of each of the ten arterial models. Here  $nn$  and  $ne$  are number of nodes and elements, respectively.

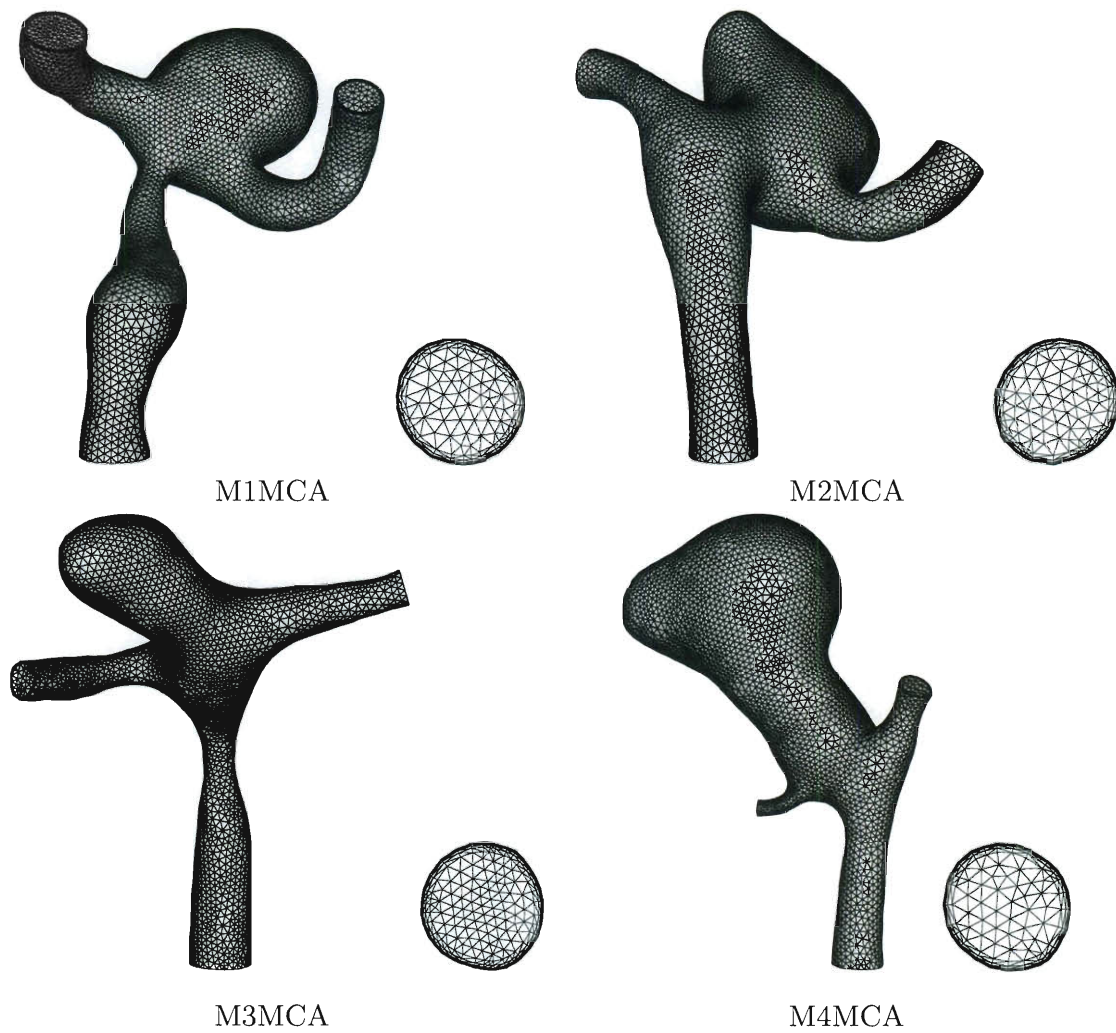


Figure 6.5: Fluid mechanics meshes at starting pressure at the fluid–structure interface and inflow plane for the MCA models.

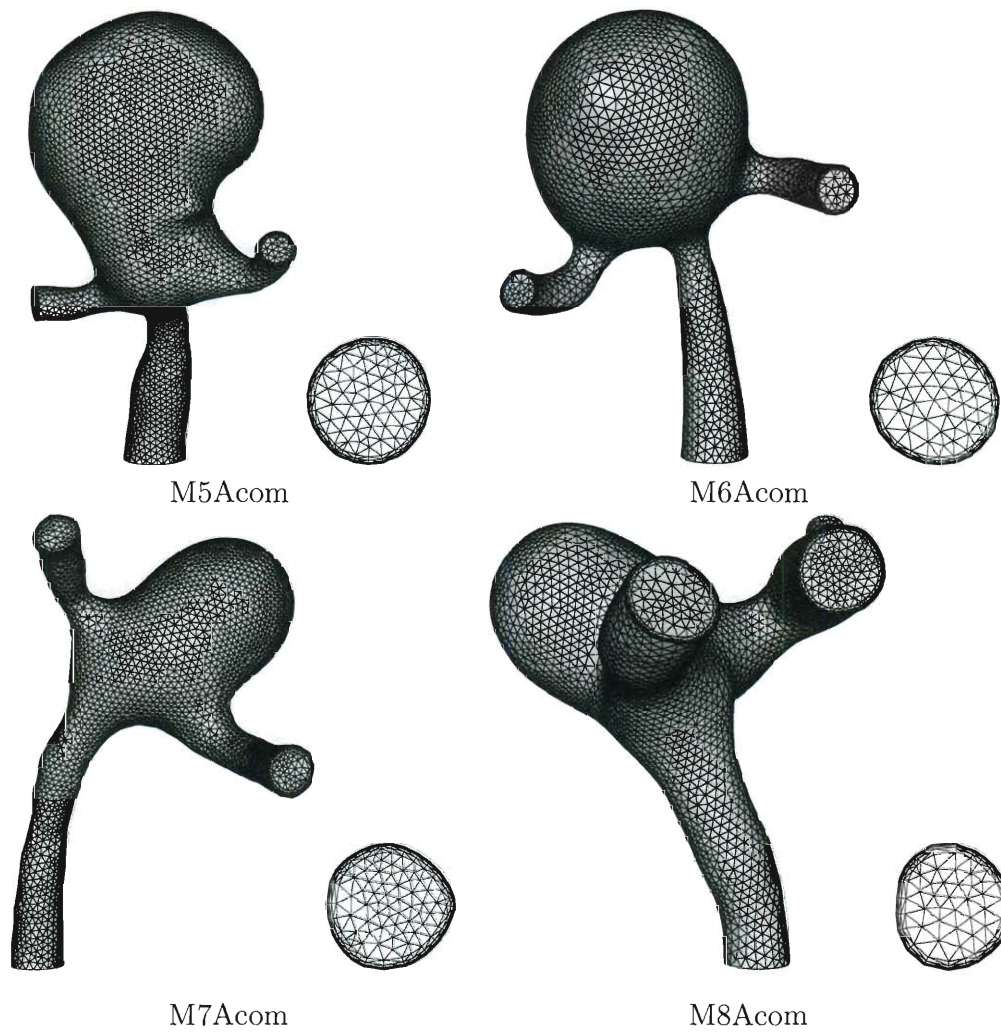


Figure 6.6: Fluid mechanics meshes at starting pressure at the fluid–structure interface and inflow plane for the Acom models.

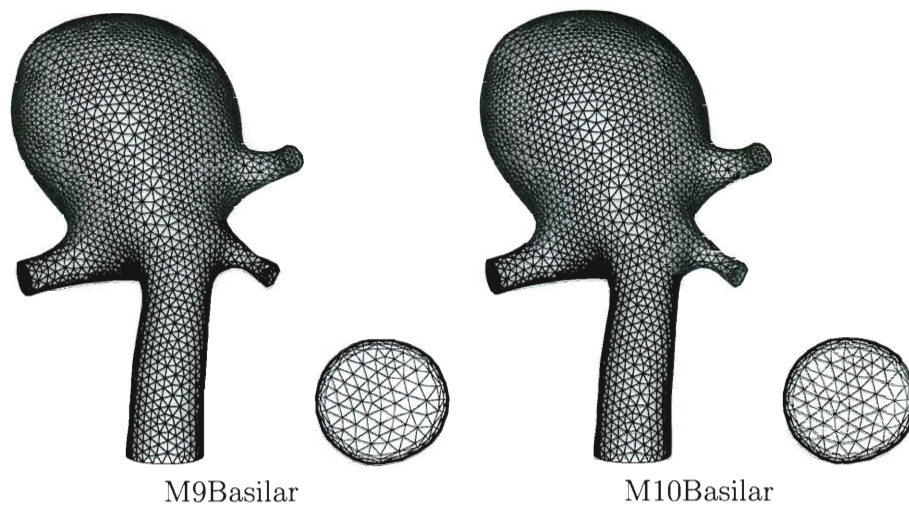


Figure 6.7: Fluid mechanics meshes at starting pressure at the fluid–structure interface and inflow plane for the Basilar models.

	Fluid			
	Volume		Interface	
	$nn$	$ne$	$nn$	$ne$
M1MCA	52,136	302,336	5,698	11,315
M2MCA	54,284	316,980	5,574	11,064
M3MCA	37,610	215,844	4,485	8,898
M4MCA	60,217	353,953	5,807	11,554
M5Acom	56,214	331,983	5,143	10,222
M6Acom	33,040	192,112	3,528	6,996
M7Acom	41,858	243,098	4,567	9,066
M8Acom	38,583	223,064	4,245	8,394
M9Basilar	41,838	246,098	3,953	7,845
M10Basilar	40,801	237,797	4,155	8,220

Table 6.3: Number of nodes and elements for the fluid mechanics mesh of each of the ten arterial models. Here  $nn$  and  $ne$  are number of nodes and elements, respectively.

Model	GMRES Iterations	Incompressibility Scale
M1MCA	350	1.0
M2MCA	450	1.0
M3MCA	300	1.0
M4MCA	800	10
M5Acom	400	1.0
M6Acom	300	1.0
M7Acom	500	1.0
M8Acom	400	1.0
M9Basilar	450	10
M10Basilar	500	10

Table 6.4: Computational parameters for the ten arterial models. Structure scales and fluid scales for the momentum conservation are 100 and 1.0 respectively for all models.

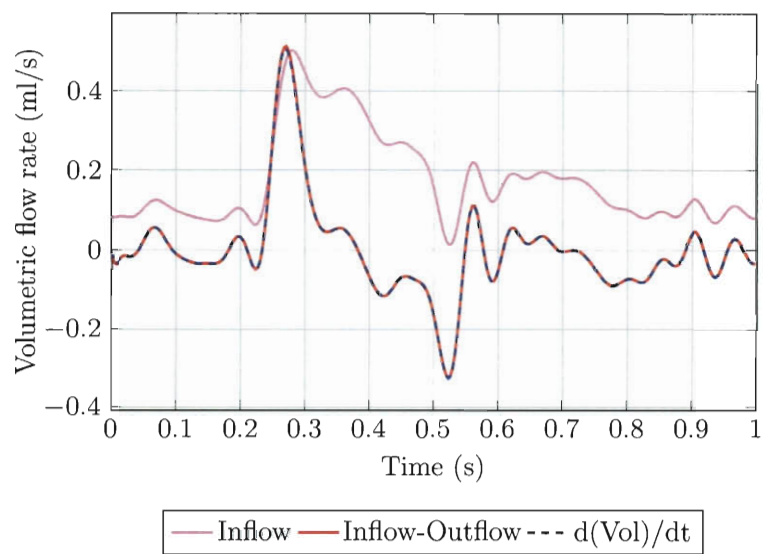


Figure 6.8: Mass balance for M1MCA.

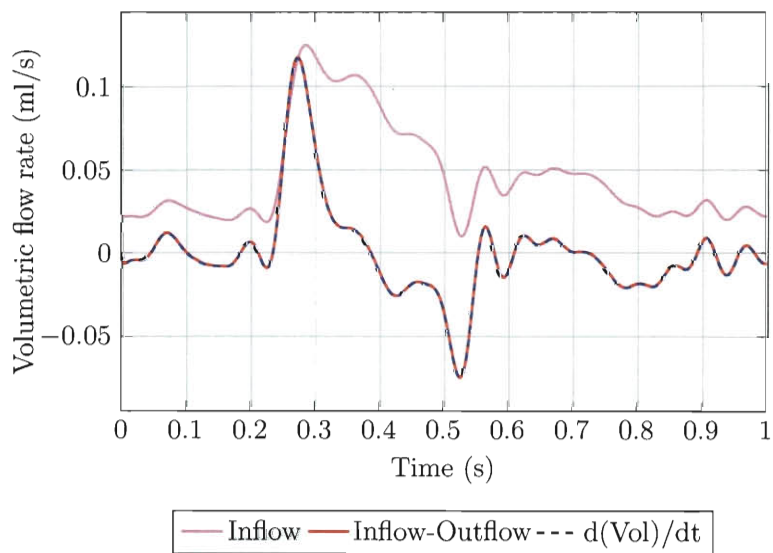


Figure 6.9: Mass balance for M2MCA.



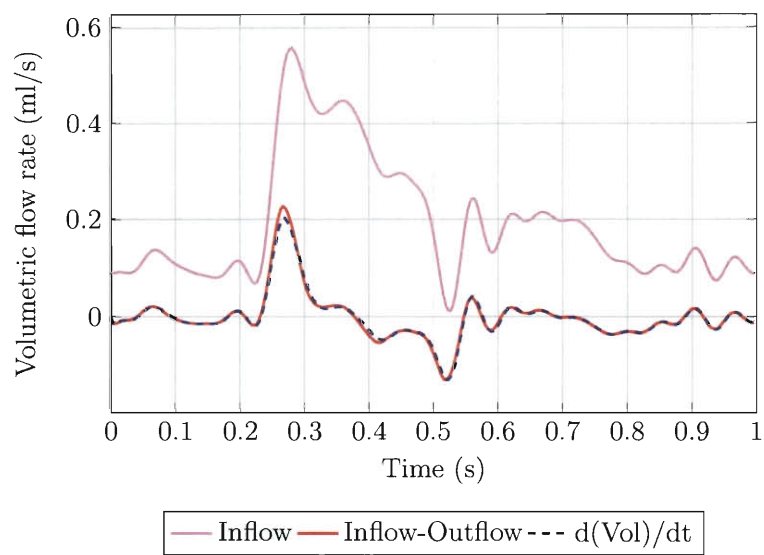


Figure 6.10: Mass balance for M3MCA.

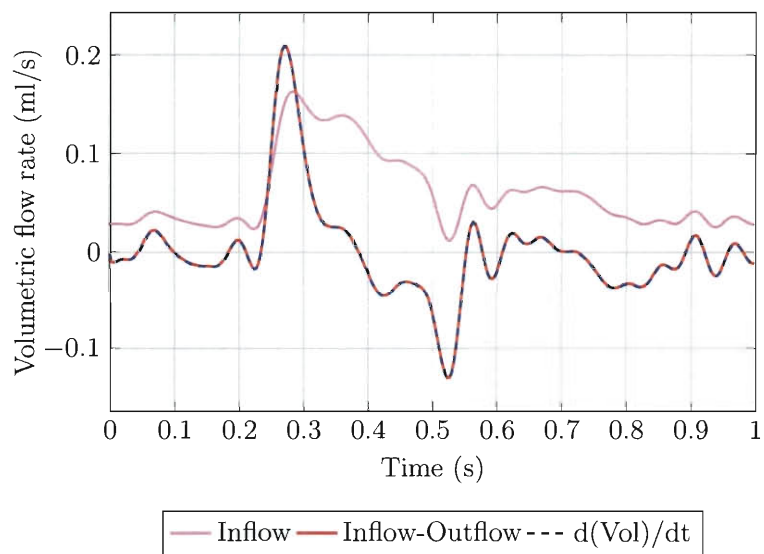


Figure 6.11: Mass balance for M4MCA.

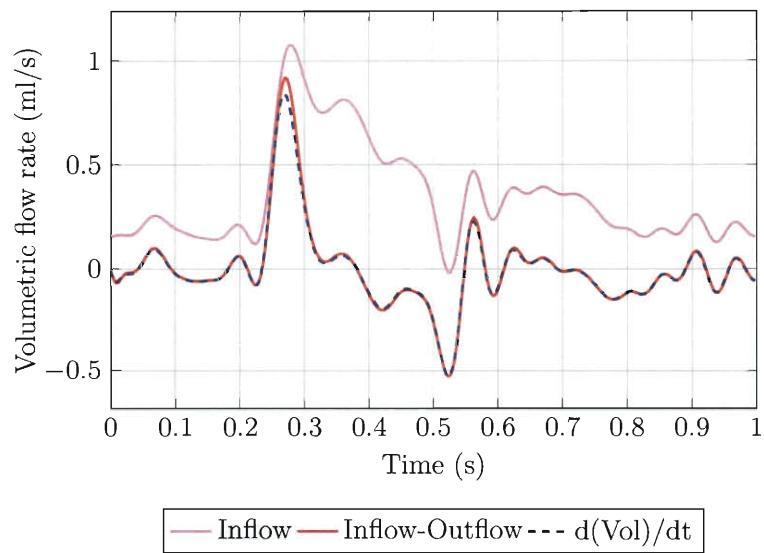


Figure 6.12: Mass balance for M5Acom.

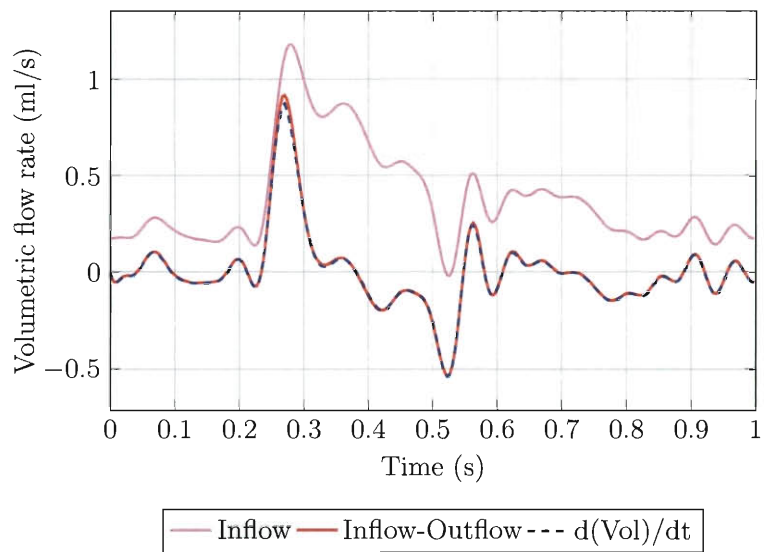


Figure 6.13: Mass balance for M6Acom.

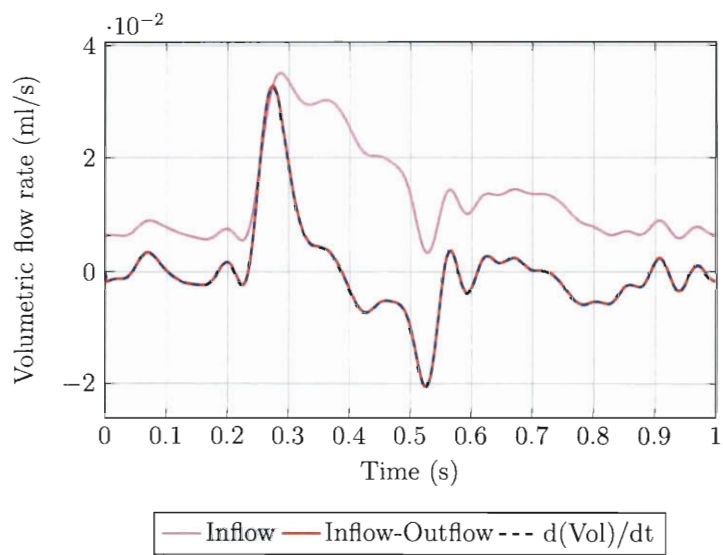


Figure 6.14: Mass balance for M7Acom.

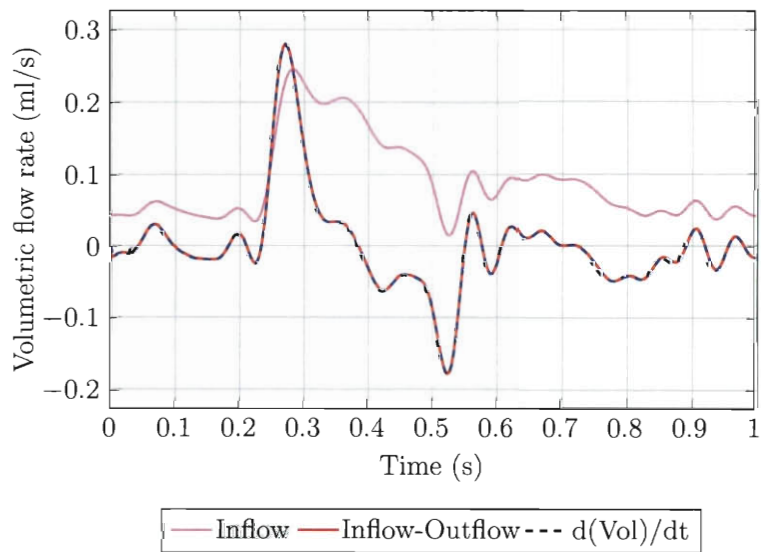


Figure 6.15: Mass balance for M8Acom.

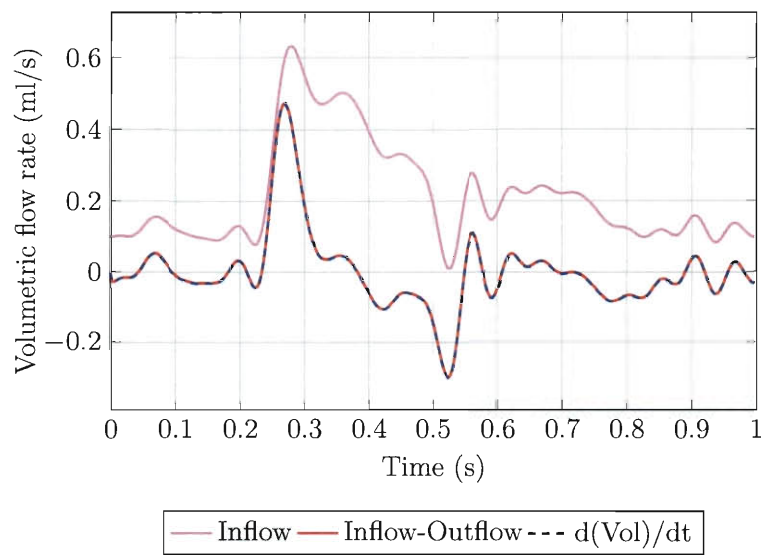


Figure 6.16: Mass balance for M9Basilar.

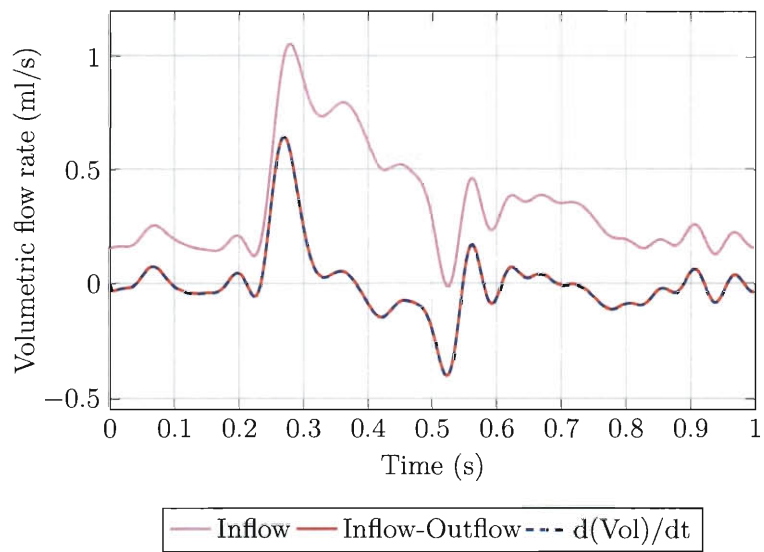


Figure 6.17: Mass balance for M10Basilar.

## 6.2 Comparative Study

### 6.2.1 Blood Flow Characteristics

We compare the fluid mechanics results by analyzing WSS and OSI. For the ten arterial models, the maximum WSS occurred at the maximum inflow flow rate of the cardiac cycle, peak of Figure 5.5. A comparison of the maximum WSS is shown in Figure 6.18, and Figure 6.19 shows the average WSS over space and time. Figures 6.20–6.29 show the WSS at peak flow for all the models. Four of the non-Basilar models, M1MCA, M3MCA, M5Acom, and M6Acom have significant WSS on the dome of the aneurysm, which occur 0.03–0.06 s after the peak flow. Figures 6.30–6.33 show the WSS on the dome of the aneurysm and the streamlines representing the flow field that cause the WSS for each of the four models. For these, the maximum volumetric flow rate is higher than the other models, meaning the difference is not due to the fact that 3 of the 4 are unruptured but rather due to the inflow scaling method we used as described in Section 5.4, which depends on inflow diameter. Figures 6.34–6.43 show the OSI for all the models. From what we observe in blood flow characteristics, we do not find conclusive evidence for a categorical difference between unruptured and ruptured aneurysms.

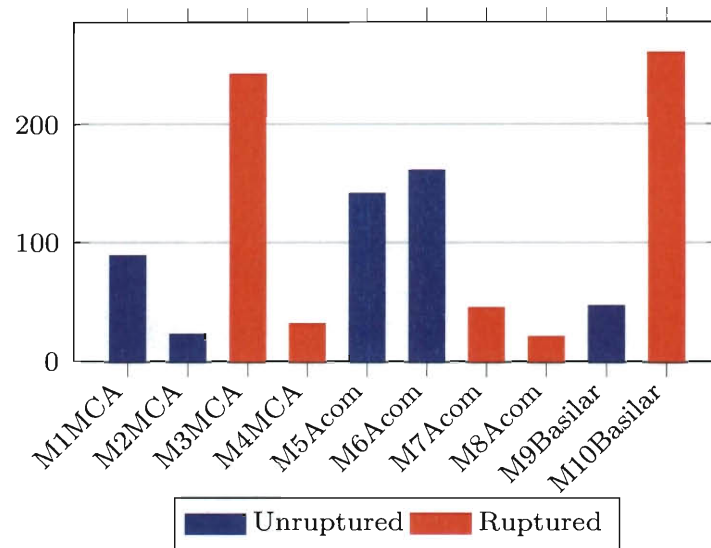


Figure 6.18: Maximum WSS (dyn/cm<sup>2</sup>) in space and time.

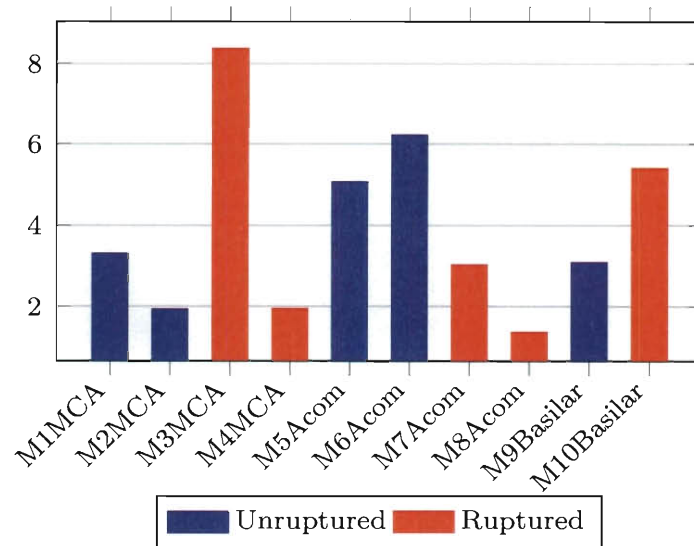


Figure 6.19: Average WSS (dyn/cm<sup>2</sup>) in space and time.

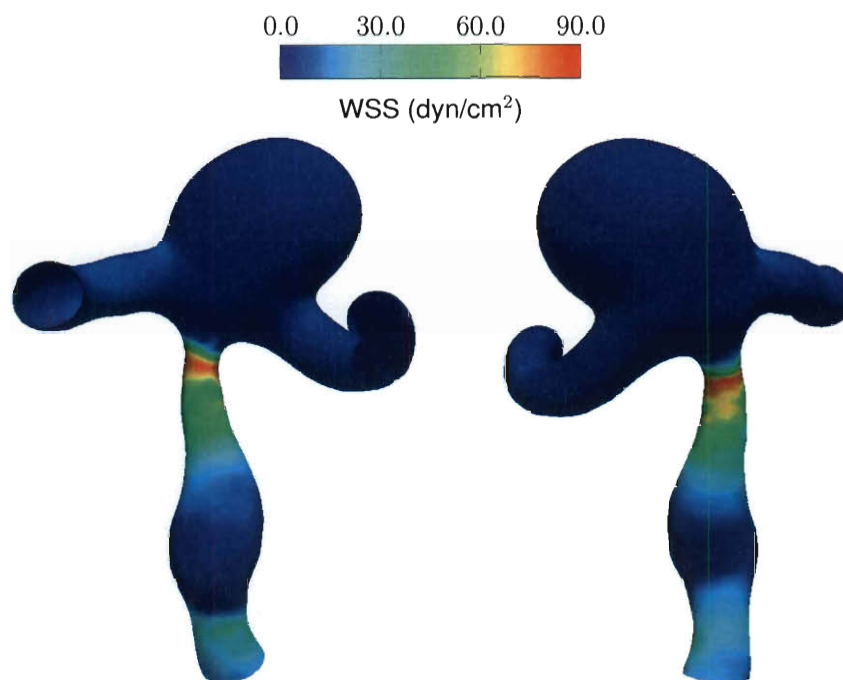


Figure 6.20: WSS at peak flow for M1MCA.

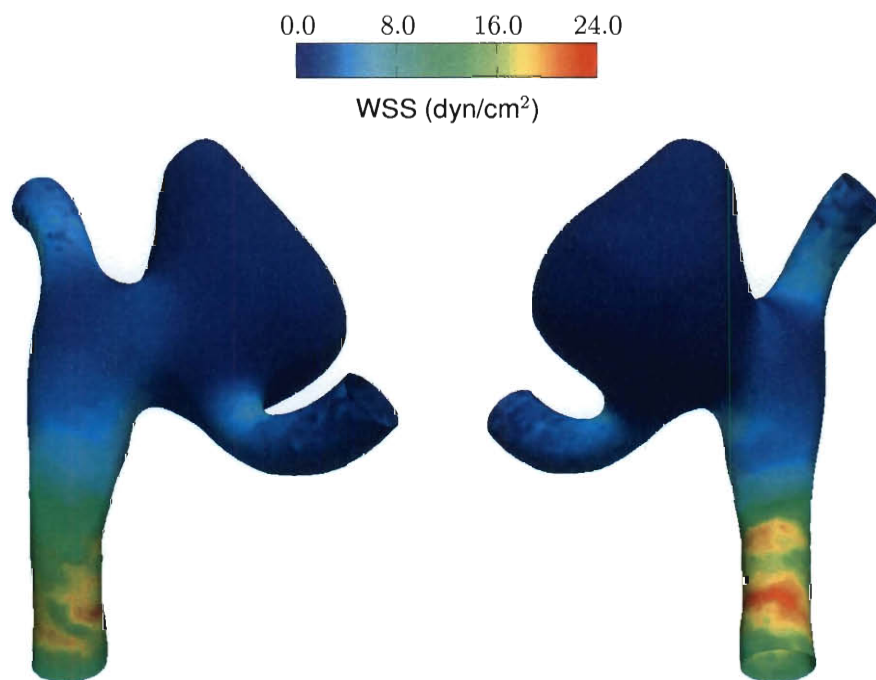


Figure 6.21: WSS at peak flow for M2MCA.

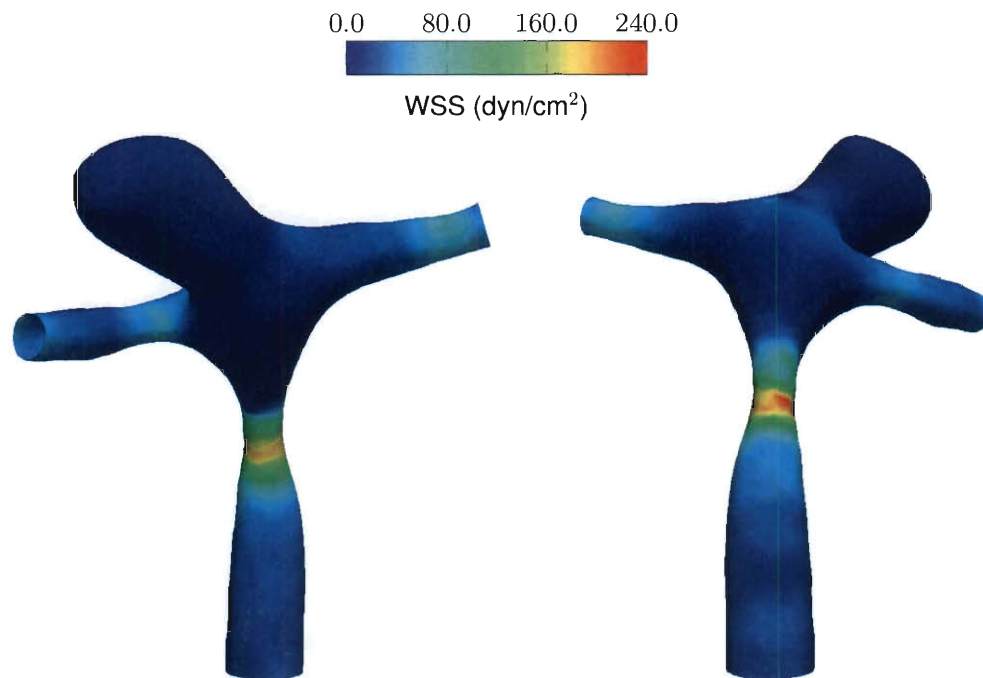


Figure 6.22: WSS at peak flow for M3MCA.

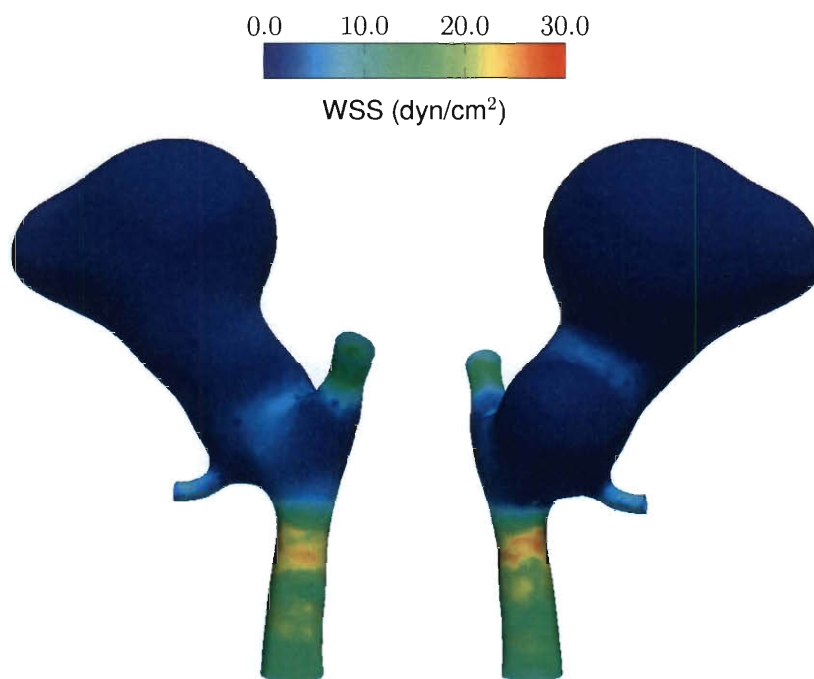


Figure 6.23: WSS at peak flow for M4MCA.



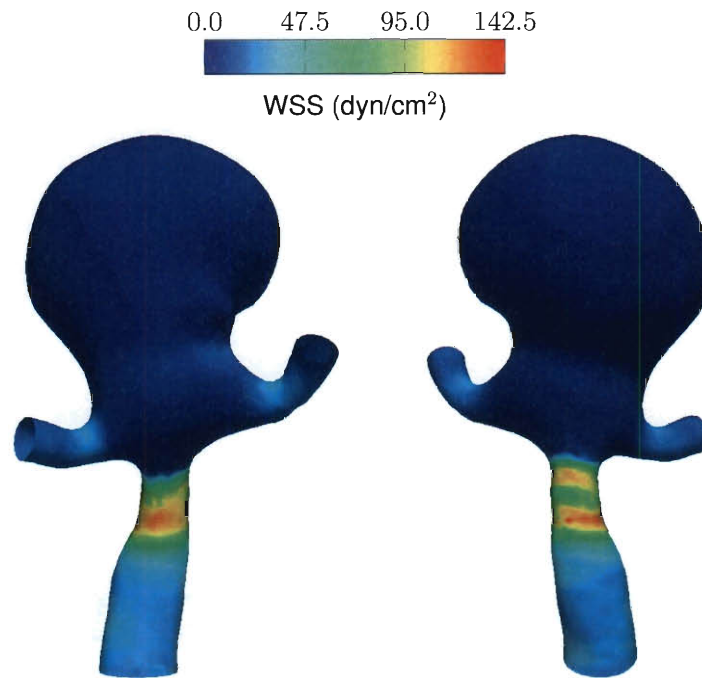


Figure 6.24: WSS at peak flow for M5Acom.

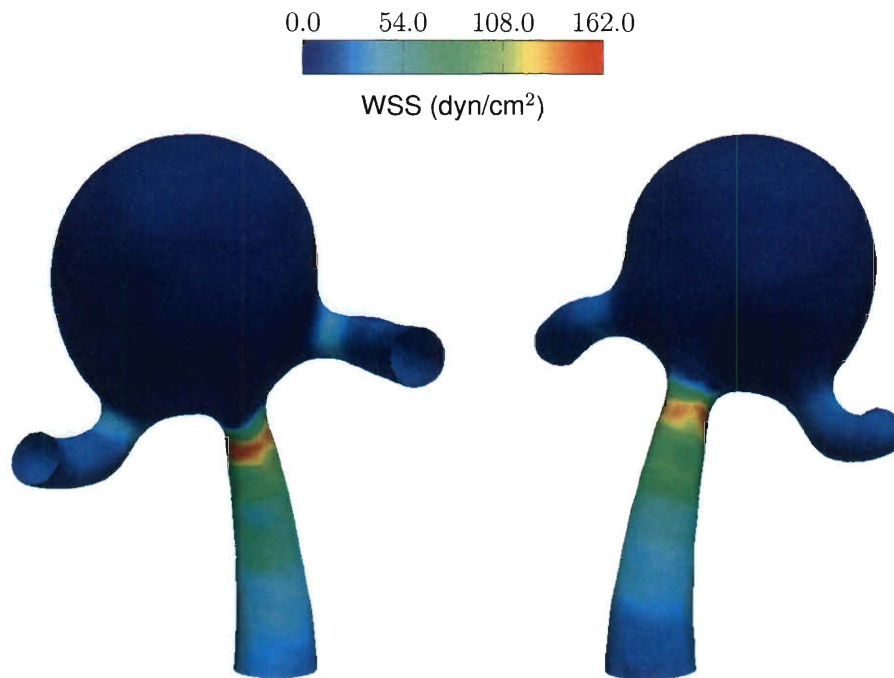


Figure 6.25: WSS at peak flow for M6Acom.

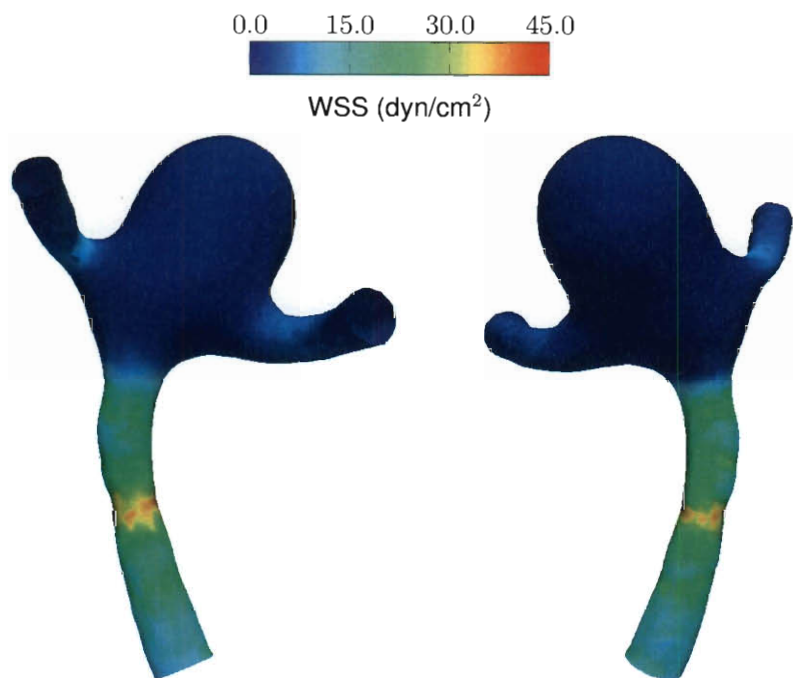


Figure 6.26: WSS at peak flow for M7Acom.

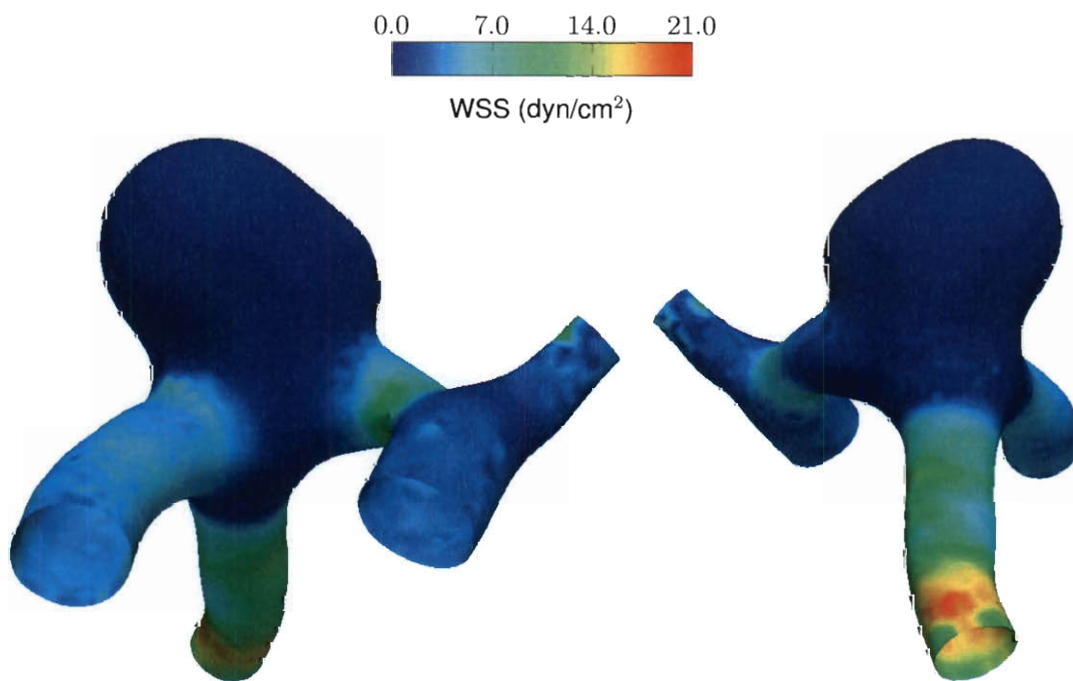


Figure 6.27: WSS at peak flow for M8Acom.

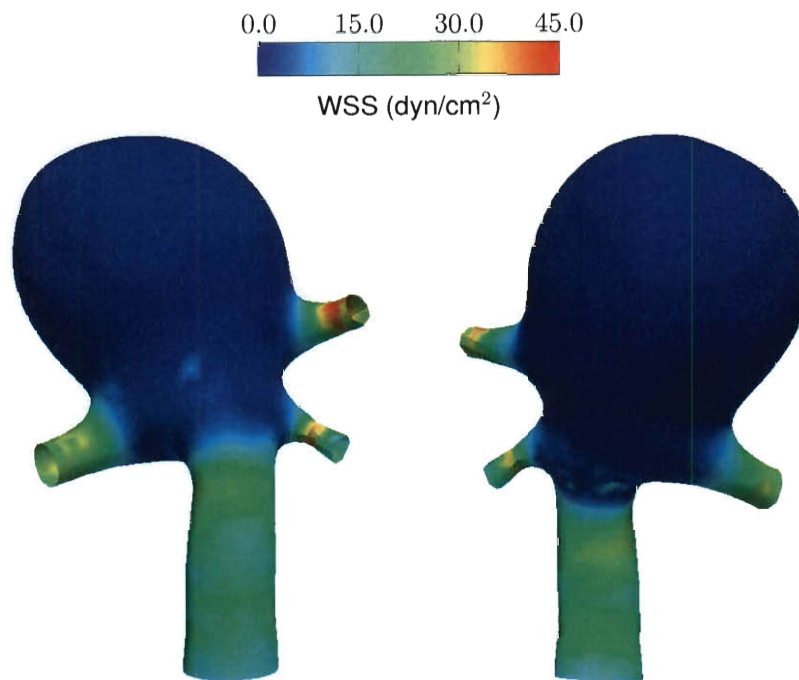


Figure 6.28: WSS at peak flow for M9Basilar.

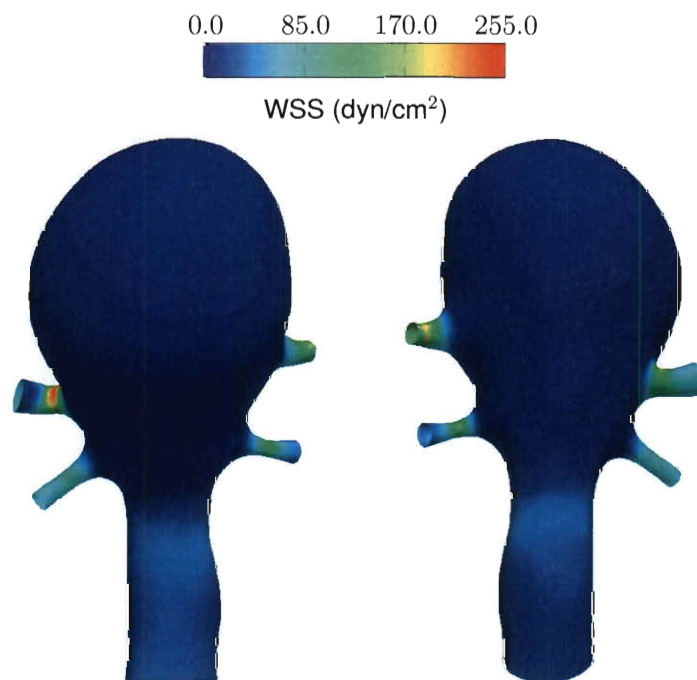


Figure 6.29: WSS at peak flow for M10Basilar.

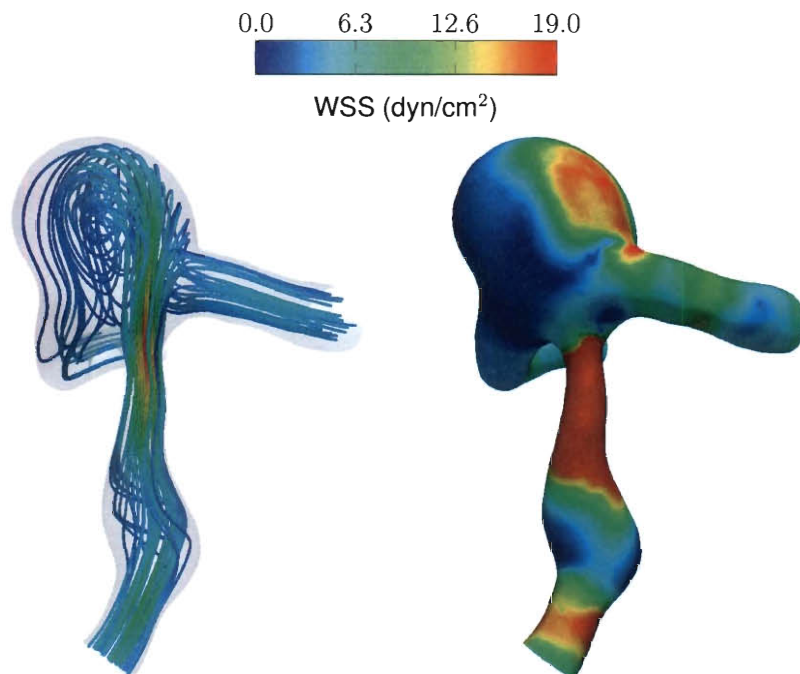


Figure 6.30: Streamlines showing WSS on the dome of the aneurysm for M1MCA at 0.06 s after the peak flow. The maximum WSS on the dome is 19.0  $\text{dyn/cm}^2$ .

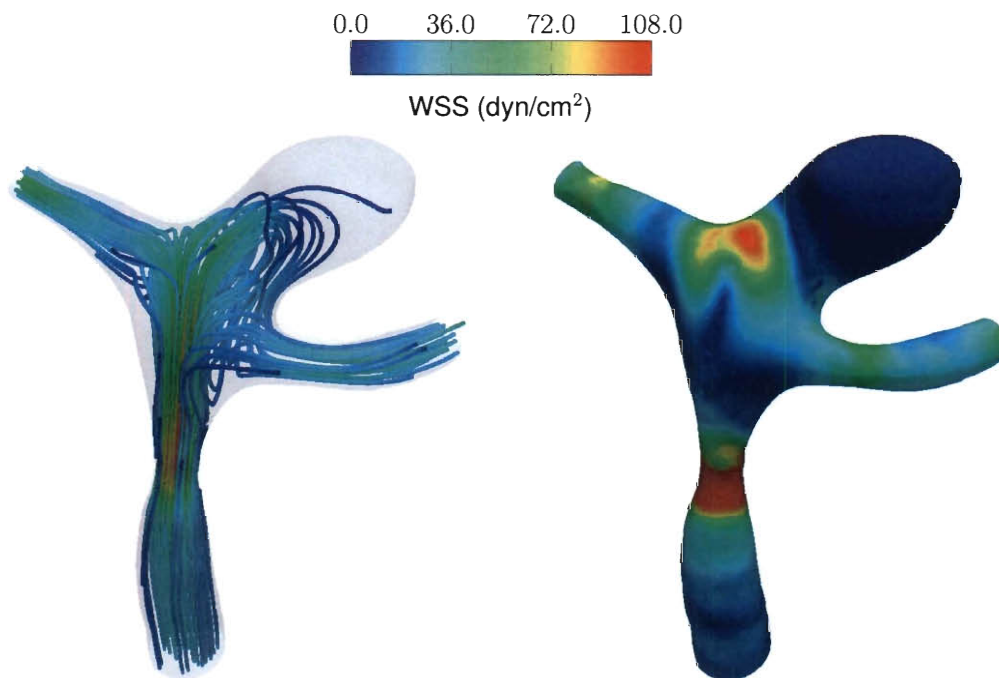


Figure 6.31: Streamlines showing WSS on the dome of the aneurysm for M3MCA at 0.03 s after the peak flow. The maximum WSS on the dome is 107.3  $\text{dyn/cm}^2$ .

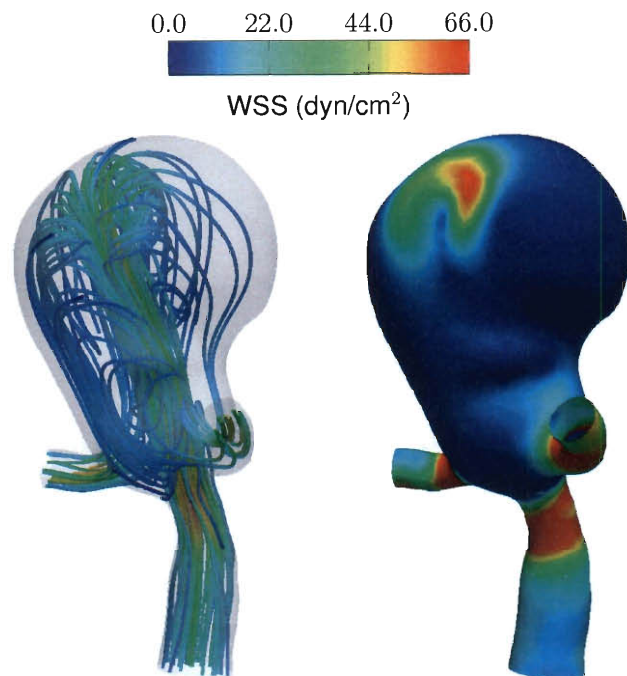


Figure 6.32: Streamlines showing WSS on the dome of the aneurysm for M5Acom at 0.06 s after the peak flow. The maximum WSS on the dome is  $65.5 \text{ dyn/cm}^2$ .

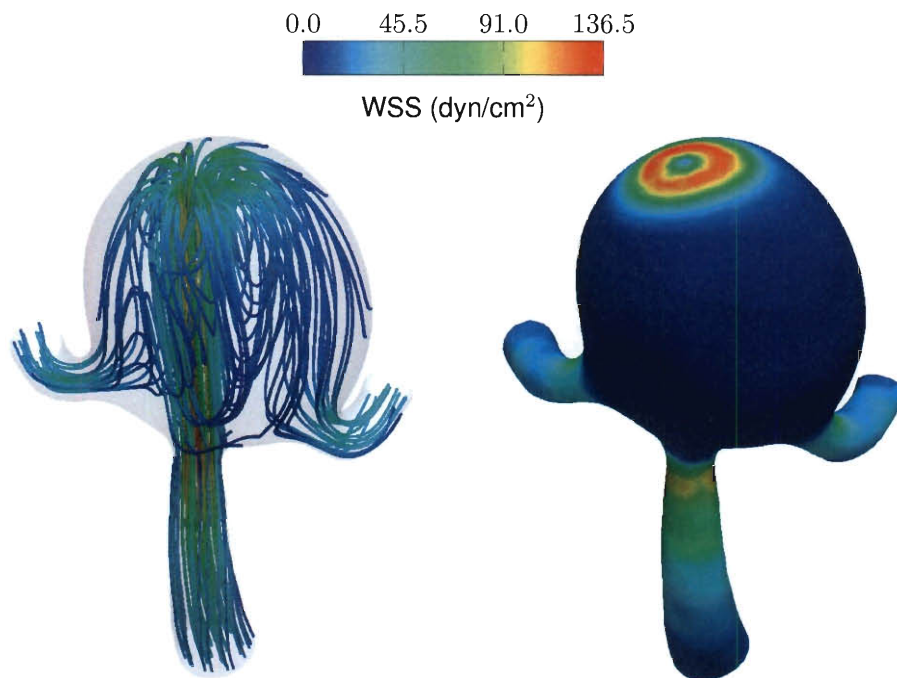


Figure 6.33: Streamlines showing WSS on the dome of the aneurysm for M6Acom at 0.03 s after the peak flow. The maximum WSS on the dome is  $136.3 \text{ dyn/cm}^2$ .

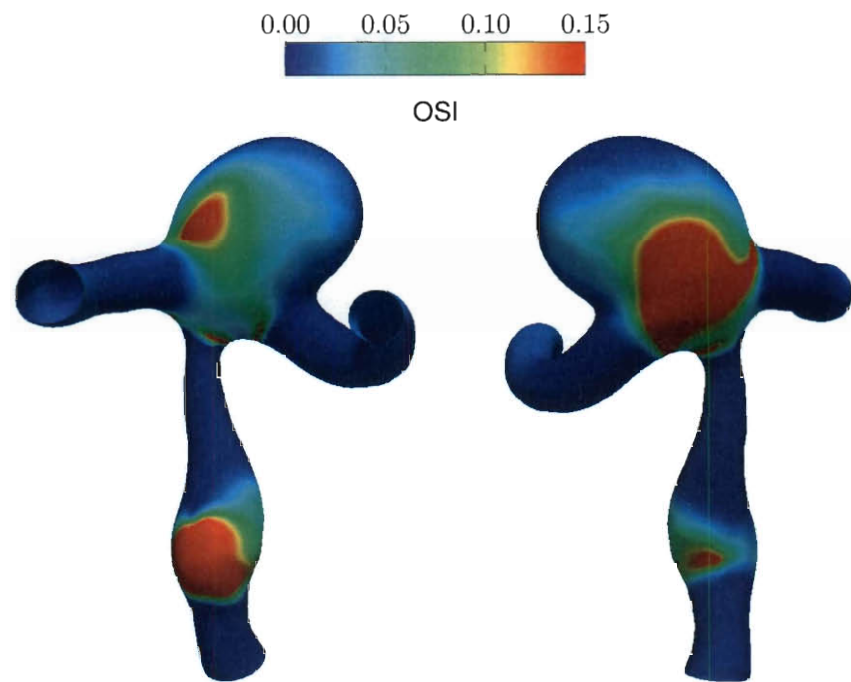


Figure 6.34: OSI for M1MCA.

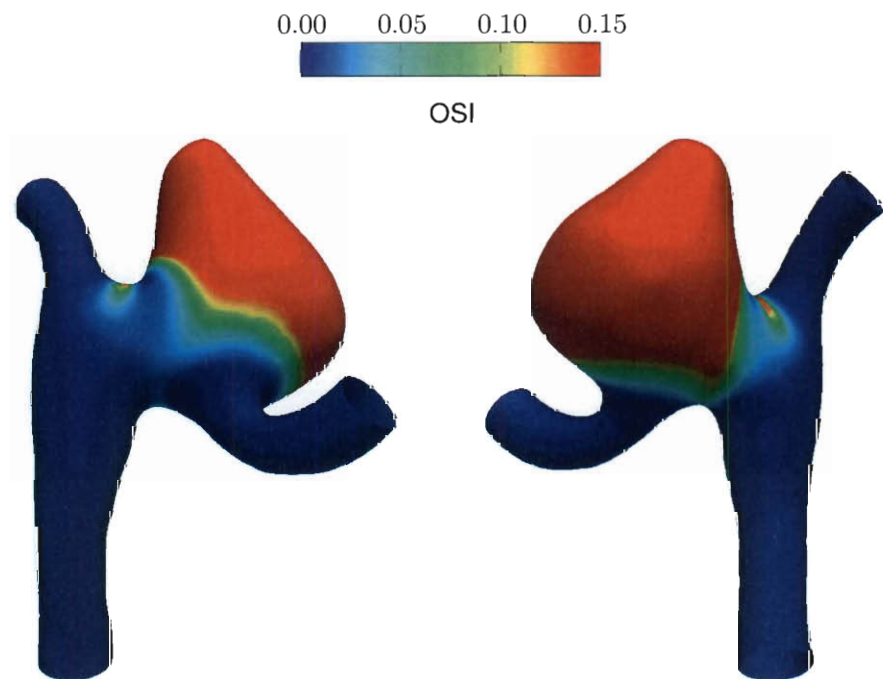


Figure 6.35: OSI for M2MCA.

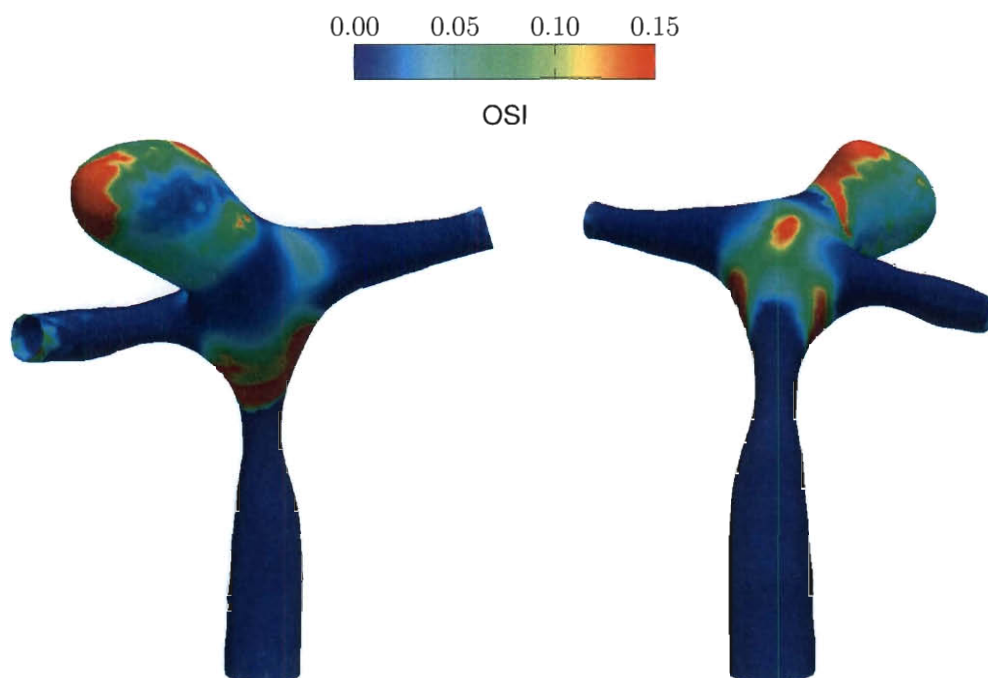


Figure 6.36: OSI for M3MCA.

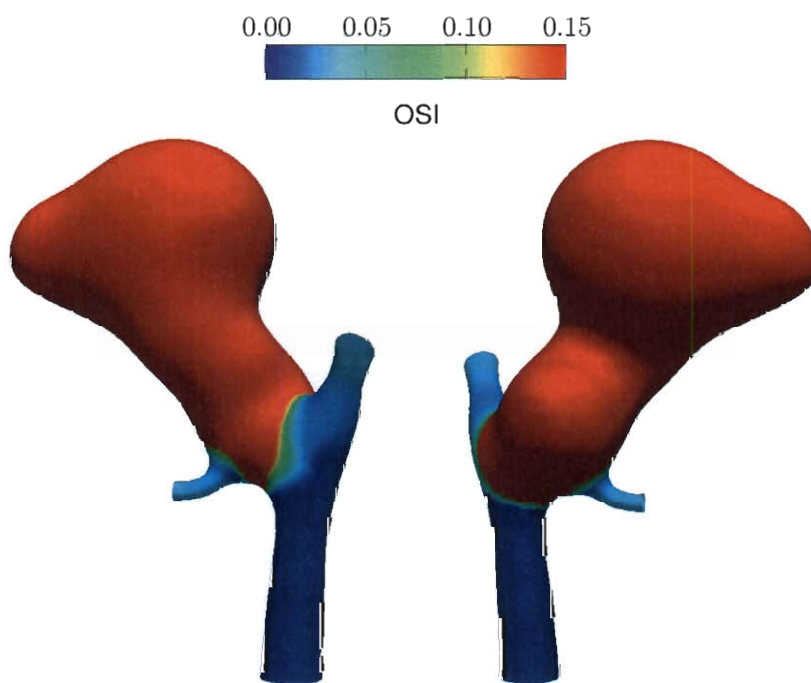


Figure 6.37: OSI for M4MCA.

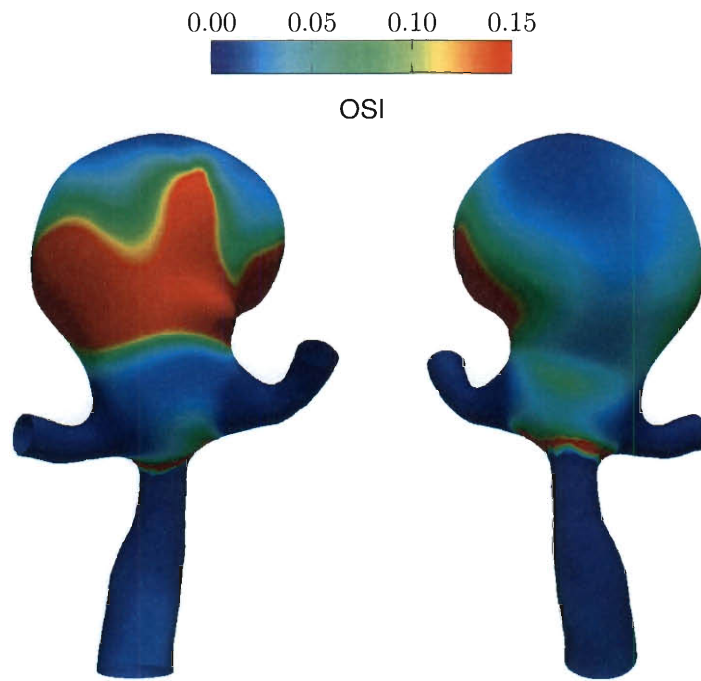


Figure 6.38: OSI for M5Acom.

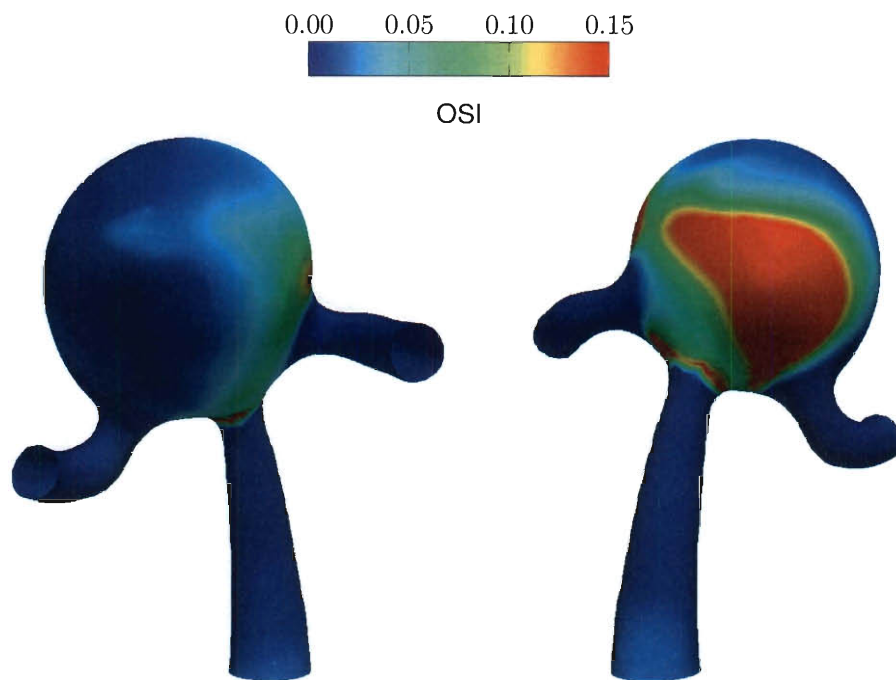


Figure 6.39: OSI for M6Acom.



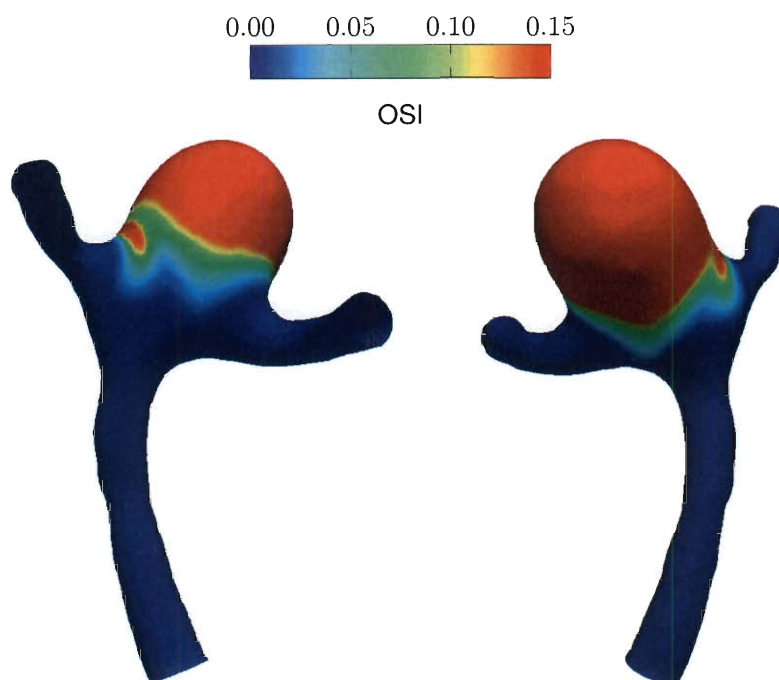


Figure 6.40: OSI for M7Acom.

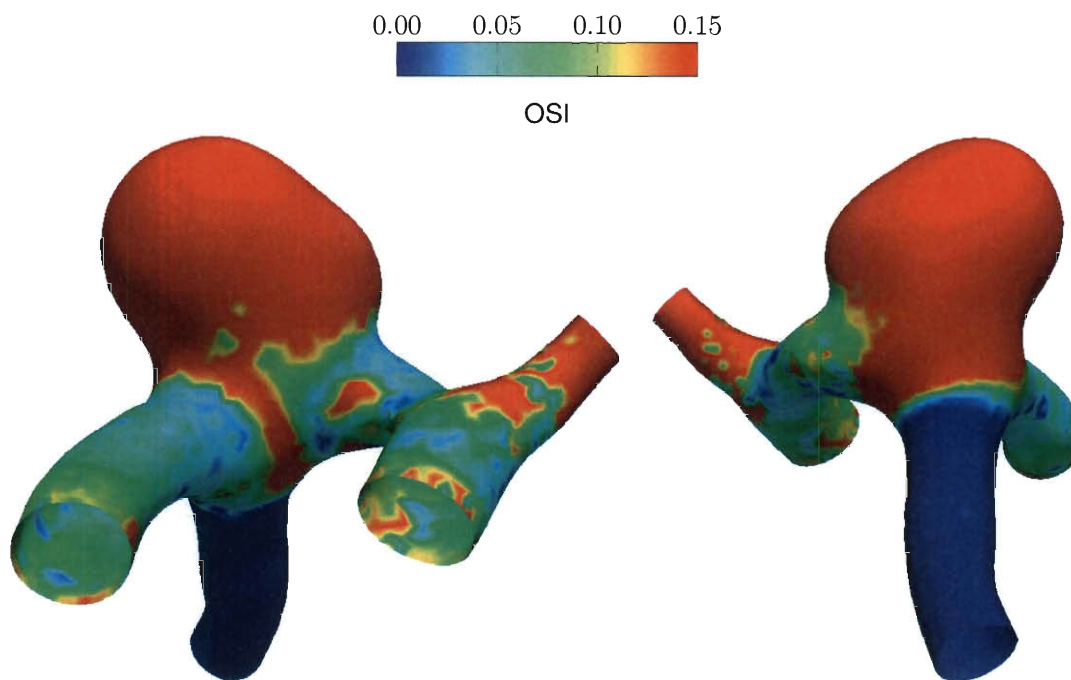


Figure 6.41: OSI for M8Acom.

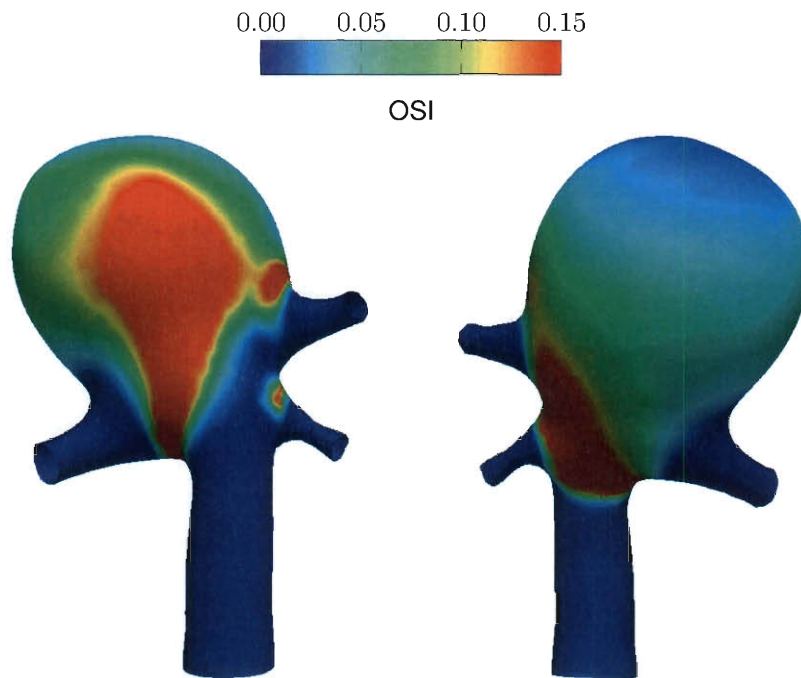


Figure 6.42: OSI for M9Basilar.

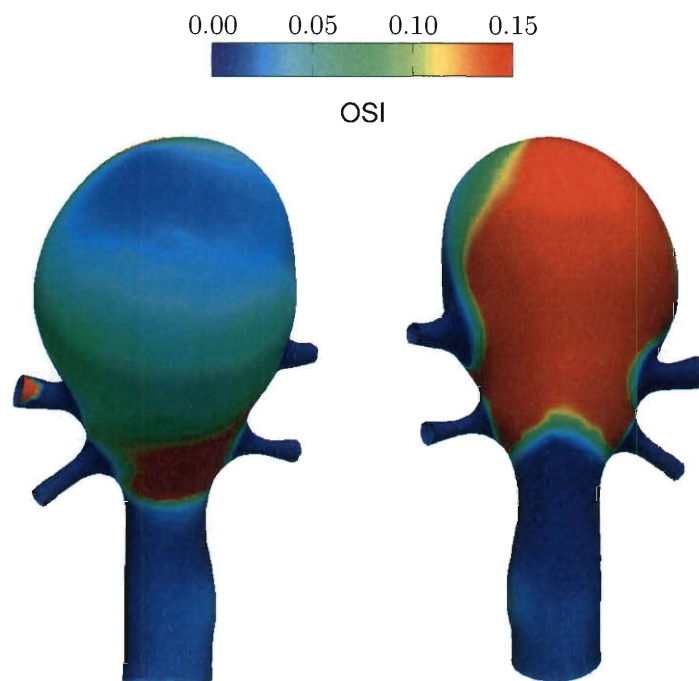


Figure 6.43: OSI for M10Basilar.

## 6.2.2 Arterial-Wall Characteristics

The structural mechanics results are compared by the arterial-wall stress and stretch. The maximum stress in space and time occurs at the peak pressure of Figure 5.6. Figure 6.44 shows the maximum stress of the arterial-wall for all the models. As a point of reference, we note from [27] that the breaking strength of saccular aneurysms is in the range of 730–1,900 kPa. Figure 6.45 displays the maximum variation in stress, which follows the same pattern as that seen in Figure 6.44. Spatially, the location of maximum variation is the same as the location of maximum stress as shown in Figures 6.46–6.55. The maximum stretch, as shown in Figure 6.56 also occurs at peak pressure. Figures 6.57–6.66 show the stretch at peak pressure for each model. The maximum stretch of the arterial-wall occurs at the same spatial locations as the arterial-wall stress. From what we observe in arterial-wall characteristics, we do not find conclusive evidence for a categoric difference between unruptured and ruptured aneurysms.

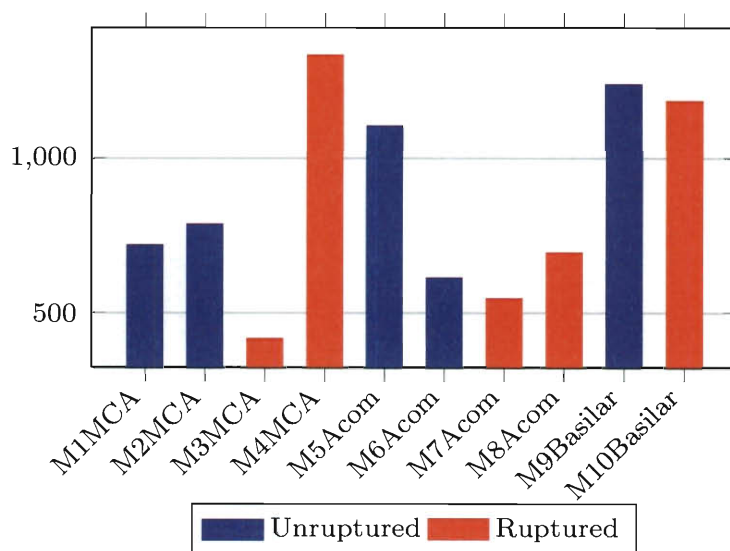


Figure 6.44: Maximum stress (kPa) in space and time.

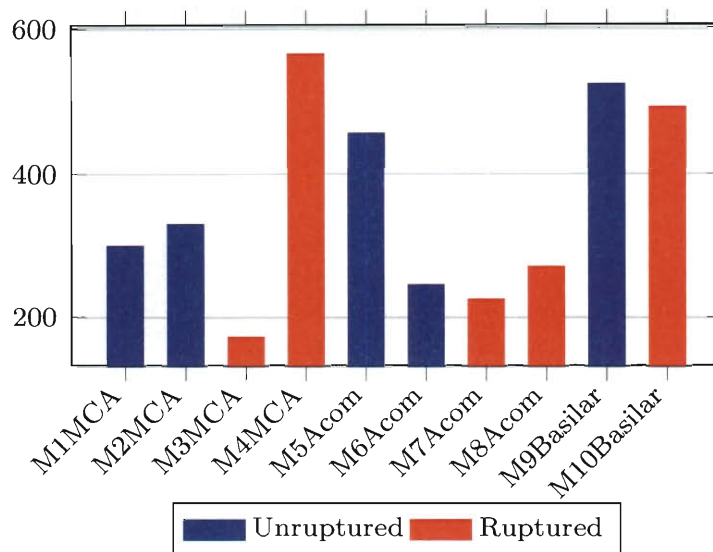


Figure 6.45: Maximum variation in stress (kPa) in space and time.

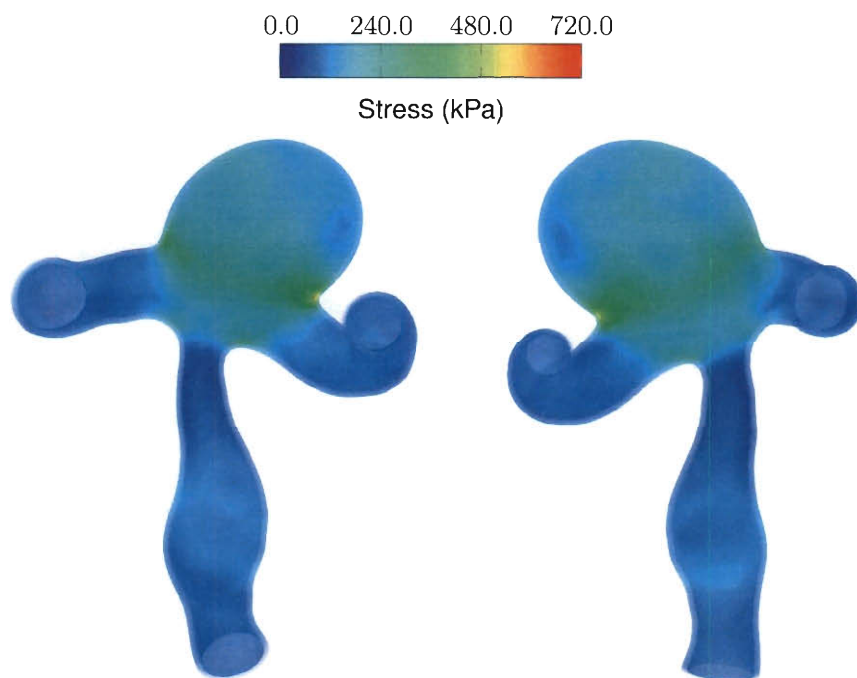


Figure 6.46: Stress at peak pressure for M1MCA.

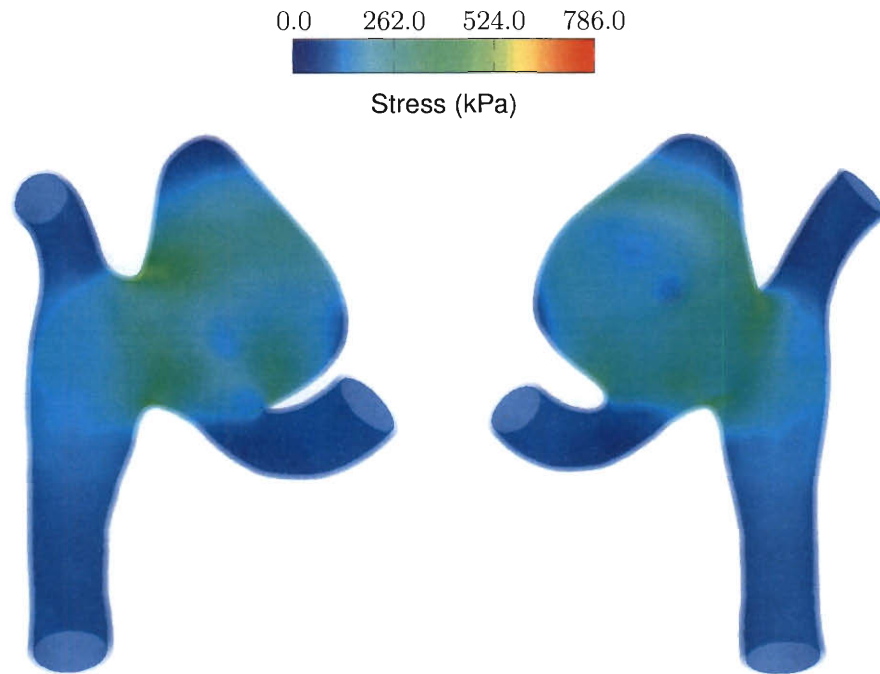


Figure 6.47: Stress at peak pressure for M2MCA.

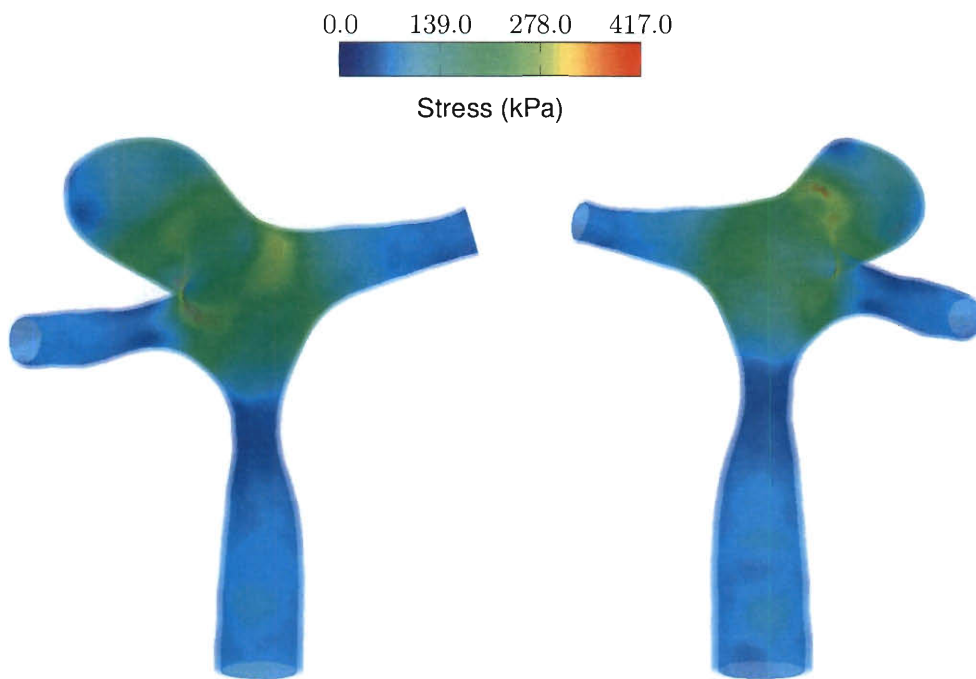


Figure 6.48: Stress at peak pressure for M3MCA.

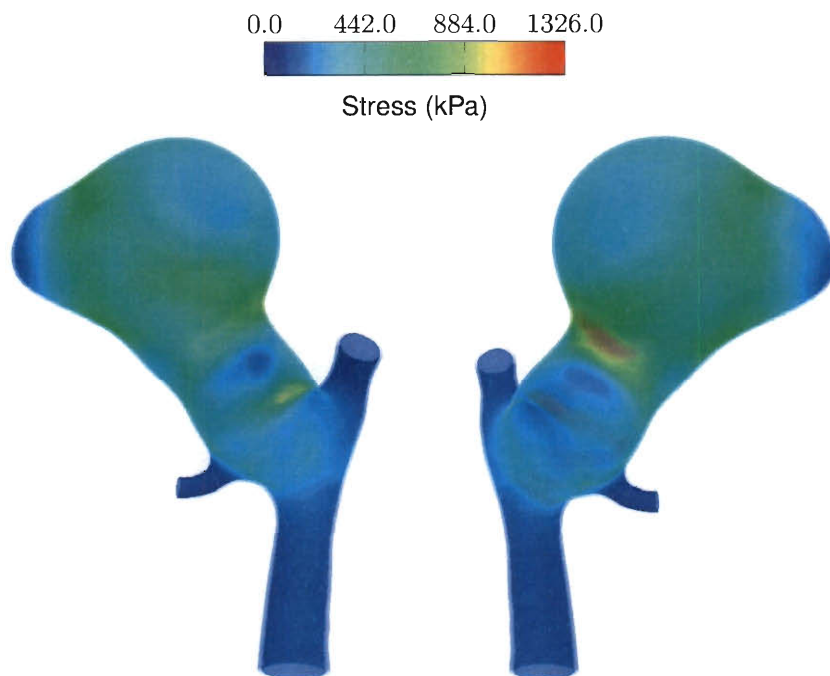


Figure 6.49: Stress at peak pressure for M4MCA.

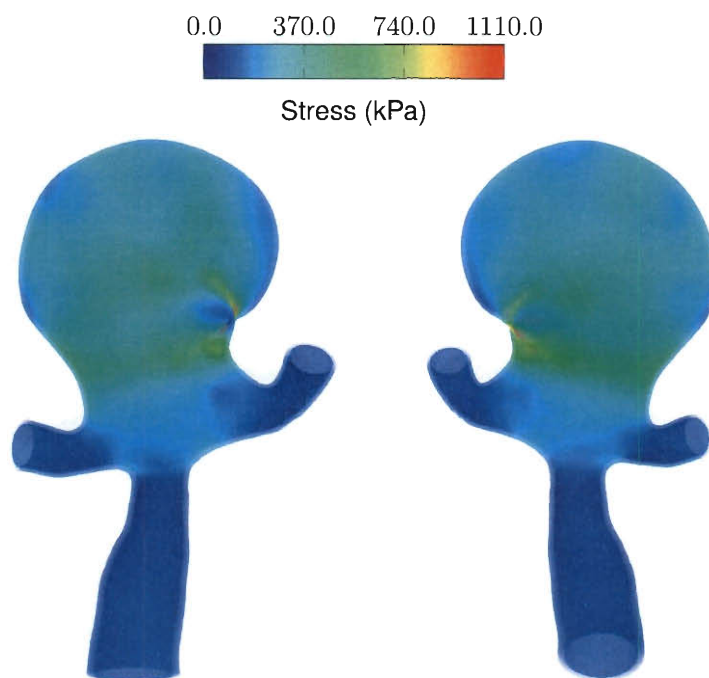


Figure 6.50: Stress at peak pressure for M5Acom.

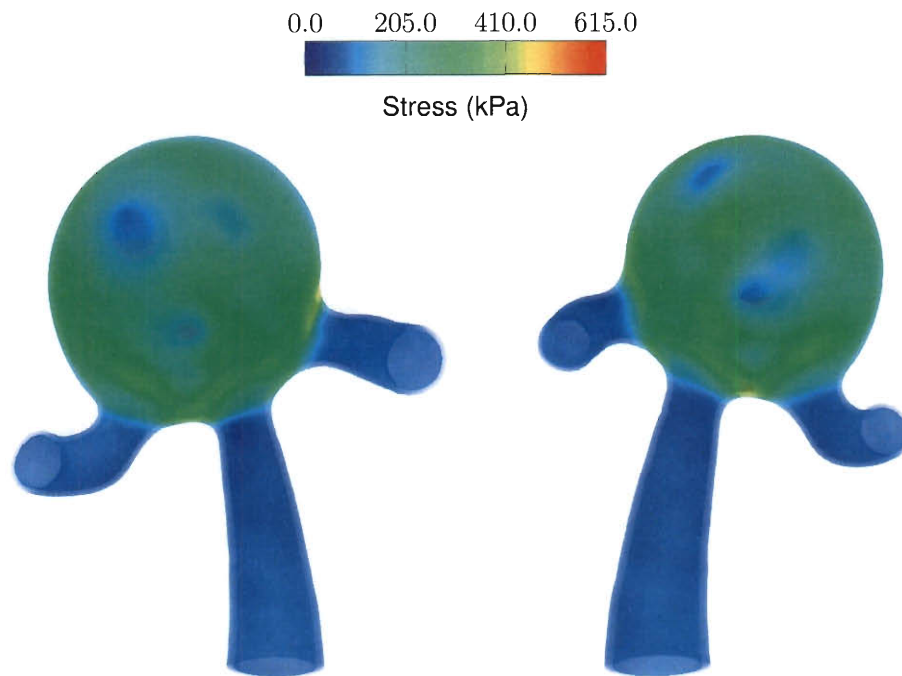


Figure 6.51: Stress at peak pressure for M6Acom.

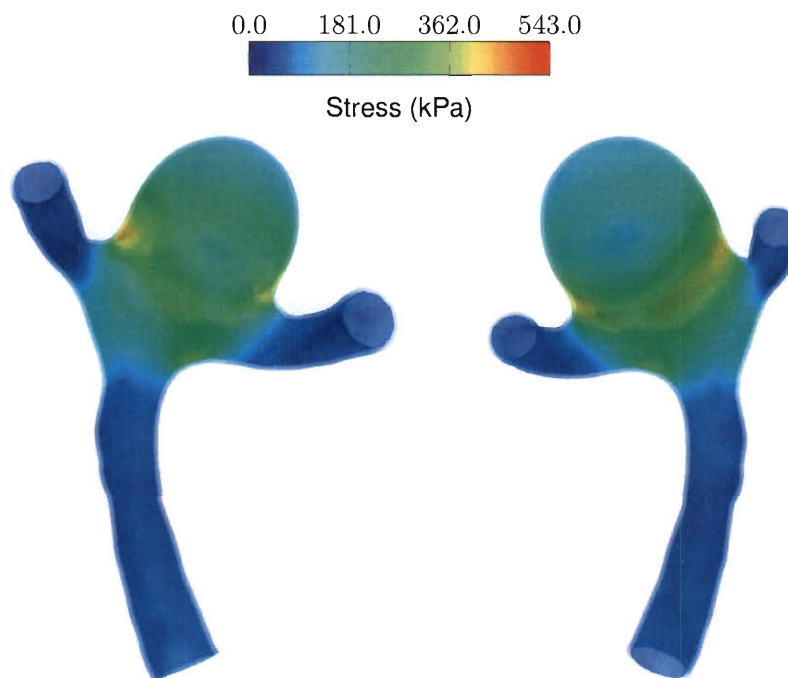


Figure 6.52: Stress at peak pressure for M7Acom.

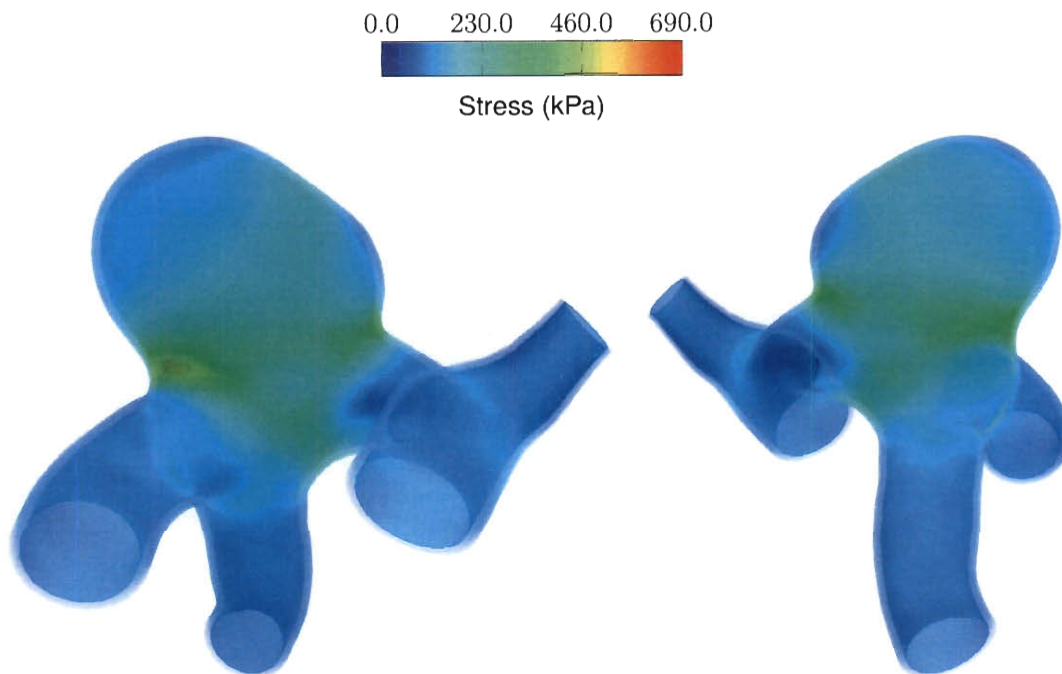


Figure 6.53: Stress at peak pressure for M8Acom.

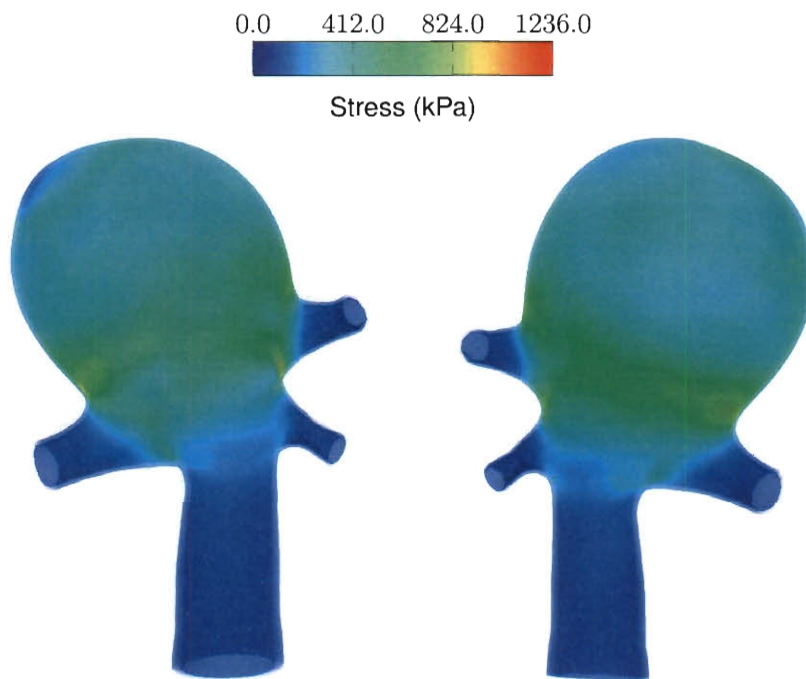


Figure 6.54: Stress at peak pressure for M9Basilar.



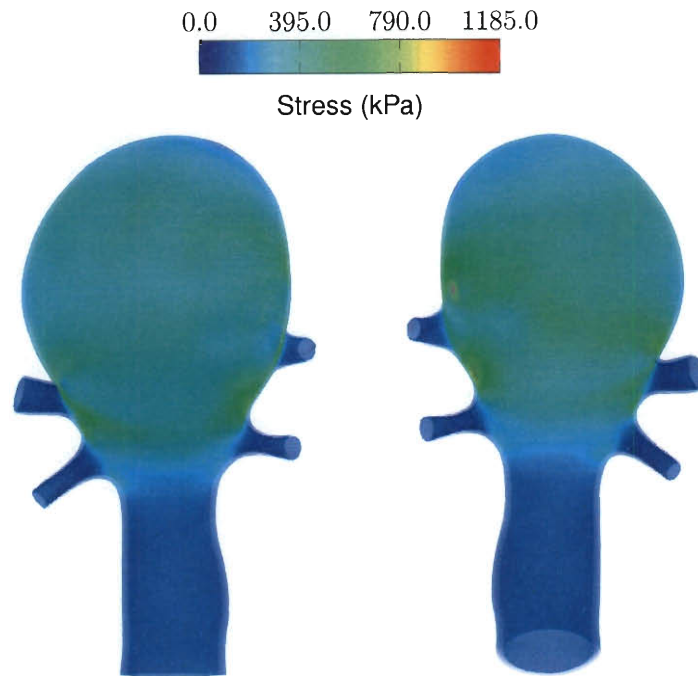


Figure 6.55: Stress at peak pressure for M10Basilar.

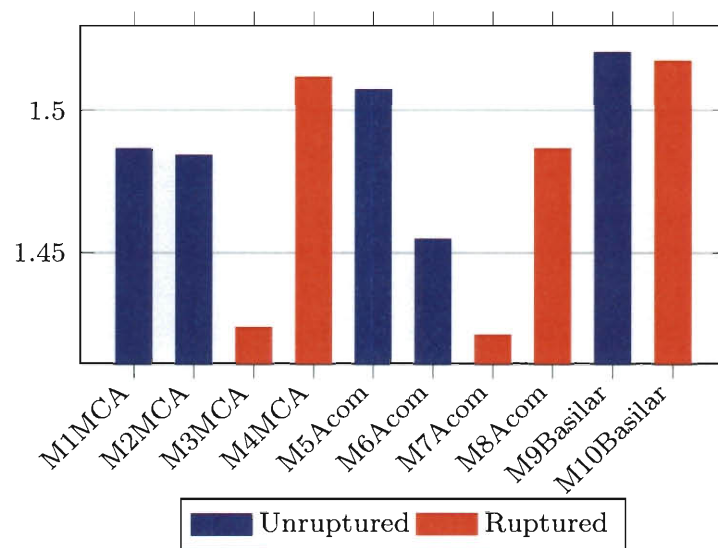


Figure 6.56: Maximum stretch in space and time.

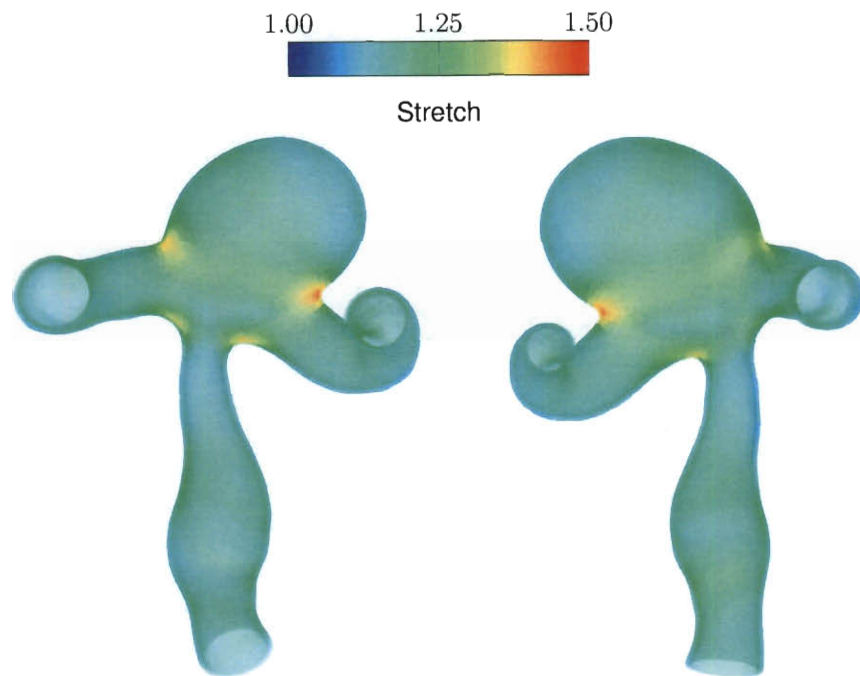


Figure 6.57: Stretch at peak pressure for M1MCA.

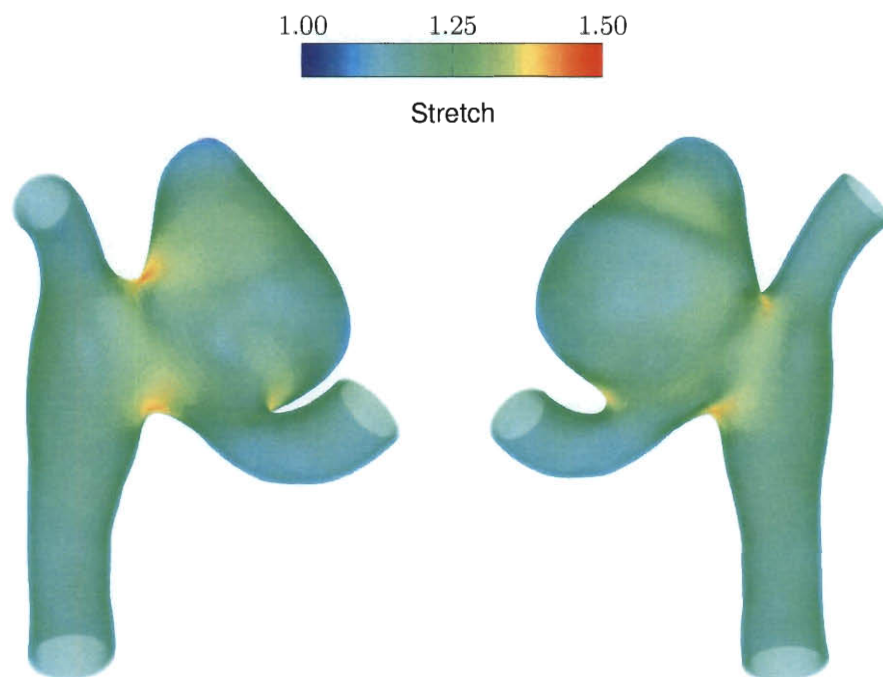


Figure 6.58: Stretch at peak pressure for M2MCA.

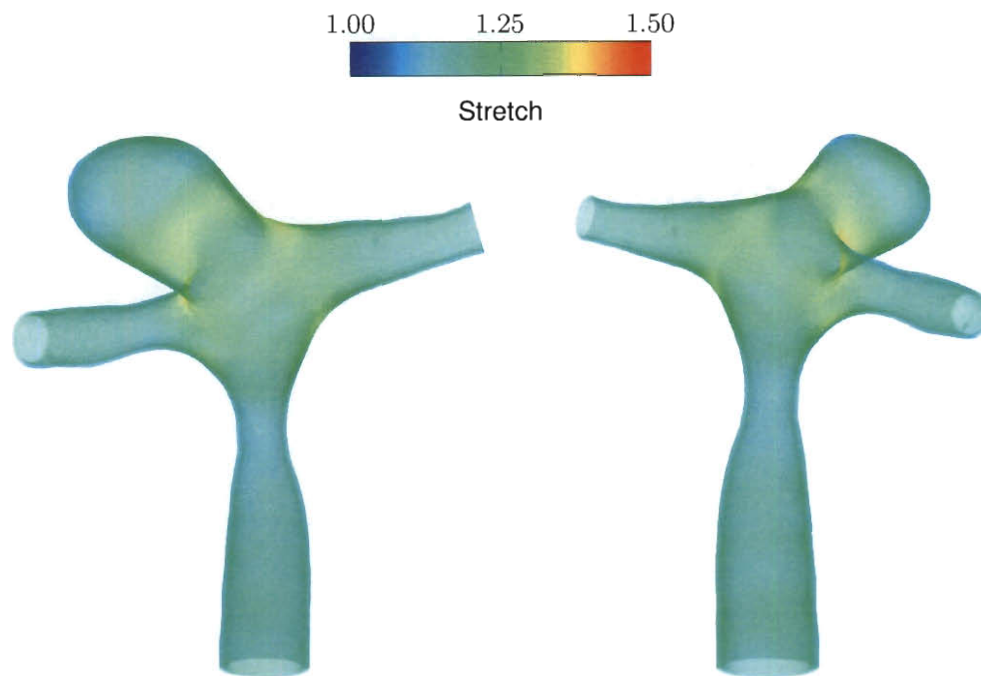


Figure 6.59: Stretch at peak pressure for M3MCA.

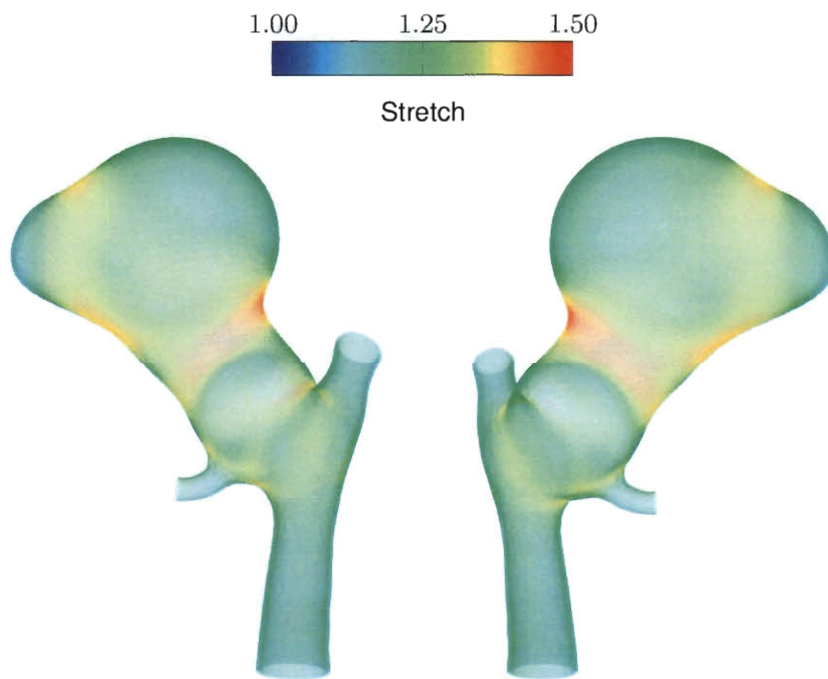


Figure 6.60: Stretch at peak pressure for M4MCA.

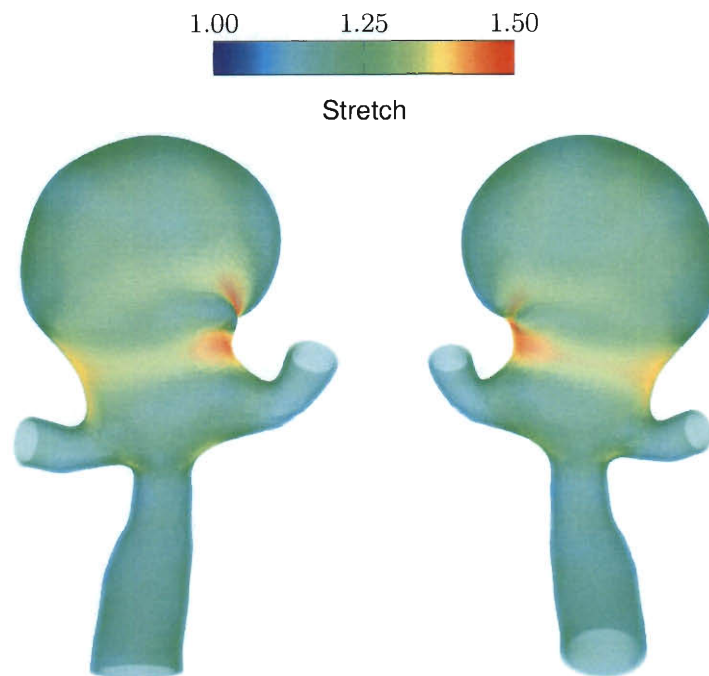


Figure 6.61: Stretch at peak pressure for M5Acom.

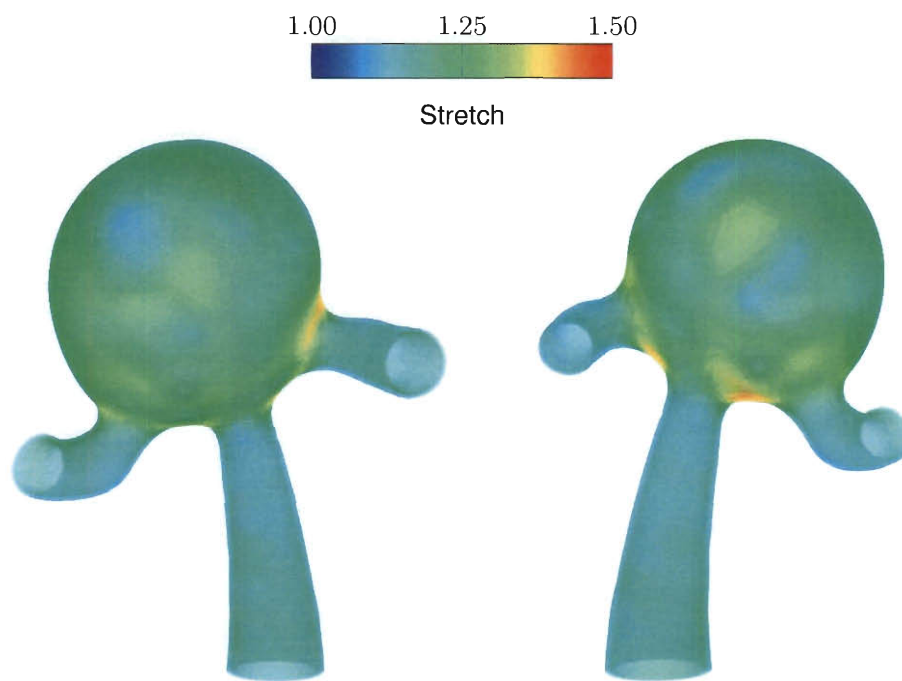


Figure 6.62: Stretch at peak pressure for M6Acom.

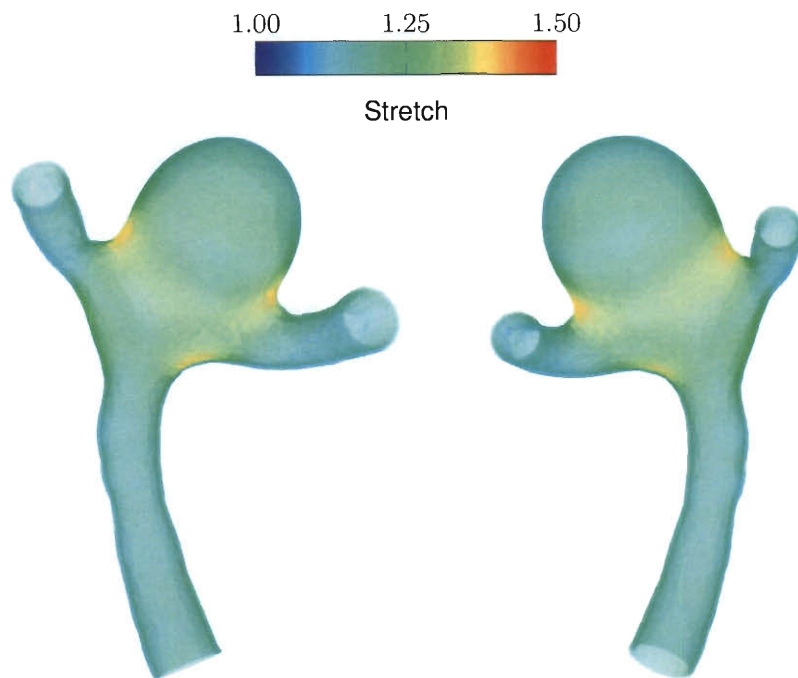


Figure 6.63: Stretch at peak pressure for M7Acom.

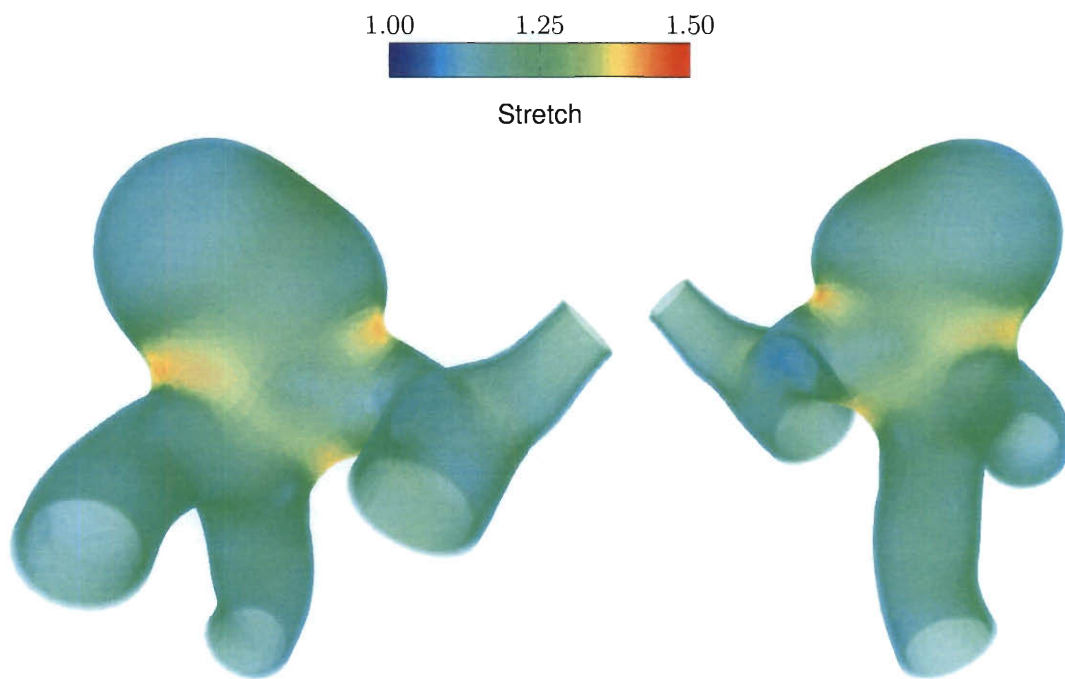


Figure 6.64: Stretch at peak pressure for M8Acom.

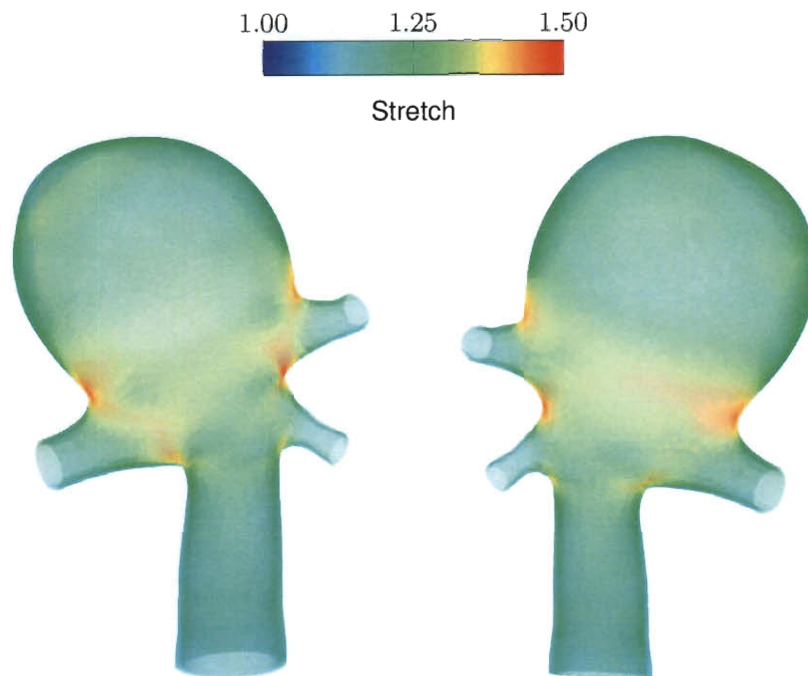


Figure 6.65: Stretch at peak pressure for M9Basilar.

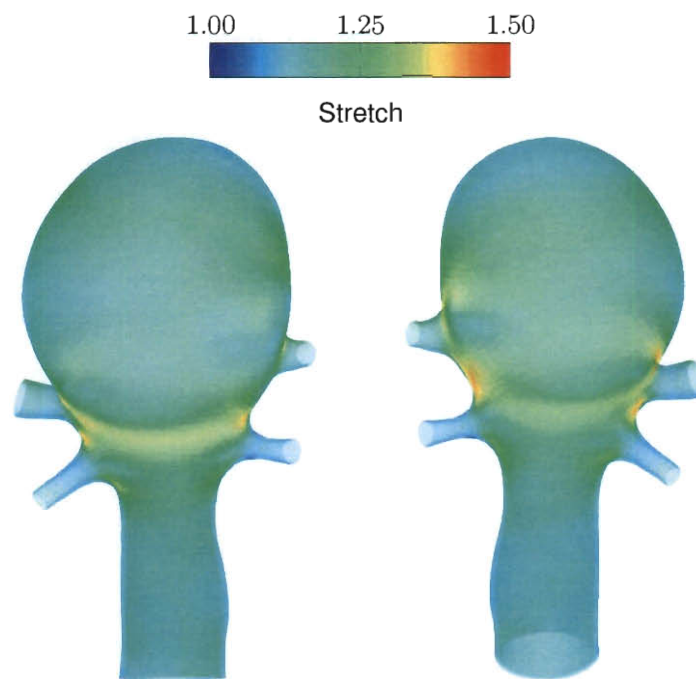


Figure 6.66: Stretch at peak pressure for M10Basilar.

### 6.3 Evaluation of Simpler Modeling Approaches

We investigate how simpler approaches to computer modeling of our ten cases compare to FSI modeling. The three simpler modeling techniques are computing the blood flow with the artery shape held fixed at the average pressure (92 mm Hg) (RA), computing the arterial wall deformation with a prescribed, time-dependent pressure (S), and computing the blood flow with the prescribed arterial shape coming from that arterial-wall computation (PS). The parameters for the simpler approaches are the same as those described in Sections 5.3–5.5 except for the two following computational parameters: number of nonlinear iterations per time step and the number of GMRES iterations per nonlinear iteration. Those values are shown in Table 6.5. For the RA and PS computations, we compare the WSS and OSI. For the Structure computations, we compare the arterial-wall stress and stretch.

Model	Nonlinear Iterations			GMRES Iterations		
	RA	PS	S	RA	PS	S
M1MCA	3	3	6	500	350	50
M2MCA	3	3	6	500	500	50
M3MCA	3	3	6	700	400	50
M4MCA	3	3	6	900	800	50
M5Acom	3	3	6	600	400	50
M6Acom	3	3	6	500	350	50
M7Acom	3	3	6	500	500	50
M8Acom	3	3	6	500	400	50
M9Basilar	3	3	6	450	450	50
M10Basilar	3	3	6	800	700	50

Table 6.5: Computational parameters for the ten arterial models. Structure scales and fluid scales are 100 and 1.0 respectively for all models.

We begin by looking at the fluid mechanics results, specifically the WSS and OSI. Figure 6.67 shows the maximum WSS for the FSI, RA, and PS techniques. We see the

maximum WSS being almost the same for the FSI and PS computations. Figure 6.68 shows the average WSS in space and time for the FSI, RA, and PS techniques. The shape for the PS comes from a structural mechanics only computation where the viscous forces from the fluid are not accounted for. This gives the PS a slightly smaller shape than the FSI shape resulting in WSS that is on average 2.5% higher than FSI. For the RA computations, we see a clear pattern of higher WSS than the FSI. The RA shape is inflated to the average pressure, which, over the interval of peak inflow flow rate, is smaller than the FSI shape over that same interval. For this reason, we see the average WSS to be 4.2% higher than FSI. Using M5Acom as a sample model, we compare the spatial distribution of the WSS and OSI obtained with the PS and RA techniques (Figures 6.69–6.72) to those obtained with the FSI computation (Figures 6.24 and 6.38). The differences between the RA and FSI computations show the need for computing with a deformable structure.

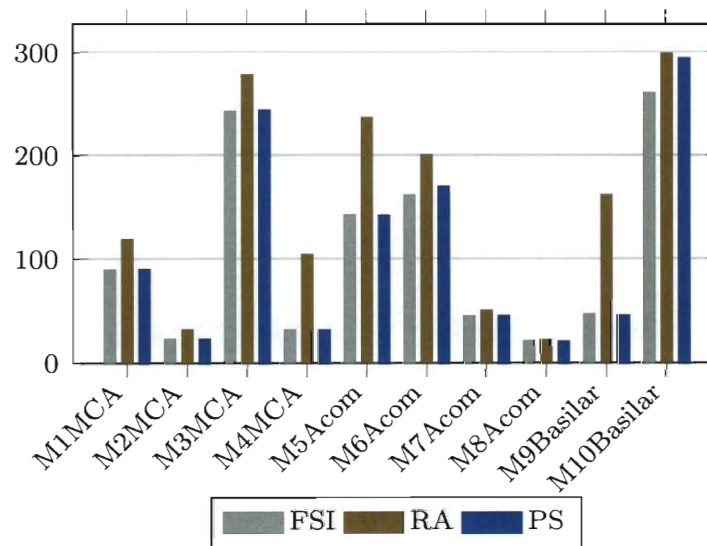


Figure 6.67: Maximum WSS ( $\text{dyn}/\text{cm}^2$ ) in space and time.



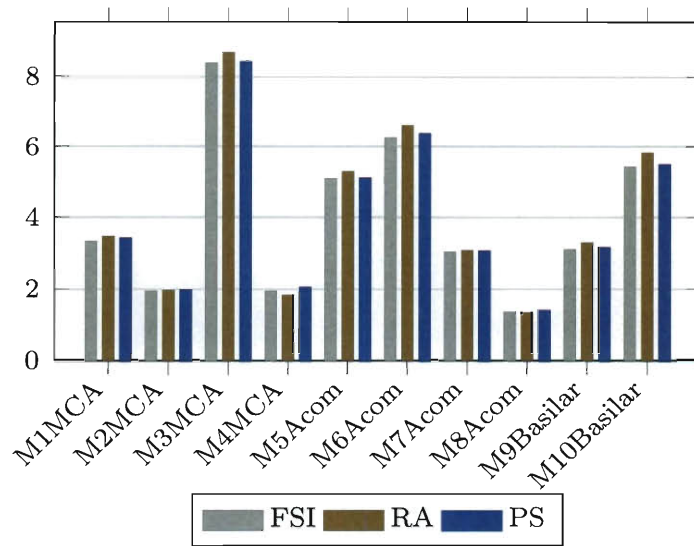


Figure 6.68: Average WSS (dyn/cm<sup>2</sup>) in space and time.

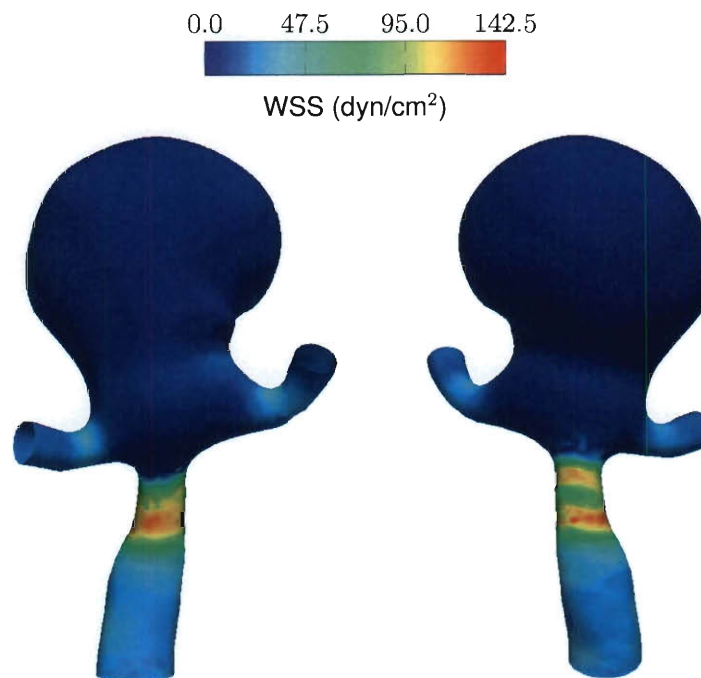


Figure 6.69: PS WSS at peak flow for M5Acom.

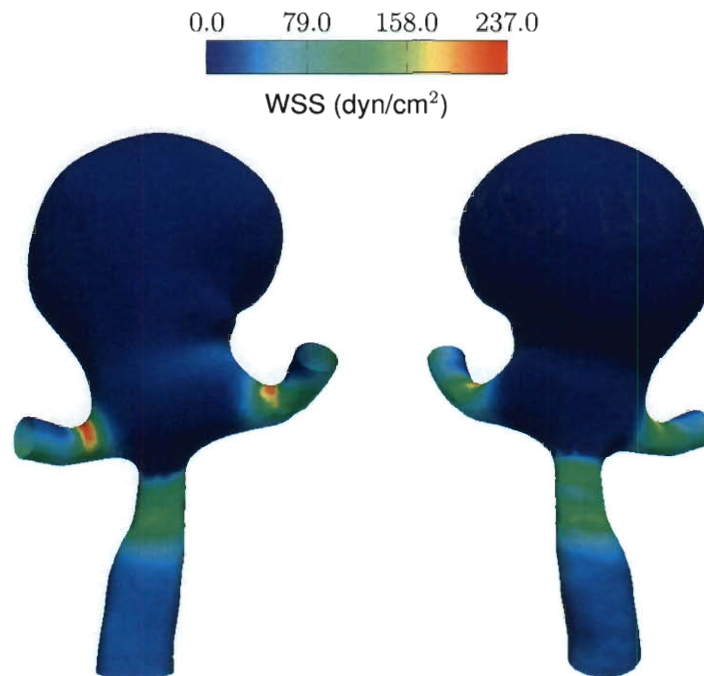


Figure 6.70: RA WSS at peak flow for M5Acom.

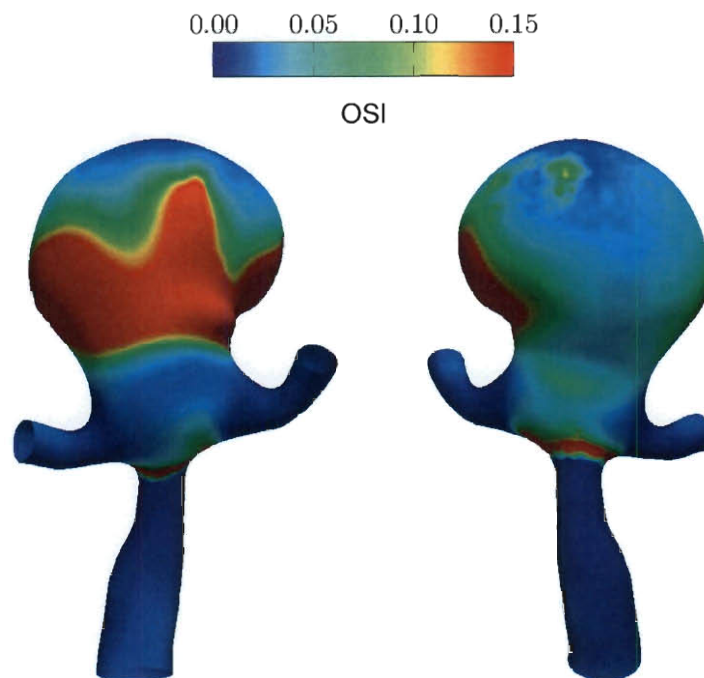


Figure 6.71: PS OSI for M5Acom.

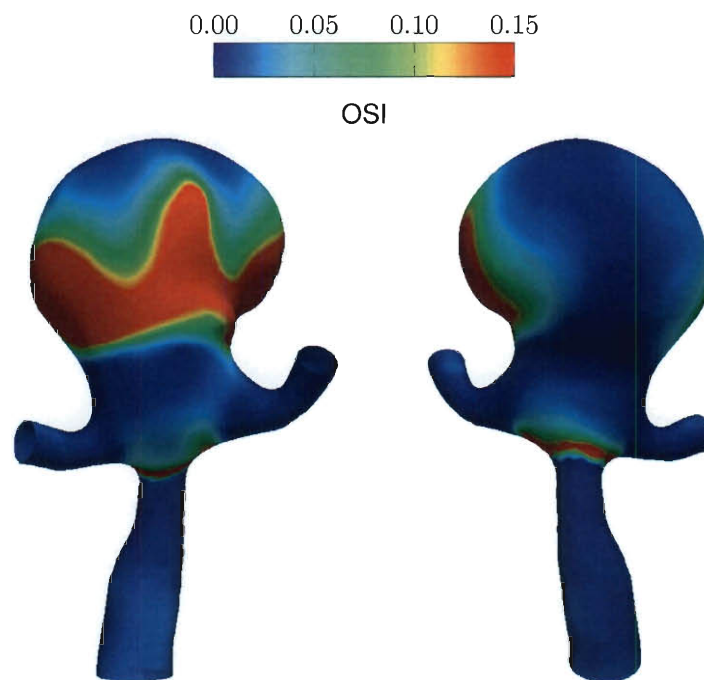


Figure 6.72: RA OSI for M5Acom.

For structural mechanics, we consider the arterial-wall stress and stretch. Figure 6.73 shows the maximum arterial-wall stress for the FSI and Structure techniques. The differences are less than 1%. By comparing, for M3MCA, the spatial stress distribution in Figure 6.74 to Figure 6.48, we see that there is very little difference between the Structure and FSI results. We also look at the average wall stretch (over space and time of the cardiac cycle) to make sure the similarity of the Structure and FSI results are not only for the maximums. Figure 6.75 shows that comparison for the ten models. Figure 6.76 shows the spatial stretch distribution which can be compared to Figure 6.59. The Structure results are slightly less than the FSI results because the Structure technique does not take into account the viscous forces from the fluid; however, as noted, these differences are small.

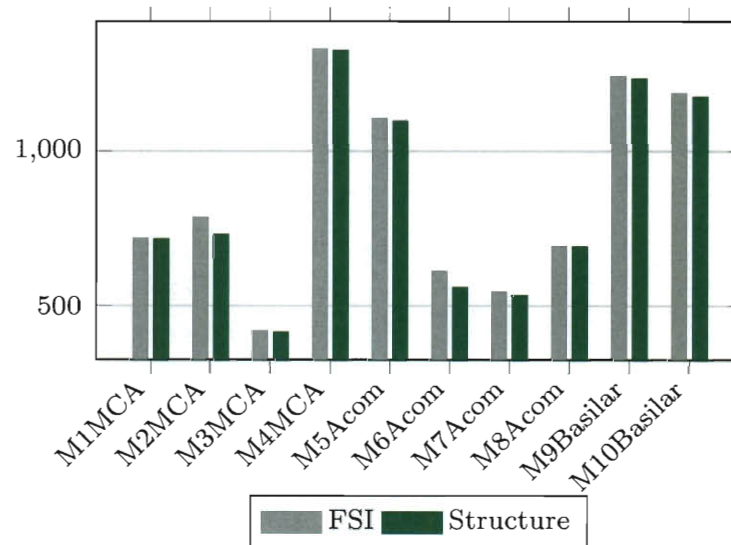


Figure 6.73: Maximum stress (kPa) in space and time.

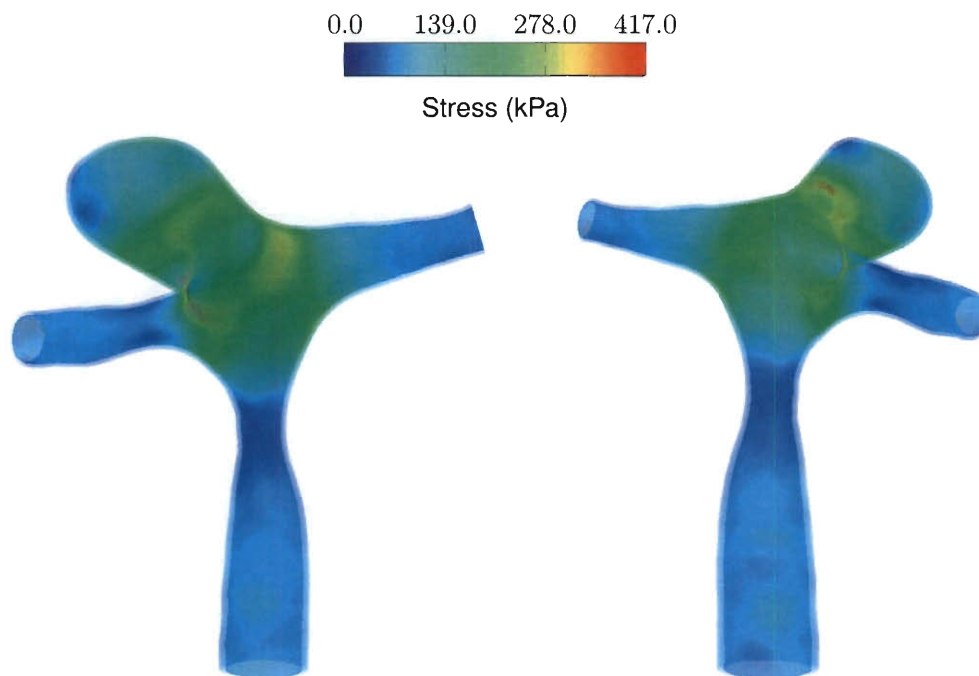


Figure 6.74: Structure only stress at peak pressure for M3MCA.

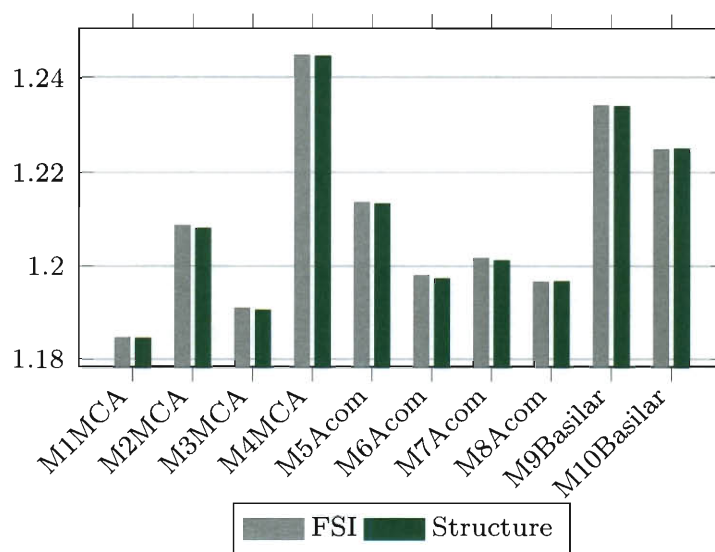


Figure 6.75: Average stretch in space and time.

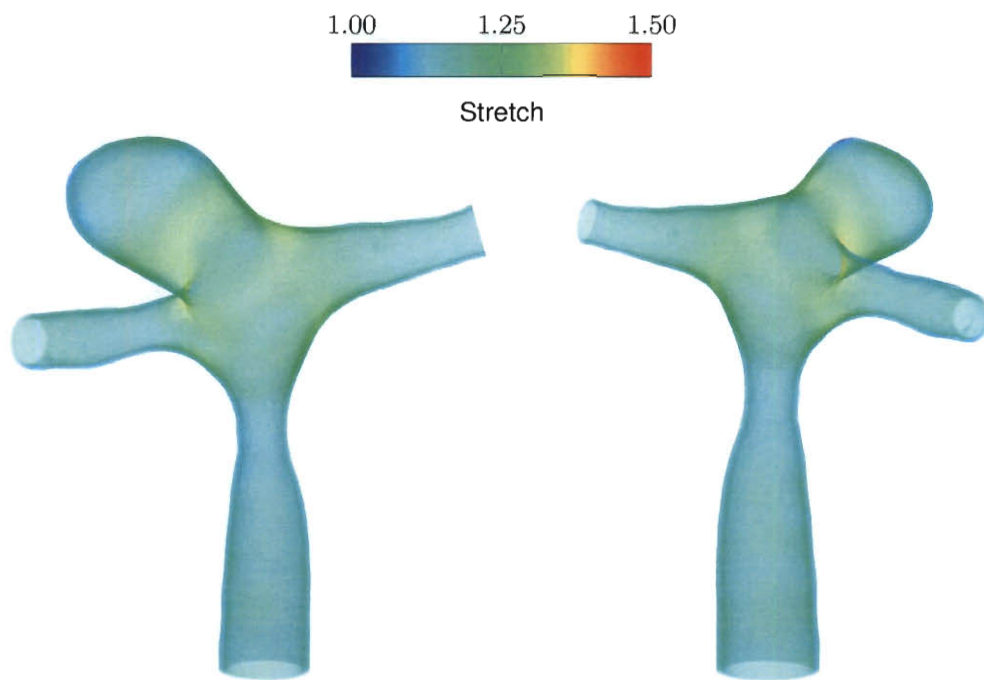


Figure 6.76: Structure only stretch at peak pressure for M3MCA.

## 6.4 Mesh Refinement

We investigate the fluid and structural mesh refinement for two models from the MCA location, one unruptured (M1MCA) and one ruptured (M3MCA). We use “-FF” and “-FS” to denote the fine fluid and structural mechanics meshes. Figure 6.77 and 6.78 show the structural mechanics meshes for M1MCA and M3MCA. Figures 6.79 and 6.80 show the fluid mechanics meshes for M1MCA and M3MCA. The node and element numbers for the structural and fluid mechanics meshes are given in Tables 6.6 and 6.7. We computed with FSI, and the three simpler approaches explained in Section 5.6.

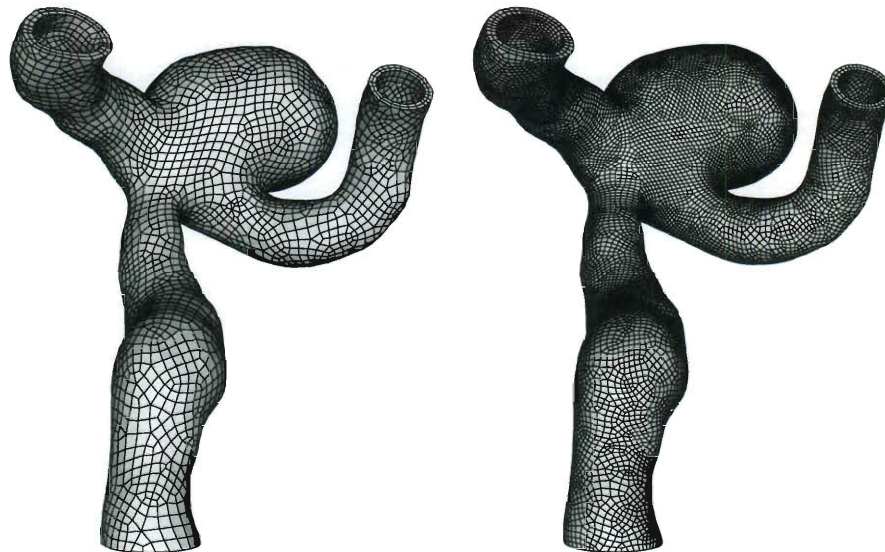


Figure 6.77: Structural mechanics meshes at zero pressure: M1MCA (left) and M1MCA-FS (right).

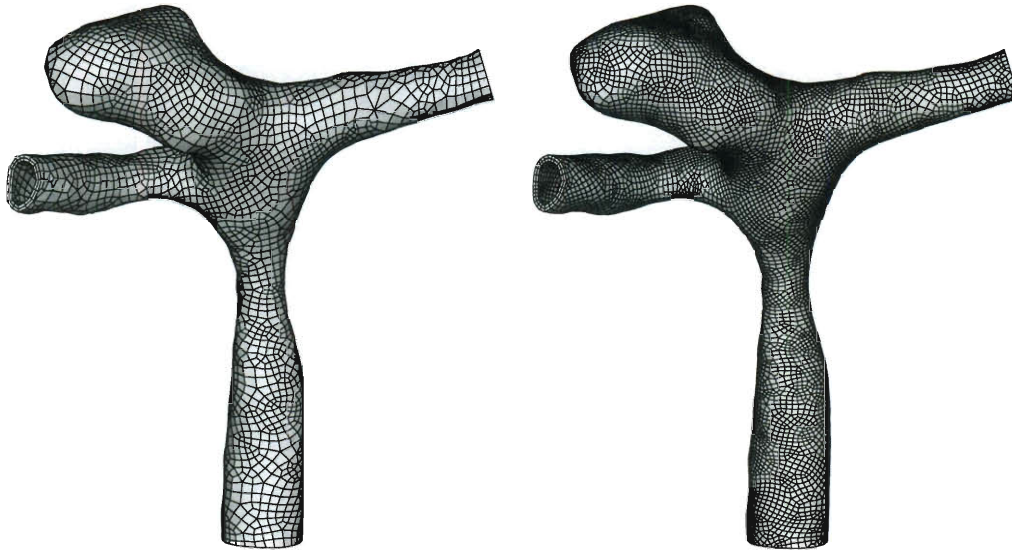


Figure 6.78: Structural mechanics meshes at zero pressure: M3MCA (left) and M3MCA-FS (right).

	Volume		Interface	
	$nn$	$ne$	$nn$	$ne$
M1MCA	14,670	9,700	4,890	4,850
M1MCA-FS	51,819	34,418	17,273	17,209
M3MCA	12,927	8,550	4,309	4,275
M3MCA-FS	34,884	23,152	11,628	11,576

Table 6.6: Number of nodes ( $nn$ ) and elements ( $ne$ ) for the standard and refined structural mechanics meshes for the two models.

	Volume		Interface	
	$nn$	$ne$	$nn$	$ne$
M1MCA	52,136	302,336	5,698	11,315
M1MCA-FF	186,753	1,111,962	15,427	30,724
M3MCA	37,610	215,844	4,485	8,898
M3MCA-FF	129,612	765,022	11,937	23,760

Table 6.7: Number of nodes ( $nn$ ) and elements ( $ne$ ) for the standard and refined fluid mechanics meshes for the two models.



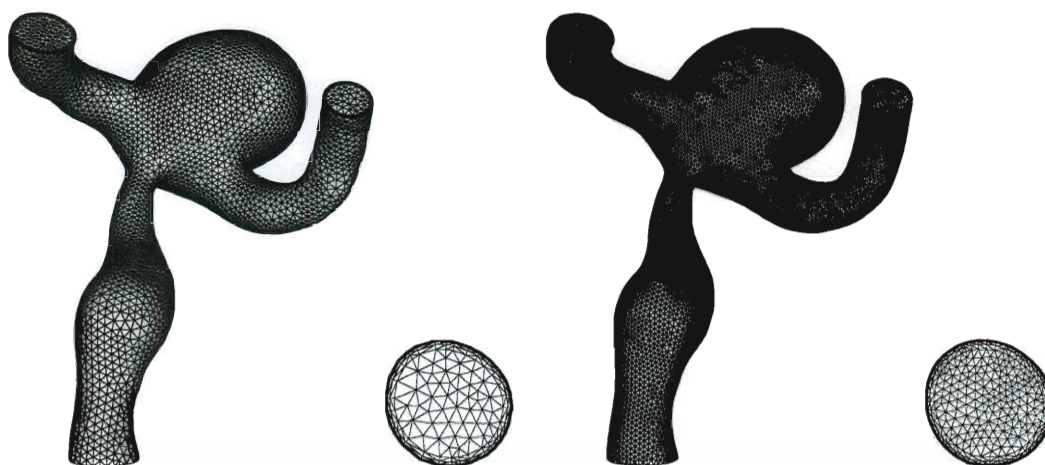


Figure 6.79: Fluid mechanics meshes at starting pressure at the fluid–structure interface and inflow plane for M1MCA (left) and M1MCA-FF (right).

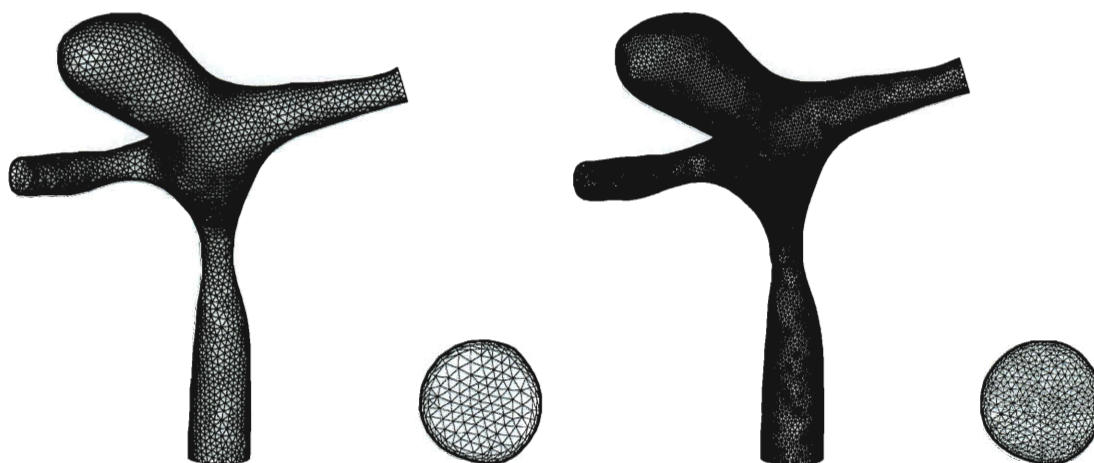


Figure 6.80: Fluid mechanics meshes at starting pressure at the fluid–structure interface and inflow plane for M3MCA (left) and M3MCA-FF (right).

We compare the fluid mechanics results by analyzing the WSS and OSI. The maximum WSS and average WSS can be seen in Table 6.8. Figure 6.81 shows the WSS at peak flow for M1MCA-FF, to be compared to Figure 6.20. Figure 6.82 shows the WSS at peak flow for M3MCA-FF, to be compared to Figure 6.22. The OSI for M1MCA-FF is shown in Figure 6.83 and can be compared to Figure 6.34. The OSI for M3MCA-FF is shown in Figure 6.84 and can be compared to Figure 6.36. Figures 6.81–6.84 are for FSI computations.

Maximum WSS			
	FSI	RA	PS
M1MCA	89.0	118.2	89.9
M1MCA-FF	96.4	126.2	96.2
M3MCA	242.2	277.7	243.5
M3MCA-FF	230.6	265.5	230.2
Average WSS			
	FSI	RA	PS
M1MCA	3.31	3.46	3.43
M1MCA-FF	3.41	3.57	3.42
M3MCA	8.37	8.67	8.42
M3MCA-FF	8.44	8.77	8.46

Table 6.8: Maximum and average WSS (dyn/cm<sup>2</sup>) in space and time.

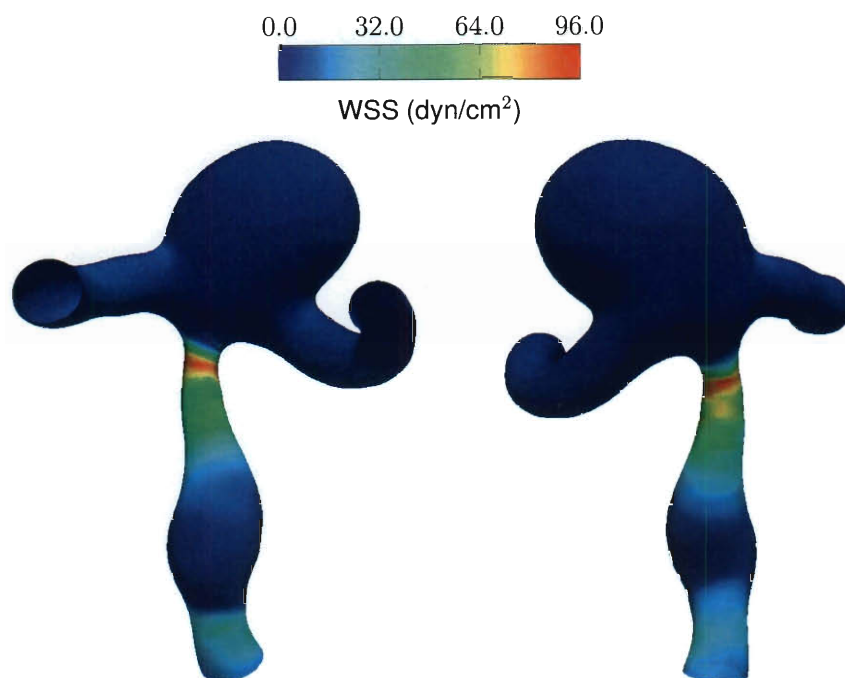


Figure 6.81: WSS at peak flow for M1MCA-FF.

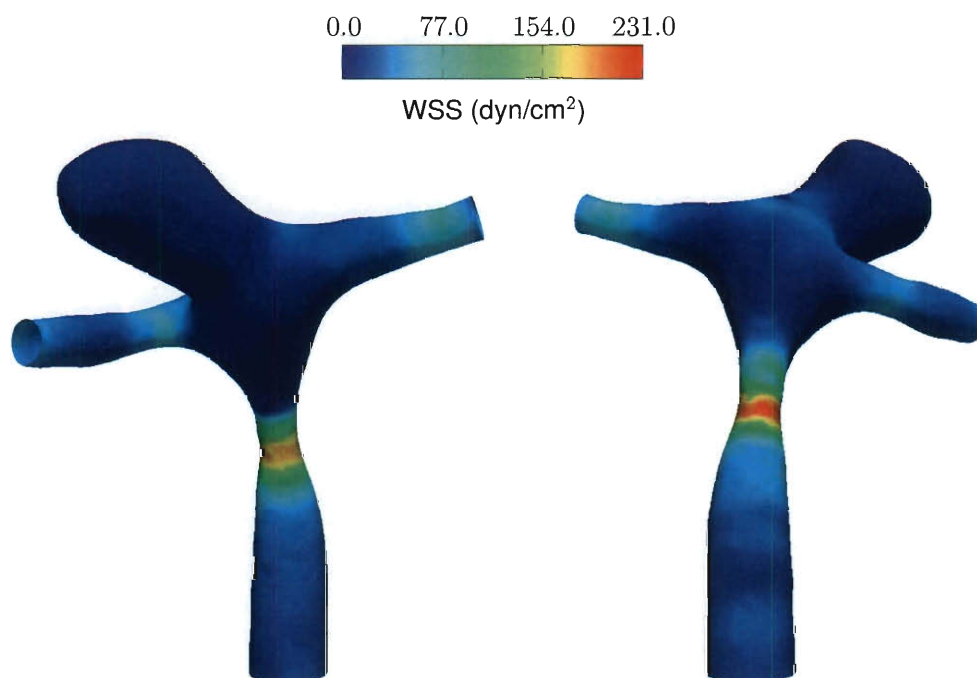


Figure 6.82: WSS at peak flow for M3MCA-FF.

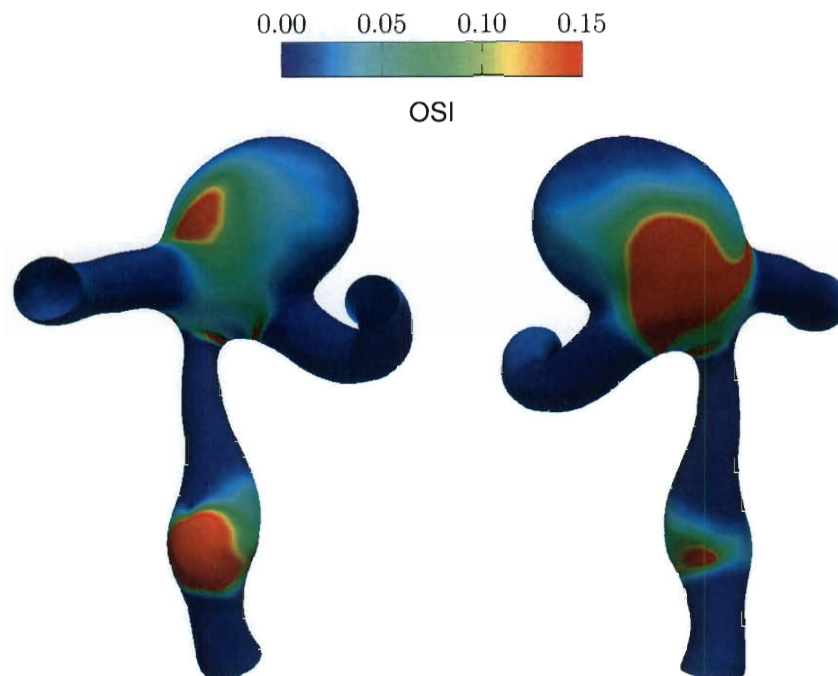


Figure 6.83: OSI for M1MCA-FF.

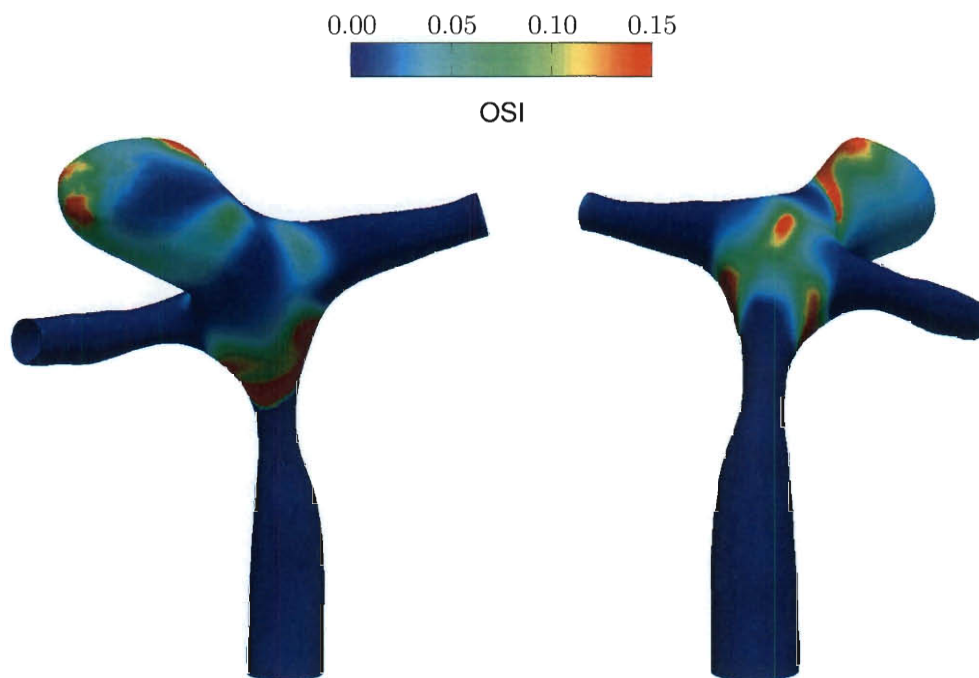


Figure 6.84: OSI for M3MCA-FF.

We compare the structural mechanics results by comparing the arterial-wall stress and stretch. The maximum stress and average stretch of the arterial-wall can be seen in Table 6.9. Figure 6.85 shows the arterial-wall stress at peak pressure for M1MCA-FS, which can be compared to Figure 6.46. Figure 6.86 shows the arterial-wall stress at peak pressure for M3MCA-FS, which can be compared to Figure 6.48. The stretch of the arterial-wall for M1MCA-FS is shown in Figure 6.87, which can be compared to Figure 6.57. The stretch of the arterial-wall for M3MCA-FS is shown in Figure 6.88, which can be compared to Figure 6.59. Figures 6.85–6.88 are for FSI computations.

Maximum Stress		
	FSI	S
M1MCA	717.8	716.9
M1MCA-FS	705.9	704.7
M3MCA	416.6	413.9
M3MCA-FS	449.1	446.2
Average Stretch		
	FSI	S
M1MCA	1.18	1.18
M1MCA-FS	1.18	1.18
M3MCA	1.19	1.19
M3MCA-FS	1.19	1.19

Table 6.9: Maximum stress (kPa) at peak pressure and average stretch in space and time.

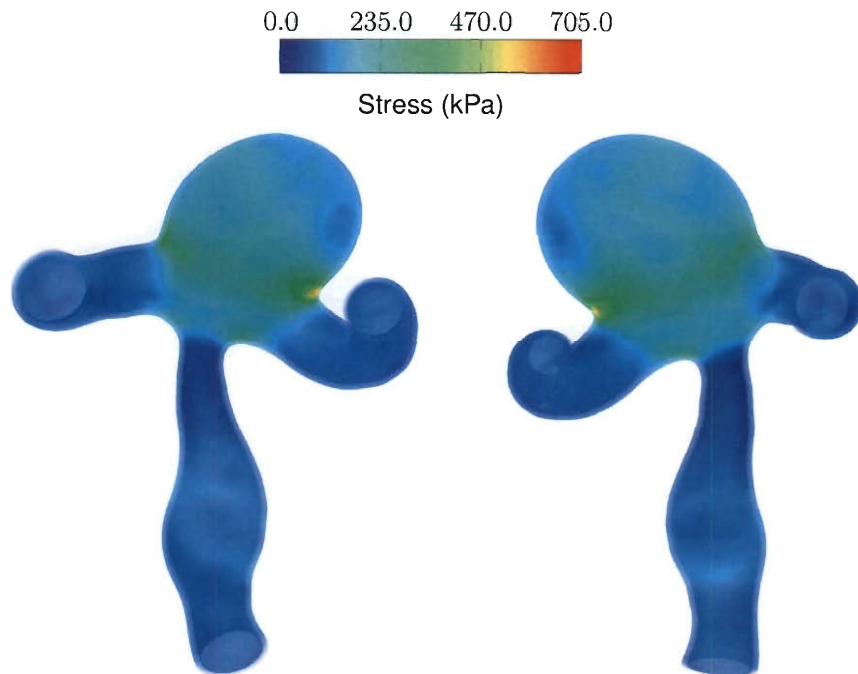


Figure 6.85: Stress at peak pressure for M1MCA-FS.

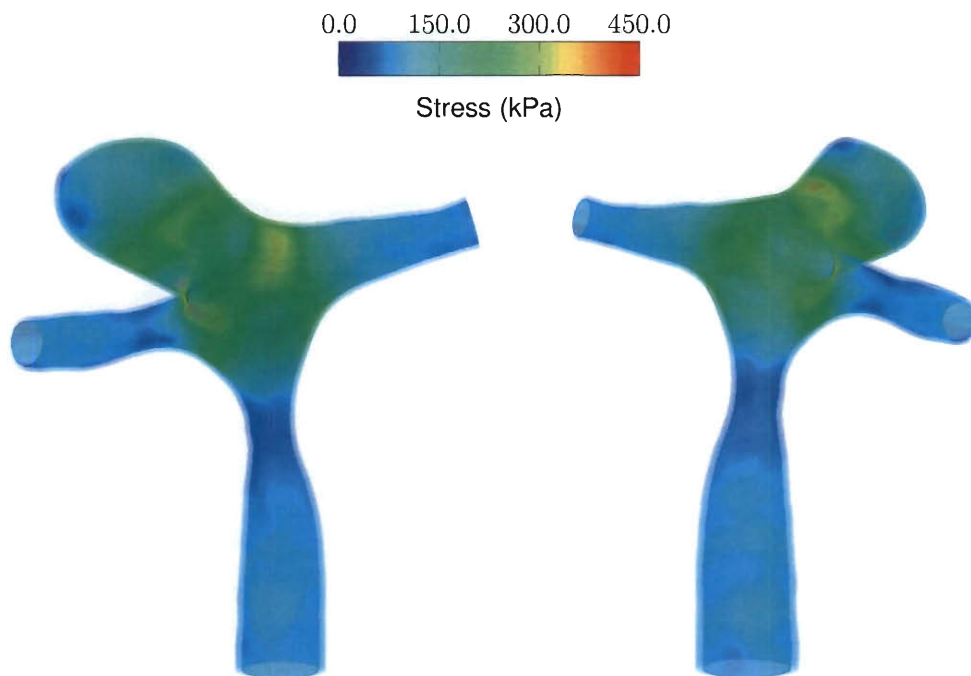


Figure 6.86: Stress at peak pressure for M3MCA-FS.

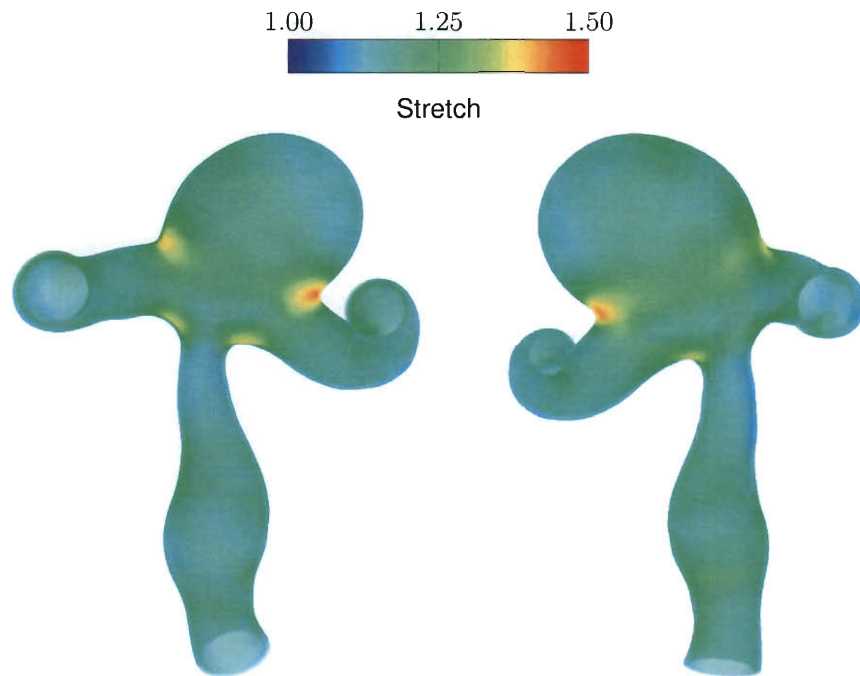


Figure 6.87: Stretch at peak pressure for M1MCA-FS.

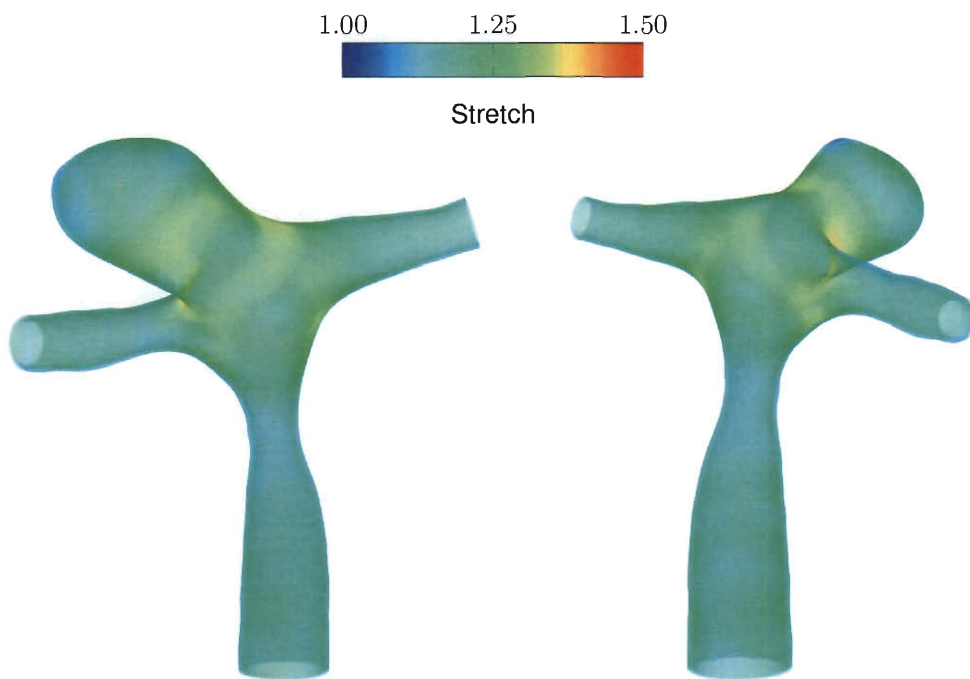


Figure 6.88: Stretch at peak pressure for M3MCA-FS.

# Chapter 7

## Findings and Conclusions

We summarize the findings of this thesis in Section 7.1 and offer conclusions in Section 7.2.

### 7.1 Findings

The original motivation of the comparative study was to find significant differences between ruptured and unruptured aneurysms. However, from what we observe in blood flow and structural mechanics characteristics, we do not find conclusive evidence for a categorical difference between ruptured and unruptured aneurysms. There are many factors that cause an aneurysm to rupture, many of which are unknown (at least to us as engineers at this stage of our research on this subject) and might be unpredictable. Our models do not account for such factors and are computed under standard conditions. In an attempt to account for conditions different than standard, we have also computed models with high blood pressure and with thinner aneurysm walls (not reported in this thesis), but these do not offer further insights and still do not account for the biological conditions that can randomly change in a patient. Although the comparative studies did not generate results helping us understand why some aneurysms rupture and some do not, we generated a comprehensive set of data



that we hope would serve as a reference for researchers modeling aneurysms.

Our work also motivated simpler approaches to modeling and mesh refinement studies that offer insights into possible future computations. As Section 6.3 has shown, when concerned only with the arterial-wall results of the computation, the Structure method can produce results with minimal error. However, when desiring accurate blood flow characteristics of a model, at least a deformable structure is required. The results of Section 6.4 lead us to think that a structural and fluid mechanics mesh more refined than those used in the comparative study might be desirable.

## 7.2 Conclusions

We have described many of the techniques developed by the T★AFSM for FSI modeling and their application to patient-specific FSI modeling of cerebral aneurysms. The SSTFSI technique, together with a number of special techniques targeting arterial FSI modeling were used. An extensive comparative study was performed on a total of ten artery models, coming from three different locations, half of which were ruptured. The physical characteristics of WSS, OSI, and arterial-wall stress and stretch were compared in an effort that was originally motivated by looking for significant differences between ruptured and unruptured aneurysms. We also showed how simpler approaches perform compared to FSI modeling. The simpler approaches were computing the blood flow with the artery shape held fixed, computing the arterial wall deformation with a prescribed, time-dependent pressure, and computing the blood flow with the prescribed arterial shape coming from that arterial wall computation. In addition, we provided some mesh refinement results.

# Bibliography

- [1] J. E. Akin, T. Tezduyar, M. Ungor, and S. Mittal. Stabilization parameters and Smagorinsky turbulence model. *Journal of Applied Mechanics*, 70:2–9, 2003.
- [2] J. E. Akin and T. E. Tezduyar. Calculation of the advective limit of the SUPG stabilization parameter for linear and higher-order elements. *Computer Methods in Applied Mechanics and Engineering*, 193:1909–1922, 2004.
- [3] S. K. Aliabadi and T. E. Tezduyar. Parallel fluid dynamics computations in aerospace applications. *International Journal for Numerical Methods in Fluids*, 21:783–805, 1995.
- [4] Y. Bazilevs, V. M. Calo, T. J. R. Hughes, and Y. Zhang. Isogeometric fluid–structure interaction: theory, algorithms, and computations. *Computational Mechanics*, 43:3–37, 2008.
- [5] Y. Bazilevs, V. M. Calo, Y. Zhang, and T. J. R. Hughes. Isogeometric fluid–structure interaction analysis with applications to arterial blood flow. *Computational Mechanics*, 38:310–322, 2006.
- [6] Y. Bazilevs, J. R. Gohean, T. J. R. Hughes, R. D. Moser, and Y. Zhang. Patient-specific isogeometric fluid–structure interaction analysis of thoracic aortic blood flow due to implantation of the Jarvik 2000 left ventricular assist device. *Computer Methods in Applied Mechanics and Engineering*, 198:3534–3550, 2009.

- [7] Y. Bazilevs, M.-C. Hsu, D. Benson, S. Sankaran, and A. Marsden. Computational fluid–structure interaction: Methods and application to a total cavopulmonary connection. *Computational Mechanics*, 45:77–89, 2009.
- [8] Y. Bazilevs, M.-C. Hsu, Y. Zhang, W. Wang, T. Kvamsdal, S. Hentschel, and J. Isaksen. Computational fluid–structure interaction: Methods and application to cerebral aneurysms. *Biomechanics and Modeling in Mechanobiology*, 9:481–498, 2010.
- [9] Y. Bazilevs, M.-C. Hsu, Y. Zhang, W. Wang, X. Liang, T. Kvamsdal, R. Brekken, and J. Isaksen. A fully-coupled fluid–structure interaction simulation of cerebral aneurysms. *Computational Mechanics*, 46:3–16, 2010.
- [10] M. Behr, A. Johnson, J. Kennedy, S. Mittal, and T. Tezduyar. Computation of incompressible flows with implicit finite element implementations on the Connection Machine. *Computer Methods in Applied Mechanics and Engineering*, 108:99–118, 1993.
- [11] M. Behr and T. Tezduyar. The Shear-Slip Mesh Update Method. *Computer Methods in Applied Mechanics and Engineering*, 174:261–274, 1999.
- [12] R. J. Benney, K. R. Stein, J. W. Leonard, and M. L. Accorsi. Current 3-D structural dynamic finite element modeling capabilities. In *Proceedings of AIAA 14th Aerodynamic Decelerator Systems Technology Conference*, AIAA Paper 97-1506, San Francisco, California, 1997.
- [13] L. Catabriga, A. L. G. A. Coutinho, and T. E. Tezduyar. Compressible flow SUPG parameters computed from element matrices. *Communications in Numerical Methods in Engineering*, 21:465–476, 2005.

- [14] L. Catabriga, A. L. G. A. Coutinho, and T. E. Tezduyar. Compressible flow SUPG parameters computed from degree-of-freedom submatrices. *Computational Mechanics*, 38:334–343, 2006.
- [15] A. Corsini, F. Rispoli, and T. E. Tezduyar. Stabilized finite element computation of NOx emission in aero-engine combustors. *International Journal for Numerical Methods in Fluids*, 65:254–270, 2011.
- [16] W. G. Dettmer and D. Peric. On the coupling between fluid flow and mesh motion in the modelling of fluid–structure interaction. *Computational Mechanics*, 43:81–90, 2008.
- [17] O. Frank. Die grundform des arteriellen pulses. *Zeitung fur Biologie*, 37:483–586, 1899.
- [18] R. Higashida. What you should know about cerebral aneurysms, 2003. [http://avm.ucsf.edu/patient\\_info/WhatYouShouldKnow/WhatYouShouldKnow.pdf](http://avm.ucsf.edu/patient_info/WhatYouShouldKnow/WhatYouShouldKnow.pdf).
- [19] H. M. Hilber, T. J. R. Hughes, and R. L. Taylor. Improved numerical dissipation for time integration algorithms in structural dynamics. *Earthquake Engineering and Structural Dynamics*, 5:283–292, 1977.
- [20] M.-C. Hsu, Y. Bazilevs, V. M. Calo, T. E. Tezduyar, and T. J. R. Hughes. Improving stability of stabilized and multiscale formulations in flow simulations at small time steps. *Computer Methods in Applied Mechanics and Engineering*, 199:828–840, 2010.
- [21] H. Huang, R. Virmani, H. Younis, A. P. Burke, R. D. Kamm, and R. T. Lee. The impact of calcification on the biomechanical stability of atherosclerotic plaques. *Circulation*, 103:1051–1056, 2001.

- [22] J. G. Isaksen, Y. Bazilevs, T. Kvamsdal, Y. Zhang, J. H. Kaspersen, K. Waterloo, B. Romner, and T. Ingebrigtsen. Determination of wall tension in cerebral artery aneurysms by numerical simulation. *Stroke*, 39:3172–3178, 2008.
- [23] A. A. Johnson and T. E. Tezduyar. Advanced mesh generation and update methods for 3D flow simulations. *Computational Mechanics*, 23:130–143, 1999.
- [24] V. Kalro and T. E. Tezduyar. A parallel 3D computational method for fluid–structure interactions in parachute systems. *Computer Methods in Applied Mechanics and Engineering*, 190:321–332, 2000.
- [25] R. A. Khurram and A. Masud. A multiscale/stabilized formulation of the incompressible Navier–Stokes equations for moving boundary flows and fluid–structure interaction. *Computational Mechanics*, 38:403–416, 2006.
- [26] A. Lo. *Nonlinear Dynamic Analysis of Cable and Membrane Structure*. PhD thesis, Department of Civil Engineering, Oregon State University, 1982.
- [27] D. J. Macdonald, H. M. Finlay, and P. B. Canham. Directional wall strength in saccular brain aneurysms from polarized light microscopy. *Annals of Biomedical Engineering*, 28:533–542, 2000.
- [28] M. Manguoglu, A. H. Sameh, T. E. Tezduyar, and S. Sathe. A nested iterative scheme for computation of incompressible flows in long domains. *Computational Mechanics*, 43:73–80, 2008.
- [29] M. Manguoglu, K. Takizawa, A. H. Sameh, and T. E. Tezduyar. Solution of linear systems in arterial fluid mechanics computations with boundary layer mesh refinement. *Computational Mechanics*, 46:83–89, 2010.
- [30] M. Manguoglu, K. Takizawa, A. H. Sameh, and T. E. Tezduyar. Nested and parallel sparse algorithms for arterial fluid mechanics computations with boundary

- layer mesh refinement. *International Journal for Numerical Methods in Fluids*, 65:135–149, 2011.
- [31] T. McPhail and J. Warren. An interactive editor for deforming volumetric data. In *International Conference on Biomedical Engineering 2008*, pages 137–144, Singapore, 2008.
- [32] R. Ohayon. Reduced symmetric models for modal analysis of internal structural-acoustic and hydroelastic-sloshing systems. *Computer Methods in Applied Mechanics and Engineering*, 190:3009–3019, 2001.
- [33] F. Rispoli, A. Corsini, and T. E. Tezduyar. Finite element computation of turbulent flows with the discontinuity-capturing directional dissipation (DCDD). *Computers & Fluids*, 36:121–126, 2007.
- [34] C. Roy. The elastic properties of the arterial wall. *J. Physiol*, 3(2):125–159, 1881.
- [35] S. Sathe and T. E. Tezduyar. Modeling of fluid–structure interactions with the space–time finite elements: Contact problems. *Computational Mechanics*, 43:51–60, 2008.
- [36] T. Sawada and T. Hisada. Fluid–structure interaction analysis of the two dimensional flag-in-wind problem by an interface tracking ALE finite element method. *Computers & Fluids*, 36:136–146, 2007.
- [37] K. Stein, R. Benney, V. Kalro, T. E. Tezduyar, J. Leonard, and M. Accorsi. Parachute fluid–structure interactions: 3-D Computation. *Computer Methods in Applied Mechanics and Engineering*, 190:373–386, 2000.
- [38] K. Stein, R. Benney, T. Tezduyar, and J. Potvin. Fluid–structure interactions of a cross parachute: Numerical simulation. *Computer Methods in Applied Mechanics and Engineering*, 191:673–687, 2001.

- [39] K. Takizawa, J. Christopher, T. E. Tezduyar, and S. Sathe. Space–time finite element computation of arterial fluid–structure interactions with patient-specific data. *International Journal for Numerical Methods in Biomedical Engineering*, 26:101–116, 2010.
- [40] K. Takizawa, C. Moorman, S. Wright, J. Christopher, and T. E. Tezduyar. Wall shear stress calculations in space–time finite element computation of arterial fluid–structure interactions. *Computational Mechanics*, 46:31–41, 2010.
- [41] K. Takizawa, C. Moorman, S. Wright, J. Purdue, T. McPhail, P. R. Chen, J. Warren, and T. E. Tezduyar. Patient-specific arterial fluid–structure interaction modeling of cerebral aneurysms. *International Journal for Numerical Methods in Fluids*, 65:308–323, 2011.
- [42] K. Takizawa, C. Moorman, S. Wright, T. Spielman, and T. E. Tezduyar. Fluid–structure interaction modeling and performance analysis of the Orion spacecraft parachutes. *International Journal for Numerical Methods in Fluids*, 65:271–285, 2011.
- [43] K. Takizawa, T. Spielman, and T. E. Tezduyar. Space–time FSI modeling and dynamical analysis of spacecraft parachutes and parachute clusters. *Computational Mechanics*, to appear, 2011.
- [44] K. Takizawa, K. Tanizawa, T. Yabe, and T. E. Tezduyar. Ship hydrodynamics computations with the CIP method based on adaptive Soroban grids. *International Journal for Numerical Methods in Fluids*, 54:1011–1019, 2007.
- [45] K. Takizawa and T. E. Tezduyar. Multiscale space–time fluid–structure interaction techniques. *Computational Mechanics*, published online, DOI: 10.1007/s00466-011-0571-z, February 2011.

- [46] K. Takizawa, S. Wright, C. Moorman, and T. E. Tezduyar. Fluid–structure interaction modeling of parachute clusters. *International Journal for Numerical Methods in Fluids*, 65:286–307, 2011.
- [47] K. Takizawa, T. Yabe, Y. Tsugawa, T. E. Tezduyar, and H. Mizoe. Computation of free–surface flows and fluid–object interactions with the CIP method based on adaptive meshless Soroban grids. *Computational Mechanics*, 40:167–183, 2007.
- [48] C. Taylor and J. Humphrey. Open problems in computational vascular biomechanics: Hemodynamics and arterial wall mechanics. *Computer Methods in Applied Mechanics and Engineering*, 198(45-46):3514 – 3523, 2009.
- [49] C. A. Taylor, T. J. R. Hughes, and C. K. Zarins. Finite element modeling of three-dimensional pulsatile flow in the abdominal aorta: relevance to atherosclerosis. *Ann. Biomed. Engrg.*, 158:975–987, 1998.
- [50] T. Tezduyar, S. Aliabadi, M. Behr, A. Johnson, and S. Mittal. Parallel finite-element computation of 3D flows. *Computer*, 26(10):27–36, 1993.
- [51] T. Tezduyar and Y. Osawa. Fluid–structure interactions of a parachute crossing the far wake of an aircraft. *Computer Methods in Applied Mechanics and Engineering*, 191:717–726, 2001.
- [52] T. E. Tezduyar. Stabilized finite element formulations for incompressible flow computations. *Advances in Applied Mechanics*, 28:1–44, 1992.
- [53] T. E. Tezduyar. Computation of moving boundaries and interfaces and stabilization parameters. *International Journal for Numerical Methods in Fluids*, 43:555–575, 2003.
- [54] T. E. Tezduyar. Finite element methods for fluid dynamics with moving boundaries and interfaces. In E. Stein, R. D. Borst, and T. J. R. Hughes, editors,



- Encyclopedia of Computational Mechanics*, Volume 3: Fluids, chapter 17. John Wiley & Sons, 2004.
- [55] T. E. Tezduyar. Finite elements in fluids: Stabilized formulations and moving boundaries and interfaces. *Computers & Fluids*, 36:191–206, 2007.
- [56] T. E. Tezduyar, M. Behr, and J. Liou. A new strategy for finite element computations involving moving boundaries and interfaces – the deforming-spatial-domain/space–time procedure: I. The concept and the preliminary numerical tests. *Computer Methods in Applied Mechanics and Engineering*, 94(3):339–351, 1992.
- [57] T. E. Tezduyar, M. Behr, S. Mittal, and J. Liou. A new strategy for finite element computations involving moving boundaries and interfaces – the deforming-spatial-domain/space–time procedure: II. Computation of free-surface flows, two-liquid flows, and flows with drifting cylinders. *Computer Methods in Applied Mechanics and Engineering*, 94(3):353–371, 1992.
- [58] T. E. Tezduyar and Y. Osawa. Finite element stabilization parameters computed from element matrices and vectors. *Computer Methods in Applied Mechanics and Engineering*, 190:411–430, 2000.
- [59] T. E. Tezduyar and S. Sathe. Modeling of fluid–structure interactions with the space–time finite elements: Solution techniques. *International Journal for Numerical Methods in Fluids*, 54:855–900, 2007.
- [60] T. E. Tezduyar, S. Sathe, T. Cragin, B. Nanna, B. S. Conklin, J. Pausewang, and M. Schwaab. Modeling of fluid–structure interactions with the space–time finite elements: Arterial fluid mechanics. *International Journal for Numerical Methods in Fluids*, 54:901–922, 2007.

- [61] T. E. Tezduyar, S. Sathe, R. Keedy, and K. Stein. Space–time finite element techniques for computation of fluid–structure interactions. *Computer Methods in Applied Mechanics and Engineering*, 195:2002–2027, 2006.
- [62] T. E. Tezduyar, S. Sathe, J. Pausewang, M. Schwaab, J. Christopher, and J. Crabtree. Fluid–structure interaction modeling of ringsail parachutes. *Computational Mechanics*, 43:133–142, 2008.
- [63] T. E. Tezduyar, S. Sathe, J. Pausewang, M. Schwaab, J. Christopher, and J. Crabtree. Interface projection techniques for fluid–structure interaction modeling with moving-mesh methods. *Computational Mechanics*, 43:39–49, 2008.
- [64] T. E. Tezduyar, S. Sathe, M. Schwaab, and B. S. Conklin. Arterial fluid mechanics modeling with the stabilized space–time fluid–structure interaction technique. *International Journal for Numerical Methods in Fluids*, 57:601–629, 2008.
- [65] T. E. Tezduyar, S. Sathe, and K. Stein. Solution techniques for the fully-discretized equations in computation of fluid–structure interactions with the space–time formulations. *Computer Methods in Applied Mechanics and Engineering*, 195:5743–5753, 2006.
- [66] T. E. Tezduyar, M. Schwaab, and S. Sathe. Sequentially-Coupled Arterial Fluid–Structure Interaction (SCAFSI) technique. *Computer Methods in Applied Mechanics and Engineering*, 198:3524–3533, 2009.
- [67] T. E. Tezduyar, K. Takizawa, T. Brummer, and P. R. Chen. Space–time fluid–structure interaction modeling of patient-specific cerebral aneurysms. *International Journal for Numerical Methods in Biomedical Engineering*, published online, DOI: 10.1002/cnm.1433, February 2011.
- [68] T. E. Tezduyar, K. Takizawa, and J. Christopher. Multiscale Sequentially-Coupled Arterial Fluid–Structure Interaction (SCAFSI) technique. In S. Hart-

- mann, A. Meister, M. Schaefer, and S. Turek, editors, *International Workshop on Fluid–Structure Interaction — Theory, Numerics and Applications*, pages 231–252. Kassel University Press, 2009.
- [69] T. E. Tezduyar, K. Takizawa, C. Moorman, S. Wright, and J. Christopher. Multiscale sequentially-coupled arterial FSI technique. *Computational Mechanics*, 46:17–29, 2010.
- [70] T. E. Tezduyar, K. Takizawa, C. Moorman, S. Wright, and J. Christopher. Space–time finite element computation of complex fluid–structure interactions. *International Journal for Numerical Methods in Fluids*, 64:1201–1218, 2010.
- [71] R. Torii, M. Oshima, T. Kobayashi, K. Takagi, and T. E. Tezduyar. Influence of wall elasticity on image-based blood flow simulation. *Japan Society of Mechanical Engineers Journal Series A*, 70:1224–1231, 2004. in Japanese.
- [72] R. Torii, M. Oshima, T. Kobayashi, K. Takagi, and T. E. Tezduyar. Computer modeling of cardiovascular fluid–structure interactions with the Deforming-Spatial-Domain/Stabilized Space–Time formulation. *Computer Methods in Applied Mechanics and Engineering*, 195:1885–1895, 2006.
- [73] R. Torii, M. Oshima, T. Kobayashi, K. Takagi, and T. E. Tezduyar. Fluid–structure interaction modeling of aneurysmal conditions with high and normal blood pressures. *Computational Mechanics*, 38:482–490, 2006.
- [74] R. Torii, M. Oshima, T. Kobayashi, K. Takagi, and T. E. Tezduyar. Influence of wall elasticity in patient-specific hemodynamic simulations. *Computers & Fluids*, 36:160–168, 2007.
- [75] R. Torii, M. Oshima, T. Kobayashi, K. Takagi, and T. E. Tezduyar. Numerical investigation of the effect of hypertensive blood pressure on cerebral aneurysm

- Dependence of the effect on the aneurysm shape. *International Journal for Numerical Methods in Fluids*, 54:995–1009, 2007.
- [76] R. Torii, M. Oshima, T. Kobayashi, K. Takagi, and T. E. Tezduyar. Fluid–structure interaction modeling of a patient-specific cerebral aneurysm: Influence of structural modeling. *Computational Mechanics*, 43:151–159, 2008.
- [77] R. Torii, M. Oshima, T. Kobayashi, K. Takagi, and T. E. Tezduyar. Fluid–structure interaction modeling of blood flow and cerebral aneurysm: Significance of artery and aneurysm shapes. *Computer Methods in Applied Mechanics and Engineering*, 198:3613–3621, 2009.
- [78] R. Torii, M. Oshima, T. Kobayashi, K. Takagi, and T. E. Tezduyar. Influence of wall thickness on fluid–structure interaction computations of cerebral aneurysms. *International Journal for Numerical Methods in Biomedical Engineering*, 26:336–347, 2010.
- [79] R. Torii, M. Oshima, T. Kobayashi, K. Takagi, and T. E. Tezduyar. Role of 0D peripheral vasculature model in fluid–structure interaction modeling of aneurysms. *Computational Mechanics*, 46:43–52, 2010.
- [80] E. H. van Brummelen and R. de Borst. On the nonnormality of subiteration for a fluid-structure interaction problem. *SIAM Journal on Scientific Computing*, 27:599–621, 2005.
- [81] C. Vega, K. Kwon, and S. Lavine. Intracranial aneurysms: Current evidence and clinical practice. *American Family Physician*, 66(4):601–608, 2002.
- [82] R. E. Wells Jr. and E. W. Merrill. Shear rate dependence of the viscosity of whole blood and plasma. *Science*, 133(3455):763–764, 1961.

- [83] J. R. Womersley. Method for the calculation of velocity, rate of flow and viscous drag in arteries when the pressure gradient is known. *Journal of Physiology*, 127:553–563, 1955.
- [84] T. Yabe, K. Takizawa, T. E. Tezduyar, and H.-N. Im. Computation of fluid–solid and fluid–fluid interfaces with the CIP method based on adaptive Soroban grids — An overview. *International Journal for Numerical Methods in Fluids*, 54:841–853, 2007.
- [85] T. Young. Hydraulic investigations, subservient to an intended croonian lecture on the motion of the blood. *Philosophical Transactions of the Royal Society of London*, 98:pp. 164–186, 1808.